Thermal Stability of Nb_3Sn Rutherford Cables for Accelerator Magnets

W.M. de Rapper

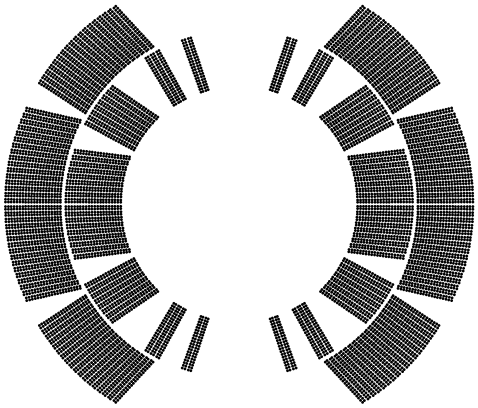

Graduation Committee:

Chairman and secretary

prof. dr. ir. J.W.M. Hilgenkamp	University of Twente

Supervisor

prof. dr. ir. H.H.J. ten Kate	University of Twente

Assistant supervisor

dr. M. Dhallé	University of Twente

Members

dr. A. Ballarino	CERN
prof. dr. ir. A.H. van den Boogaard	University of Twente
prof. dr. ir. J.A.M. Dam	Eindhoven University of Technology
prof. dr. ing. B. van Eijk	NIKHEF
prof. dr. ing. A.J.H.M. Rijnders	University of Twente

Thermal Stability of Nb_3Sn Rutherford Cables for Accelerator Magnets
W.M. de Rapper

Ph.D. thesis, University of Twente, Enschede, the Netherlands

ISBN: 978-90-365-3657-8

Printed by Drukkerij Best, Eindhoven, the Netherlands

THERMAL STABILITY OF Nb_3Sn RUTHERFORD CABLES FOR ACCELERATOR MAGNETS

PROEFSCHRIFT

ter verkrijging van de graad van doctor
aan de Universiteit Twente, op gezag van
de rector magnificus, prof. dr. H. Brinksma,
volgens besluit van het College voor Promoties
in het openbaar te verdedigen op
vrijdag 2 mei 2014
om 12:45 uur

door

Willem Michiel de Rapper
geboren op 12 februari 1982
te Heusden

Dit proefschrift is goedgekeurd door de promotor en assistent-promotor

prof. dr. ir. H.H.J. ten Kate
dr. M. Dhallé

Preface

This work is a thesis for a doctoral defense, aiming at sufficient argumentation to defend the conclusions and to have an engaging discussion. However, care has been taken to include also sufficient background of the subject discussed, with the aim that someone working in the field of applied superconductivity can read this work without needing to search for the cited literature.

For quick reference to information in this work the next paragraph gives a rough overview of the contents.

Reading guide
The first chapter is written as an introduction to superconductivity and thermal stability. It starts with a brief introduction to superconductivity in general and focuses more on the specifics of the thesis towards the end. This chapter might be less interesting for readers already familiar with superconductors, they can jump to section 1.3. If you happen to be also familiar with accelerator magnets please start reading at section 1.4. It is advised that the reader at least reads section 1.4.2, in which the term "thermal stability" is defined as used in this work.

In the second chapter the majority of terms and concepts are defined in detail. It is therefore recommended to be read by everybody, regardless of the information sought in this thesis.

Chapters 3, 4 and 5 can be read independently, depending on the interest of the reader. In chapter 3 the models that are available to predict thermal stability are introduced, while in chapter 4 the

methodology of the experiments developed to measure thermal stability is introduced. In chapter 5 additional measurement methods are described used to quantify certain physical properties of the cable samples relevant to thermal stability.

There are three result chapters. The first one, chapter 6, deals with results on topics complementary to thermal stability, but which are interesting nonetheless for magnet design. In the following chapter, the measurements of various material properties relevant for thermal stability are reported. In chapter 8 the results of the thermal stability measurements and calculations can be found. In the first section the thermal stability dependence on various variables is determined, followed by a comparison to the operational conditions in accelerator dipole magnets and a comparison to previous results.

In section 8.2 the models described in chapter 3 are compared to the measured data. In section 8.2.1 the treatment of several unknowns is discussed and in the following sections the results of the three models are discussed.

In the final chapter the conclusions drawn from both measurements and models are discussed. Furthermore, recommendations for further research to enhance knowledge on stability of accelerator magnets are made.

Details which are needed for replication, but not needed for understanding the work, are put in the appendices at the back to allow for a succinct argumentation.

Contents

Preface **v**

List of symbols **xi**

1 Introduction **1**
1.1 Technical superconductors 2
1.1.1 Limits of superconductivity 2
1.2 Applied superconductivity 5
1.2.1 Nb_3Sn conductors 6
1.2.2 High-J_c Nb_3Sn wires 6
1.2.3 Cabling 8
1.3 Particle accelerators 9
1.3.1 Collider magnets 10
1.3.2 Production and operation 14
1.3.3 Research programs 16
1.4 Stability of superconductors 17
1.4.1 Key stability issues 17
1.4.2 Introduction to thermal stability 23
1.4.3 Current understanding 27
1.4.4 Unsolved issues 30
1.5 Conclusion 30

2 Nb_3Sn Rutherford cables **33**
2.1 Topology 33
2.1.1 Strand geometry 34

2.1.2 Cable 35
2.2 Material properties 40
2.2.1 Electrical resistivity 40
2.2.2 Thermal conductivity 45
2.2.3 Heat capacity 47
2.3 Cable samples 50
2.3.1 Full-size sample 52
2.4 Conclusion 54

3 Thermal stability simulations 55
3.1 CUDI 56
3.2 StabCalc 59
3.3 Analytical estimates 63
3.3.1 Minimum propagation zone 63
3.3.2 Heat capacity estimate 66
3.3.3 Energy estimate 67
3.4 Conclusion 68

4 Sample preparation for the FRESCA cable test facility 69
4.1 Sample preparation 70
4.1.1 Layout 70
4.1.2 Heat treatment 71
4.1.3 Impregnation 71
4.1.4 Instrumentation 73
4.2 Sample holder 77
4.3 Cable test station 78
4.4 Measurement procedures 83
4.4.1 Critical and quench current 83
4.4.2 Minimum quench energy 88
4.4.3 Residual resistivity ratio 90
4.5 Numerical estimates 92
4.5.1 Self-field 92
4.5.2 Transversal pre-stress 93

4.5.3 Heater efficiency 97
4.6 Conclusion 100

5 Complementary measurement techniques 101
5.1 Strand critical current 101
5.2 U-shaped sample holder for cables 103
5.2.1 Adapted point heaters 105
5.3 Adjacent and crossing contact resistance 108
5.4 Conclusion 110

6 Limitation of transport current due to self-field instability 111
6.1 Strand-to-cable comparison 111
6.2 Cable self-field limitation 114
6.3 Conclusion 117

7 Non-uniform cable properties 119
7.1 Critical current distribution in Rutherford cables . . 119
7.2 RRR distribution in Rutherford cables 124
7.3 Conclusion 127

8 Minimum quench energy, measured and calculated 129
8.1 Measurements 129
8.1.1 Transport current dependence 130
8.1.2 Magnetic field dependence 139
8.1.3 Load line dependence 145
8.1.4 Reproducibility 148
8.1.5 Distribution of the magnetic field in an accelerator magnet 152
8.1.6 Comparison to Nb-Ti Rutherford cables . . . 155
8.1.7 Conclusion 156
8.2 Calculated performance 157
8.2.1 Input parameters 157
8.2.2 CUDI 159
8.2.3 StabCalc 162

8.2.4 Analytical approximation 162
8.2.5 Conclusion 164

9 Conclusion **167**
9.1 Thermal stability 168
9.1.1 Transition to collective strand behavior 169
9.1.2 Impact of operating temperature 170
9.2 Modeling thermal stability 170
9.3 Cable performance 171
9.4 Discussion 172
9.4.1 Models 173
9.4.2 Cable properties 174

Appendices **175**

A k_{Cu} fit parameters **177**

B $C_v(B,T)$ of Nb_3Sn **179**

C Discretization 2D MQS approximation **183**

D FRESCA magnetic field and voltage taps **187**
D.1 Voltage tap technology 189

E Self-field calculation **193**
E.1 FRESCA sample 193
E.2 VAMAS Barrel 195
E.3 U-shaped sample holder 197

F MQE maps **201**

Summary **217**

Samenvatting (Summary in dutch) **221**

Acknowledgments **225**

List of symbols

Symbol	Unit	Description
ϵ	m/m, -	Strain
μ_0	$4\pi \cdot 10^{-7}$ N·A^{-2}	Magnetic permeability of vacuum
λ	-	Superconductor fraction in the filamentary zone
ρ	Ω·m	Electrical resistivity
σ	N·m^{-2}	Stress
θ_k	°	Keystone angle
θ_l	°	Lay angle
A	m^2	Surface area
B	T	Magnetic field
B_c	T	Critical magnetic field
B_{cs}	T	Current sharing magnetic field
B_{kink}	T	Transition magnetic field thermal stability regime
B_{low}	T	Magnetic field of lowest quench current
B_{peak}	T	Peak absolute magnetic field
C_v	J· K^{-1}· m^{-3}	Volumetric heat capacity
d	m	Diameter

Continued from previous page

Symbol	Unit	Description
E	V/m	Electrical field
f_{CnC}	-	Cu to non-Cu ratio
f_{Cu}	-	Cu fraction
f_{nCu}	-	Non-Cu fraction
I	A	Current
I_c	A	Critical current
I_{kink}	A	Transition current thermal stability regime
I_{low}	A	Lowest instability induced quench current
I_q	A	Quench current
J	A$\cdot$ m^{-2}	Current density
J_c	A$\cdot$ m^{-2}	Critical current density
J_e	A$\cdot$ m^{-2}	Engineering current density
k	W$\cdot$ K$^{-1}\cdot$ m^{-1}	Thermal conductivity
L_0	$2.44{\cdot}10^{-8}$ W$\cdot\Omega\cdot$K^2	Lorentz number
L_p	m	Transposition pitch
l_s	m	Length between two crossing contacts
n	-	n value
R_a	µΩ	Adjacent contact resistance
R_c	µΩ	Crossing contact resistance
RRR	-	Residual resistance ratio
T	K	Temperature
T_c	K	Critical temperature
T_{cs}	K	Current sharing temperature
t	m	Cable mid thickness
U	V	Potential difference
w	m	Cable width

Chapter 1

Introduction

Thermal stability is a key issue in applied superconductivity and accelerator magnets are no exception. Since superconductors are used in increasingly larger magnet systems, the risks and consequences of an unstable conductor augment as well. At the moment of writing, there is an extensive research program ongoing to develop Nb_3Sn magnets for future accelerators. Therefore, it is an opportune moment to review the thermal stability of the practical superconductors in use. If the superconductor stability is taken into account pro-actively instead of re-actively, time and effort lost due to underperforming magnets can be avoided.

To discuss the concept of thermal stability in Nb_3Sn superconducting accelerator magnets, an understanding of several concepts in superconductivity and accelerators is required. This chapter seeks to provide such background and highlights the motivation and context of the work.

In section 1.1 superconductivity in general is briefly introduced while section 1.2 moves on to applied superconductivity, focusing on wires and cables. Section 1.3 deals with accelerator magnets which constitute the main application area of this thesis.

The first three sections thus provide context for the thermal stability issues in superconductors. Thermal stability itself is presented

in section 1.4 in more detail. In section 1.4.2 the main topic of this thesis is addressed, while in section 1.4.3 the current status of understanding is reviewed. There clearly is a lack of empirical data on the stability of the present generation high-J_c Nb_3Sn superconductors, which is the last motivating factor behind this work.

1.1 Technical superconductors

When certain materials are cooled below their so-called critical temperature, they lose all resistivity for stationary current. This was first observed in 1911 for mercury [1]. This material is not suited for large-scale applications like magnets, due to its low critical field. However, soon after other and more practical superconducting materials were found. Of particular interest are Nb-Ti and Nb_3Sn, their superconducting properties were discovered in 1961 [2] and 1954 [3] respectively. Even though Nb_3Sn was discovered earlier and supports higher temperatures and magnetic fields, it was quickly found that Nb-Ti, because of its ductile nature, is less costly to make and poses less engineering challenges for use in practical applications.

The Nb-Ti alloy has the highest upper critical magnetic field of all known ductile superconductors. For this reason it is the preferred material for many superconducting magnet systems. Thanks to the MRI industry, the production of Nb-Ti wires is a mature and relatively low-cost technology, when compared to other superconducting materials.

1.1.1 Limits of superconductivity

Even though Nb-Ti is more economical and forgiving in use, it has intrinsic limits like all superconductors. There is a limit to the amount of current that can be transported with zero DC resistance. This amount depends strongly on the temperature and the magnetic field in the conductor.

Every superconductor has such an inherent critical surface, which

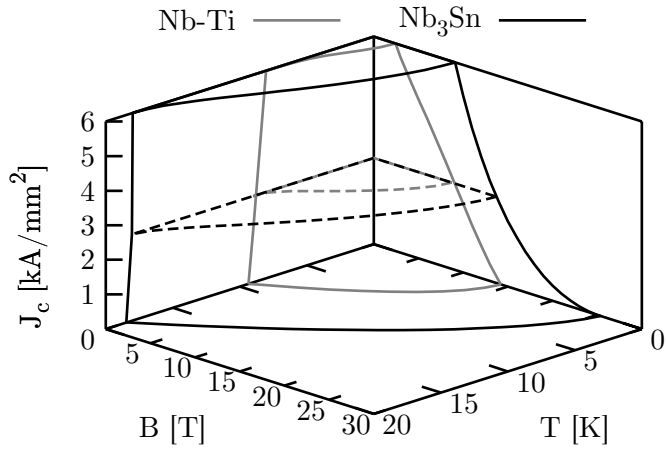

Figure 1.1: The critical current density of Nb_3Sn and Nb-Ti as a function of magnetic field and temperature. The plot is clipped to a maximum J_c value of 6 kA/mm^2 to better show the relevant surface area. The dashed line is the cross section of the critical surfaces at 2.5 kA/mm^2.

is illustrated for Nb-Ti and Nb_3Sn in figure 1.1. Beneath these surfaces the conductors have zero DC resistance, above the surface the resistance is finite. An important feature of the critical surface is the critical temperature T_c at zero current density and magnetic field. T_c is the lower left corner of the critical surface in figure 1.1, the highest temperature at which superconductivity can be found in a certain material.

From the lower left to the lower right corner of the critical surface there is a thick black line denoting the upper critical field B_{c2} as a function of temperature, the $B_{c2}(T)$ curve. This curve shows the maximal magnetic field at which superconductivity can be witnessed in a material for any given temperature. This curve is the absolute limit of the material, and the critical current density in the imme-

diate vicinity of this line is extremely low. In order to increase the critical current density, the temperature and magnetic field need to be decreased.

Table 1.1: Critical temperature, upper critical magnetic field and current density at characteristic working points of several superconductors.

Material	$T_c(B=0)$ [K]	$B_{c2}(T=0)$ [T]	J_c [A/m^2]	T [K]	B [T]
Nb-Ti	9.2	14.6	$2.3 \cdot 10^9$	1.9	9
Nb_3Sn	18.3	26-30	$2.5 \cdot 10^9$	4.2	12
MgB_2	39	15	$1.0 \cdot 10^9$	20	2
YBCO	93	~ 120	$15 \cdot 10^9$	4.2	30
BSCCO 2212	95	~ 200	$1.5 \cdot 10^9$	4.2	25

Some typical values for T_c and B_{c2} are given in table 1.1. For reference, the maximal current density in insulated copper wires is roughly $5 \cdot 10^6$ A/m^2. The table shows that Nb_3Sn has "better" superconducting properties than Nb-Ti. MgB_2 seems to be better than Nb-Ti as well at certain temperatures, but its upper critical magnetic field is not that much higher. It would be possible to make magnets with comparable magnetic field at an elevated operating temperature, MgB_2 for example, would be suitable for 1-5 T magnets at a 20 K maximal operating temperature.

The two high-temperature conductors have significantly higher critical parameters. However, there are still some engineering challenges to be overcome before wire, cable and magnets of the size and quality required for a collider are available. Therefore, these are out of scope of this work.

Scaling laws
There is a microscopic model describing the origin of superconductivity from the interaction between electrons and the crystal latice, the BCS theory [4]. For engineering purposes the estimates derived from the BCS theory are not sufficiently precise. For this reason empirical scaling laws are developed for all applied superconductors. The scaling laws are used to extrapolate the critical surface of a given conductor from a limited number of known data points. The scaling laws used in this work will be discussed in detail in section 2.2.1.

1.2 Applied superconductivity

The practical result of superconductivity is that a conductor will have zero resistance when carrying a stationary current, as long as temperature, magnetic field, strain and current density remain below the critical surface. For wires or cables, instead of the critical current density the more tangible critical current value I_c is most relevant.

In high-current applications the superconducting material is always shunted by a normal conductor with a low resistance. As explained in section 1.4, the normal conductor is needed to stabilize and protect the superconductor. It is required to dissipate the stored energy in the conductor more gradually, since superconductors have a high normal resistivity in combination with poor thermal conductivity. Normally copper or aluminum is used. Bulk superconductors are unstable, as will be explained in section 1.4.3. Therefore, the superconducting material is divided up in small filaments that are embedded in the metal shunt material. This brings the normal state resistivity of the composite conductor and the instabilities down to a useful level.

When the transport current in the conductor exceeds the critical current, the shunt material carries the remaining (normal) current parallel to the supercurrent. Such current sharing results in ohmic loss in the conductor even though it is still partly superconducting.

1.2.1 Nb_3Sn conductors

Pure Nb_3Sn is brittle when compared to copper or Nb-Ti. The material can not withstand more than about 0.3 % strain without permanent degradation of the superconducting properties. This makes the material completely unsuitable for straight forward wire drawing techniques as the ones used for the production of Nb-Ti wires. However, both Nb and Sn are ductile. A copper wire containing niobium and tin in some form can be drawn to wires. The tin in the wire can be present as pure tin, dissolved in the form of bronze, or in powdered $NbSn_2$. Once the wire is drawn and shaped in the desired geometry, it undergoes a diffusion reaction heat treatment at ∼650 °C to obtain the superconducting Nb_3Sn phase.

Tin also readily diffuses through copper at these temperatures. This effect is used in internal tin wires. Rods of niobium are placed in a copper matrix next to rods of tin, and the tin diffuses via the copper into the niobium to form Nb_3Sn. However, even small concentrations of tin significantly increase the resistivity of the copper matrix at 4 K [5]. To keep the tin from diffusing through the entire copper matrix, diffusion barriers are introduced. Commonly tantalum or niobium foil is used for this purpose.

1.2.2 High-J_c Nb_3Sn wires

There are several production processes for Nb_3Sn conductors. For high-J_c wires the best performing options presently available are the Powder-In-Tube (PIT) method and the Re-stacked Rod Process (RRP). Both are briefly discussed here. For applications which require low AC-loss, such as pulsed coils, bronze wire is used since it generally allows for finer filament size. The powder in tube process consists of stacking several tubes of niobium placed in a copper cylinder. The tubes are filled with tin or a tin-rich mixture of niobium and tin. The cylinder is welded shut and drawn to several kilometers of wire.

The RRP process starts with a copper block comprising niobium and tin cylinders, which is extruded over several meters. This cylin-

der is cut in sections and wrapped in a diffusion barrier of Ta or Nb, before being re-stacked in a pure copper matrix and then extruded further and finally drawn to several kilometers of wire.

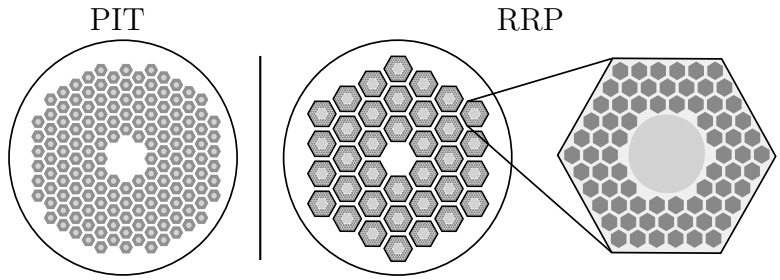

Figure 1.2: Drawing of the wire cross sections, the PIT type wire is illustrated on the left and the RRP type on the right. Dark gray is niobium, gray is tin or tin compound and light gray is bronze.

A sketch of the wire cross sections are shown in figure 1.2. The Nb_3Sn filaments are relatively small in the RRP strand, but they are so closely spaced that they react into a densely interconnected bundle of filaments during the reaction heat treatment. This so-called sub-element, which effectively acts as a single filament, has a relatively large diameter, in the 50 - 150 µm range. A PIT wire has filaments with a characteristic size of ∼40 µm, they are separated by pure copper and remain separated after reaction heat treatment. An example of a PIT wire cross section with filaments is also shown in figure 1.4.

Cable critical current measurements are commonly compared to the current carrying performance of the constituent wires. If they are reacted together with the cable sample, they will be referred to as witness strands. Such witness samples can be either virgin or extracted. A virgin sample is taken from the normal round wire and an extracted sample is cut from the cable itself.

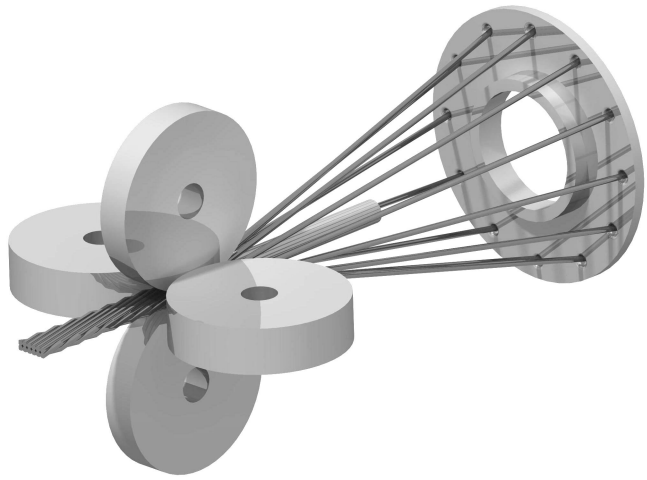

Figure 1.3: Schematic view of the cabling process.

1.2.3 Cabling

As explained further in section 1.3.1, accelerator magnets are built using cables. A wire that is used in a cable is referred to as a strand. The wires are fed from a set of rotating spools mounted on a large disk. The spools rotate at exactly the same speed as the disk to avoid strand torsion. The twist pitch of the cable is then defined by the number of rotations per meter produced cable. The wires are pulled through a braking system to ensure equal tension in all strands. The cable then passes a set of four-rollers called a turks head, as shown in figure 1.3.

The rollers define the "bounding box" of the cable and thus its compaction. The keystone is defined by the angle of the top roller, which can be slightly tilted. The cable is then pulled through a measuring station to check that the dimensions are as specified and is finally stored on a spool.

The highest strand deformation is found in the edges of the cable [6]. At the edges the strands have to make two bends in short succession (see also figure 3.2). Since the tension on each strand is the same, the twisting results in a force along the wide edge of the

Figure 1.4: Cross section of cable sample C (top) and a side view of the same, where the copper matrix is etched away to reveal the Nb_3Sn filaments (bottom).

cable accumulating stress on the side edge of the cable. This results in a shear plane in the strand. If plastic deformation occurs in this shear plane, the filaments can be damaged, resulting in a loss of supercurrent and tin poisoning of the copper. Such plastic deformation is visible in the filaments at the edges of the top cable in figure 1.4.

1.3 Particle accelerators

In circular proton accelerators, as shown in [7], the collision energy E of protons is given by:

$$E = 0.3qBr \quad [\text{GeV}]. \tag{1.1}$$

Here q is the charge of the proton (for H^+ $q = 1$), B is the magnetic field generated by the bending dipoles and r is the radius of the accelerator. Thus the energy can only be increased by increasing B or r.

The LHC bending dipoles are built using Nb-Ti superconductors, which can only reach current densities suitable for magnet design up to 10 tesla at 1.9 K. To raise the magnetic field in the bending dipoles above this level, a different conductor is needed. At the time of writing only Nb_3Sn can reach the required current densities at magnetic fields of 14 to 16 tesla in a cost effective production process.

1.3.1 Magnets for circular colliders

A collider system uses many different types of magnets for the beam optics. Superconductors are mostly used in the dipole and the quadrupole magnets, for beam bending and focusing respectively, since these require a high absolute magnetic field to improve the key accelerator specifications: energy and luminosity.

An example of the dipole coils configuration is given in figure 1.5. Here the coils in a bending dipole magnet are shown. In the LHC the two beams run in parallel and cross at the four collision points. The aspect ratios are off to illustrate the details better, since the coils are in reality approximately 15 meter long and only 12 cm wide. Accelerator systems require magnets with high magnetic field quality. This means that the magnet must have a uniform magnetic field or a uniform magnetic field gradient for dipoles and quadrupoles, respectively. When this is not the case, a small positional deviation of the particle beam brings it in a different magnetic field or magnetic field gradient, steering the beam further off its ideal trajectory.

To achieve a highly uniform magnetic field using a conductor which has a constant current density, the conductor must be placed in a configuration as shown in figure 1.6. This distribution is defined as two overlapping ellipses with equal but inversed current densities [9].

As seen in section 1.2.2, Nb_3Sn conductors are produced as wires.

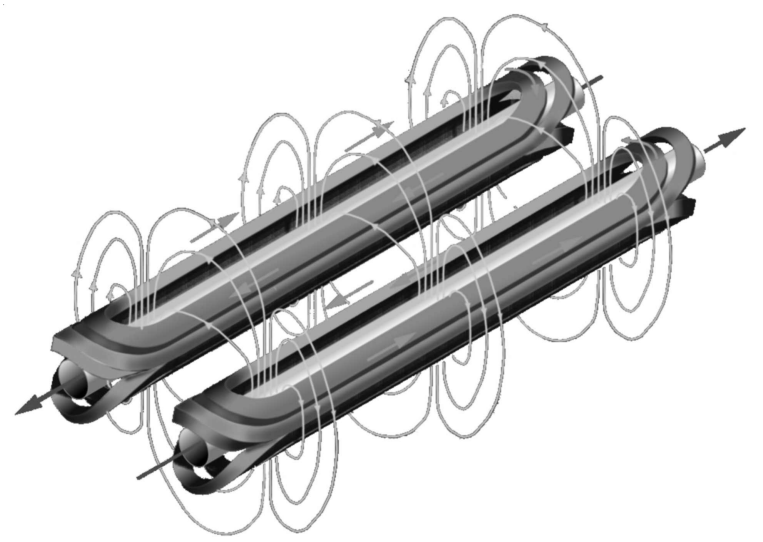

Figure 1.5: Artist impression of two dipole coils and the beam tubes as used in the LHC (courtesy of CERN [8]). The current (gray), magnetic field (light gray) and beam directions (dark gray) are indicated by arrows.

If a dipole magnet is wound from a single wire its self-inductance would be too high and thus the achievable ramp rates unacceptably low. To reduce the self-inductance of the magnet, the coils need to be wound with cables. The cables have a roughly rectangular cross section and are distributed over the cross section to approximate the perfect current distribution.

As an example figure 1.7 shows two coil designs for a 100 mm aperture dipole magnet. The cables are made from 40 1.0 mm diameter strands. The coil on the left is referred to as a $\cos\theta$ design, while the coil on the right is referred to as a block design. Both are viable designs to produce an accelerator dipole, each with different advantages and disadvantages. The $\cos\theta$ design typically results in a more uniform magnetic field while the block magnet may be easier to manufacture and theoretically can support the Lorentz forces more

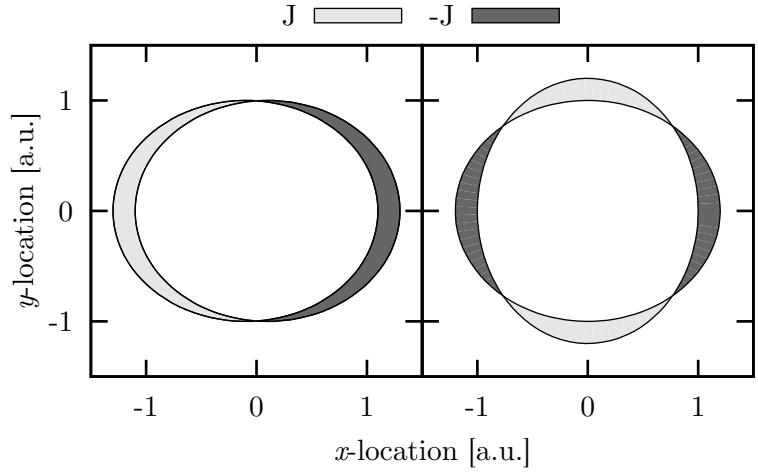

Figure 1.6: Current distribution over the cross section needed to achieve a perfect dipole (left) and quadrupole (right) field, using a homogeneous current density.

efficiently along the straight cross section of the coil. For a more comprehensive discussion of the pros and cons of block versus $\cos\theta$ designs, see [9] and [11].

The cables in a coil need to be insulated, and in the case of brittle superconductors like Nb_3Sn, the strands require impregnation to limit strain induced degradation of the critical current. Therefore, the overall current density of a cable is always lower than the critical current density in a single wire. The average current density in a coil winding including electrical insulation is called the engineering current density J_e. This physical quantity is a good measure for the overall performance of a cable. The engineering current density determines how much surface area is needed in the magnet cross section to reach a certain magnetic field. This has of course a direct implication for the conductor cost of a magnet. A cable which can deliver a higher J_e might be more cost effective even when the cost per meter is higher than a low J_e cable.

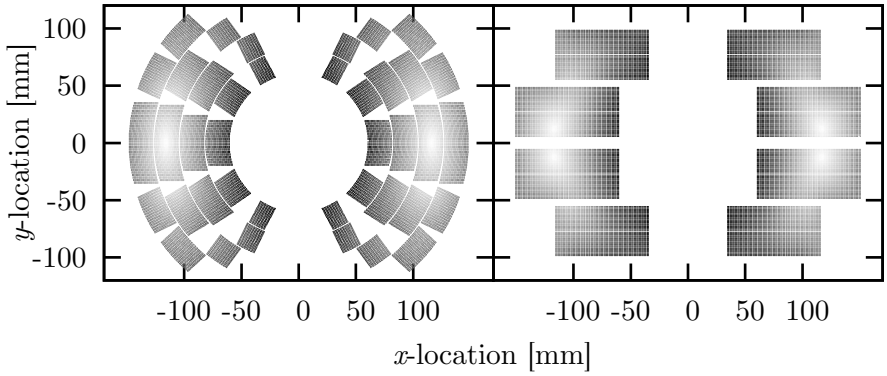

Figure 1.7: Cross section of two common dipole designs [10]. The shade indicates the magnetic field strength. On the left a $\cos\theta$ design and on the right a block design is shown.

As can be seen in figure 1.7, in the cross section of the coil every magnetic field value from zero to peak magnetic field is encountered. Peak magnetic field B_{peak} is the highest absolute magnetic field found in the conductor. The peak magnetic field is higher than the nominal magnetic field in the bore of the magnet, depending on the size of the bore and on the shape of the winding pack.

Superconducting magnets are inherently limited by the performance of the superconductor in the peak magnetic field location. The peak magnetic field is always at the same location in the coil cross section but its value depends on the current. There is a linear relation between the B_{peak} and the current, the so-called load line. A magnet is ultimately limited to the current where the load line crosses the critical surface of the superconductor, but in practice will be operated well below this value since an operational margin is required for stability reasons.

1.3.2 Production and operation cycle of Nb_3Sn collider magnets

Thermal stability is just one aspect of magnet design. There are other, sometimes even conflicting boundary conditions that need to be met. Several limitations arise from the production and the operation of a Nb_3Sn dipole magnet, which have to be taken into account during the design. These are discussed here to explain the choice of sample preparation and model boundary conditions later.

Assembly of Nb_3Sn magnet systems

To ensure that the results obtained are relevant for functional magnet systems, the material choices are quite limited. This is caused by the production and operation cycles of Nb_3Sn accelerator magnets. Materials used in Nb_3Sn coil windings must withstand temperatures ranging from 650 C to 2 K. The remaining materials used in the magnet system need to withstand temperatures from room temperature to 4.3 K. The parts which are in direct contact with the coil must have a comparable thermal contraction to the wire, so that the conductor is not damaged by thermal stress.

The only proven insulation for a wind-and-react coil is glass fiber sleeves or wrap, possibly including a mica film, impregnated with epoxy resin. The glass fiber can withstand the heat treatment and when it is filled with epoxy resin after the reaction heat treatment, it will have sufficient electrical resistance for magnet operation.

A react-and-wind coil can be insulated by a different material such as polyimide tape. However, this method of winding only works well for coils with a large radius. Furthermore, the conductor still has to be impregnated for the Nb_3Sn to withstand the stresses that build up during operation.

Electrical insulation and impregnation greatly reduce the thermal contact between the cabled conductor and the helium bath. From a thermal stability point of view, cooling should be inhibited as little as possible. There is research in progress on various new impregnation types. Two possibilities which have the potential to improve the

thermal stability are loaded epoxies [12] and porous ceramic insulation [13]. Unfortunately there have been no tests with coils made from cabled conductor using these materials.

Loaded epoxies are epoxies for example filled with rare earth sulfur-oxide particles, which have a peak in specific heat at cryogenic temperatures. Their implementation looks promising [14], but no experimental evidence of increased thermal stability in Nb_3Sn coils is as yet available.

Ceramic insulation is made by coating glass fiber tape in a ceramic compound, which sinters to a solid during the heat treatment of the Nb_3Sn. However, so far this insulation is relatively thick, brittle and seems to lack the structural support that Nb_3Sn conductors need [15].

Magnet operation

A linear increase of current over time is used to drive an accelerator magnet to a new magnetic field set point. This is commonly referred to as a ramp up or down for an increase or a decrease of the current, respectively. The rate at which this happens is referred to as the ramp rate, measured in A/s. An accelerator magnet has to be charged at $\sim$10 A/s to follow the energy ramp of the particle beam contained by the magnet. This is why low self-inductance magnets are needed in accelerator systems. If the magnets can ramp faster, the beam can be brought to a higher energy faster. This decreases the setup time between active measurements and thus increases the total availability of the machine for high energy physics experiments.

As was stressed before, superconductors only have zero loss for stationary currents. When the magnets are ramped up or down the changing magnetic field induces a loss in the conductor. The main loss component arises from induced coupling currents in the cables [16]. To minimize this, the electrical contacts between the wires in the cable need to be minimized. This will be discussed in more detail in section 2.1.2, where some minimal contact resistance values are given.

Not only do these induced coupling currents imply a load on the cryogenic system, but they also disturb the current distribution in the cable, which gives rise to magnetic field errors. Such current redistribution effects are therefore unwanted in accelerator magnets. However, as will be shown in section 1.4.2, current redistribution at some level is needed for thermal stability. The design values of electrical contacts in a Nb_3Sn cable are a fine balance between thermal stability on one hand and coupling currents on the other.

There are two practical methods to increase the inter-strand resistances: covering the strands with a coating or inserting a core into the cable. Both significantly reduce the ramp loss in Nb_3Sn Rutherford cables [17]. In the LHC a AgSn coating is used on the Nb-Ti strands to reduce the contact resistances to an acceptable level. The downside of using a coating is that both the adjacent and the crossing contact resistances are affected. A core consists of a ductile resistive material, typically a stainless steel strip, inserted between the strands during the manufacturing of the cable. This reduces only the crossing contacts and keeps the adjacent contacts as is.

It is important to note that in Nb_3Sn Rutherford cables the material choice for the coating or the core is limited due to the heat treatment. The coating used in the LHC would diffuse into the copper matrix during the heat treatment. Common coatings for Nb_3Sn are chromium and nickel, used extensively in the cable-in-conduit conductors designed for pulsed magnets. Also other non-conductive materials seem promising [18].

1.3.3 Research programs

There are currently a few running research programs geared towards the advancement of accelerator technology in light of the planned LHC upgrades. They cover all aspects of the accelerator. The programs relevant for this work are the EU funded CARE and EuCard programs and the US LHC Accelerator Research Program (LARP).

The CARE/NED program was set up to develop high-field magnets for the LHC upgrade [19], but curbed to thermal studies, design

optimization and conductor development [20]. Its successors are the EuCard projects which is in progress: the conductor development is done partially in the Short Model Coil (SMC) program [21]–[23], which aims to gather knowledge and experience in the manufacture and operation of Nb_3Sn dipole coils. Several cables from this program have been tested in the FRESCA cable test facility at CERN [24].

The first of several possible LHC upgrades is the luminosity upgrade. There are two parts in this upgrade which are relevant to Nb_3Sn magnet design; the insertion quadrupole magnet upgrade and a shortened dipole project for 11 T [25].

LARP [26] comprises a quadrupole R&D project, which has already delivered a number of magnets [27]. The focus of this program is to aid the luminosity upgrade of the LHC. For this upgrade quadrupoles with a gradient in excess of 200 T/m are planned.

In the far future a Nb_3Sn upgrade, possibly in combination with high T_c materials, is envisioned [28]. This energy upgrade does not have a fixed time line, whereas at the writing of this document the luminosity upgrade is planned to be ready medio 2022.

1.4 Stability of superconductors

In applied superconductivity the terms “instability” and “stability” are used to describe the capacity of a system to remain in- or to recover to its nominal operating conditions after an internal or external perturbation. An instability issue will bring the superconductor to the normal state unless certain conditions are met. A stability issue defines the energy needed to bring the conductor from the “metastable” superconducting state to the normal conducting state.

1.4.1 Key stability issues

In the context of superconducting magnets, there are three mechanisms which are commonly referred to as instability, see figure 1.8.

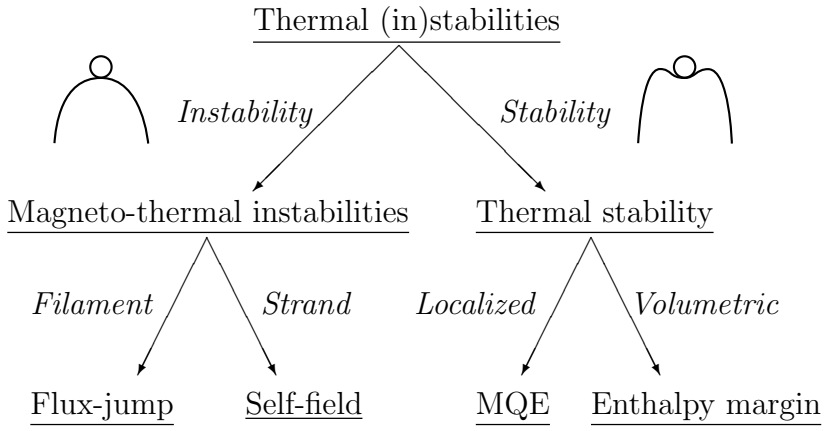

Figure 1.8: Flow chart showing the relation between the terms commonly referred to as (in)stability in superconductors.

Their common denominator is that they can cause a full return to the normal state of the superconductor via a positive feedback loop. They can be further subdivided into two categories. The first category are the so-called magneto-thermal instabilities. These instabilities are closely linked to local changes in magnetic field inside the superconductor. The second group is thermal stability, which could be named electro-thermal stability analogous to the previous category, since the positive feedback loop arises from the interplay between temperature and electric currents in a superconducting wire.

The first category are true intrinsic instabilities. Under certain conditions the conductor will be unstable and return to the normal conducting state. The second category is an extrinsic stability problem. The conductor is intrinsically stable, but can be brought to the normal state by a small starting energy, which is many times smaller than the energy needed to heat the entire conductor to the critical temperature. The minimum starting energy that initiates a transition to the normal state via electrical effects is called the minimum quench energy (MQE). For completeness, figure 1.8 also includes the

volumetric energy needed to bring a volume of a conductor to the normal state, which is referred to as the enthalpy margin.

Flux-jump instability

Bulk superconductors placed in a magnetic field can be unstable and spontaneously revert to the normal state due to flux-jump instabilities [29]. This type of instability arises from the relative low heat capacity of the strand materials at liquid helium temperatures in combination with the energy built up while expelling the magnetic field. These effects are most dominant at low applied magnetic field values (B<3 T). They were removed completely initially by drawing a superconductor to sufficiently small diameter wires [30]. The invention of the multi filamentary wire [31] made it possible to remove these instabilities altogether [32], while maintaining a sufficiently large wire to use in cabling.

Flux-jumps are well understood, for a comprehensive overview see [9], chapter 7, here a summary is given for convenience. When a piece of superconductor is magnetized, the shielding currents have a current density of J_c [33]. The amount of magnetic flux that is expelled from the conductor is therefore directly linked to the critical current density.

If by a random fluctuation the temperature in the conductor rises, the critical current density decreases. The amount of expelled magnetic flux then also decreases. Due to the accompanying release of flux pinning energy, the change in magnetic flux results in a temperature increase. This positive feedback loop continues when the heat generated by a change in temperature is larger than the heat needed to increase the temperature by the same amount. Putting this more precisely [9]:

$$\frac{\mu_0 J_c^2 d_f^2}{12(T_c - T_{bath})} \cdot \Delta T > C_v \cdot \Delta T \quad [\mathrm{J \cdot m^{-3}}]. \tag{1.2}$$

Here d_f is the diameter of the superconducting filament, C_v is the volumetric heat capacity and ΔT is an arbitrary small temperature

increase. The left hand side represents the heat generated due to the change in magnetic flux caused by the temperature increase, while the right hand side represents the heat needed to achieve the same temperature increase. When this inequality is satisfied the conductor is unstable. Equation 1.2 can be rewritten as a stability condition:

$$J_c \cdot d_f < \sqrt{12 C_v (T_c - T_{bath})/\mu_0} \quad [\mathrm{A/m}]. \tag{1.3}$$

When this inequality is satisfied the superconductor will not experience flux-jumps. This equation is commonly referred to as the adiabatic filament stability criterion. The only physical quantity which is not a material property is d_f. To avoid flux-jumps, the size of the superconducting elements in a composite wire must be reduced to a value that satisfies equation 1.3. Besides removing flux-jump instabilities the superconductor can also recover more easily from external influences due to the improved conduction cooling [34].

As an example, a strand in a winding at a nominally low magnetic field must have fairly small filaments; using the material properties at 2 tesla, C_v is $5 \cdot 10^3$ J·m^{-3}, T_c is 17.6 K and J_c is $19.3 \cdot 10^9$ A·m^{-2}, it is found that the filament diameter needs to be less than 40 µm at 2 T.

It is important to note that T_c and J_c are material properties which depend on the value of the magnetic field. A typical operating point for Nb_3Sn is 12 tesla and 4.3 kelvin. Under these operating conditions C_v is $5 \cdot 10^3$ J·m^{-3}, T_c is 12.8 K and J_c is $2.5 \cdot 10^9$ A·m^{-2}. To satisfy equation 1.3, the filament diameter therefore has to be less than 250 µm at 12 T. So flux-jumps are mostly an issue during the ramp up of the magnet and in the low magnetic field windings.

Equation 1.3 assumes the system to be fully linear and adiabatic, which is a valid worst-case approximation at high magnetic fields. However, as will be shown in section 2.2.3, the heat capacity increases rapidly with temperature. When the heat capacity starts to increase during a flux-jump, it is possible that equation 1.3 is suddenly satisfied and the flux-jump stops before the superconducting state is fully lost. This is referred to as a partial flux-jump.

The conductors in this work all have superconducting element sizes of less than 50 µm. For $d_f = 50$ µm these conductors are stable above 2.7 tesla. At magnetic fields below this, the conductor has to rely on the increasing heat capacity to withstand flux-jumps.

Wire self-field instability

This is an instability that arises from non-uniform current distribution in superconducting wires at low magnetic field. Because of the high critical current densities at low magnetic field and the skin effect, the current is distributed in a thin band in the outer filaments of the wire. Even though the conductor would be stable with a uniform current distribution, it is not stable with such a non-uniform current distribution [35]. A brief summary of the underlying causes will be given here for convenience.

If a superconducting wire is placed in a magnetic field varying over the length of the wire, the conductor will be limited in the point that experiences the highest magnetic field. At this point the critical current equals the transport current of the wire. In the rest of the wire the critical current can be much higher, as shown in section 1.1.1. The skin effect will force the current initially to flow in a thin shell on the outer edge of the filamentary zone inside the wire. Since superconductors have no DC resistance, there is no driving force causing the current to diffuse over the full cross section of the wire. Therefore, there is a thin shell of current at the outer edge of the wire in the locations where the current is significantly smaller than the critical current.

In this situation the center of the strand does not experience any magnetic field generated by the current which it is carrying, the so-called self-field of the wire. When the current redistributes slightly inwards, due to a random temperature fluctuation, more of the superconductor in the wire experiences the self-field. This magnetizes the superconductor which in turn generates a loss, which results in a higher temperature, so that a positive feedback loop is once more established.

The stability condition against such self-field instability is taken from reference [9]:

$$\frac{\mu_0 \lambda^2 J_c^2 d^2}{4C_v(T_c - T_{bath})} < \left[-\frac{1}{2}\ln\epsilon - \frac{3}{8} + \frac{\epsilon^2}{2} - \frac{\epsilon^4}{8} \right]^{-1}. \tag{1.4}$$

Here d is the diameter of the filamentary region, λ is the fraction of non-copper material in the filamentary zone and ϵ is defined as $\epsilon = d_{cur}/d$, where d_{cur} is the inner diameter of the current shell in the strand. This ratio can be expressed as $\epsilon = \sqrt{1-i}$, where i is the reduced current $i = I/I_c$. Assuming a wire is operated at a fixed fraction of its critical current, say 80%, the value for ϵ can be solved, in this example as $\epsilon = 1 - 0.8^2 = 0.36$. With this assumption equation 1.4 can be expressed as:

$$J_c d < \sqrt{\frac{4C_v(T_c - T_{bath})}{\mu_0 \lambda^2} \cdot f(i)} \quad [\mathrm{A/m}], \tag{1.5}$$

$$\text{with } f(i) = \left[-\frac{1}{2}\ln\sqrt{1-i} - \frac{3}{8} + \frac{(1-i)}{2} - \frac{(1-i)^2}{8} \right]^{-1}. \tag{1.6}$$

Note that equation 1.5 is very similar to the adiabatic flux-jump stability condition in equation 1.3. For a wire operated at a reduced current of 0.8, at a T_{bath} of 4.3 K and an applied magnetic field of 12 T and with material properties of λ is 0.9, C_v is $5 \cdot 10^3$ J·m^{-3}, T_c is 12.8 K and J_c is $2.5 \cdot 10^9$ A·m^{-2}, the maximal filamentary diameter is 0.5 mm. This implies that the wires used in this work (1.25 and 0.7 mm) should not be stable. This is partly true, some samples do show self-field limitations as will be shown in chapter 6.

However, equation 1.4 is a pessimistic estimate, since it assumes adiabatic conditions. Furthermore, it neglects the perturbation energy required to trigger an self-field instability. This requires a numerical model [36]. When the current in a strand is increased it may cross the stability threshold as defined in equation 1.4, at this point the strand is unstable, but requires a perturbation to trigger the instability. Therefore, repeated measurements will result in a range

of quench currents. The minimum quench current is the current at which the strand or cable first becomes unstable.

A low matrix resistivity (high RRR value) also reduces the instabilities by increasing the required perturbation energy to trigger a self-field instability [37].

In short, there are currently two options to counter these instabilities: 1) use a lower-resistive matrix material to increase the energy needed to trigger an instability and 2) decrease the wire diameter to decrease the energy contained in the self-field per unit wire length. A third option which has shown good results, but may be difficult to implement in magnet design, is to force the current distribution [38]. Self-field instabilities are still an issue in the present generation of Nb_3Sn wires.

Thermal stability

The previous two mechanisms arise from intrinsic properties of the superconducting material and of the superconducting wire respectively. Thermal stability, on the other hand, is defined as the amount of external energy required to trigger an irreversible return to the normal state. This amount depends on the operating conditions of the conductor (current, magnetic field, temperature and cooling). Therefore, it heavily depends on the design and operation of a magnet system. These temperature excursions are the main subject of this work.

1.4.2 Introduction to thermal stability

A thermal perturbation can take many forms (electrical, mechanical or radiation) and can have many causes (induced current, EM forces and beam losses as respective examples). They all have the same result: an increase in temperature. Due to the low heat capacities of the constituent materials at these temperatures, small amounts of energy $\sim$100 µJ will result in appreciable temperature rises. This can cause a transition to the normal state, resulting in joule heating. This results in a further increase of the temperature, bringing an even larger volume of the conductor into the normal state.

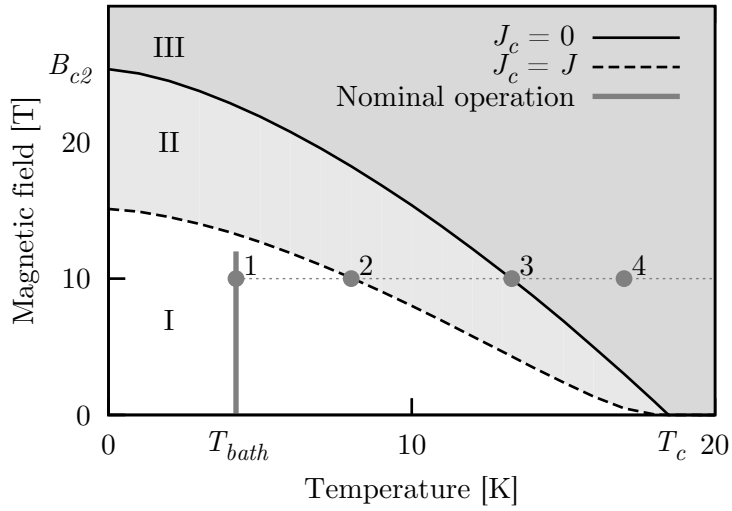

Figure 1.9: Critical surface and current sharing surface as a function of temperature and magnetic field. The continuous gray line represents a magnet operating at a fixed current density with a peak magnetic field of 12 telsa. The dotted line indicates a perturbed wire in the magnet at a location where the magnetic field is 10 tesla.

A schematic view of a thermal stability excursion in a magnet under nominal operating conditions is shown in figure 1.9, which is a "top down" view of figure 1.1. A magnet is operating with a current density of J, at a bath temperature of 4.3 kelvin and a peak magnetic field of 12 tesla. As discussed in section 1.3.1, the conductor in a coil will encounter every magnetic field value from zero to the peak magnetic field. The continuous gray line represents all possible operating conditions in a stable magnet.

Suppose that a section of a strand in a magnetic field of 10 tesla (1) is perturbed and the temperature increases along the dotted line. If the temperature stays below point 2, the conductor will recover, since the critical current density is still larger than the current density (area I). When the strand is heated beyond this point, between 2

and 3, there is heat generation inside the strand due to ohmic loss (area II), since part of the current is carried by the normal matrix. Point 2 is commonly referred to as the current sharing temperature T_{cs} of a conductor. The current sharing temperature is a function of magnetic field, see the dashed line in figure 1.9, but also of current density.

The internal heat generation will increase from zero at point 2 to its maximal value at point 3. When point 3 is passed the strand is completely in the normal state (area III). From this point onward the heat generation in the strand will remain approximately constant, only changing due to the temperature dependence of the matrix resistivity.

Note that the parts of the conductor operating in a lower magnetic field have a much larger temperature margin before they reach the dashed current sharing line. The temperature difference between the operation temperature and the current sharing temperature is often referred to as the temperature margin of a conductor. This is a crude measure for stability and is useful for qualitative comparison of magnet designs.

Any practical magnet design enforces operation at a significantly lower peak magnetic field than dictated by the critical surface of the conductor. This is to allow some temperature margin in the parts of the conductor operating in the peak magnetic field.

Once the initial perturbation is over, there are two competing factors that determine whether the superconductor will recover or will completely transfer to the normal state: the internal heat generation and the cooling. If the heat is removed faster than it is generated, the conductor will return to the nominal operating conditions. Because of the strong positive feedback between temperature and heat generation, it is impossible to have a stable normal zone is present inside a conductor. It will either expand or collapse.

This process is summarized in the overview of the thermal stability cascade depicted in figure 1.10. An initial perturbation acts on a strand, generating a normal zone in the strand. This Normal

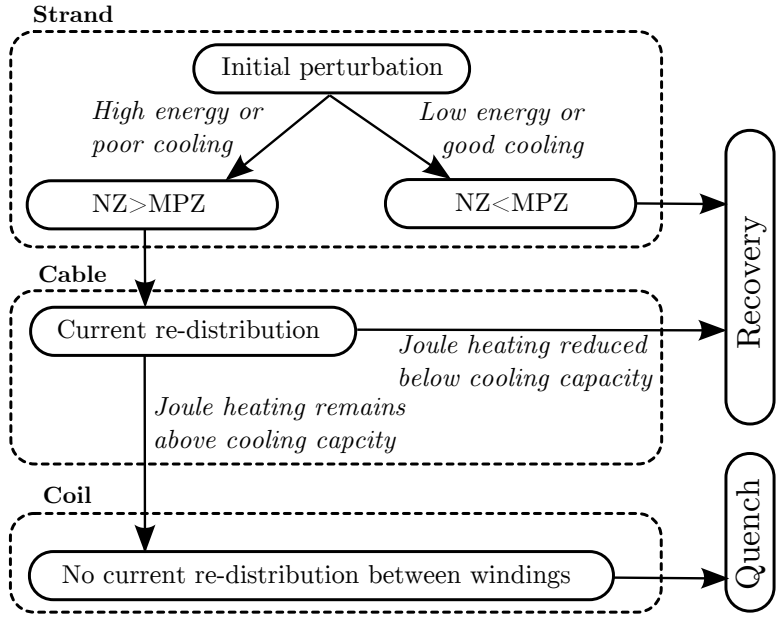

Figure 1.10: Schematic view of a thermal stability process in a superconducting magnet. It starts with an initial perturbation at the strand level and either recovers or escalates to a higher level of complexity.

Zone (NZ) is either larger or smaller than the Minimum Propagation Zone (MPZ). The minimum propagation zone is per definition the size which determines whether a normal zone will collapse or not. If it does not collapse (NZ>MPZ), the current will start to redistribute around the NZ. This happens because the material in the normal state has a finite resistivity, while the material around it is still superconducting. This process is limited by the resistances between the strands and by the self-inductance of the current paths. If the joule heating is reduced below the cooling capacity before more strands in the cable reach the normal state, the cable recovers. If the normal zone starts to spread uncontrollably to neighboring strands, the entire cable cross section will quickly revert to the normal state and

the normal zone will start to spread over the length of the cable. At this point the geometry of the coil becomes relevant. Unfortunately, there is no mechanism to redistribute current over different cables in an accelerator magnet, therefore a cable quench will always lead to a magnet quench.

In short; there are two ways in which an accelerator magnet can recover from an external perturbation. If the limits of these two mechanisms are calculated, the thermal stability of the entire accelerator magnet is known.

1.4.3 Current understanding

Magneto-thermal effects in wires are well understood, as discussed in section 1.4.1. The following sections will show what the state-of-the-art is in the understanding of the thermal stability in cables, either in terms of modeling or of empirical data to back up the models.

Modeling: Analytical approach

The thermal stability of single strand systems may be predicted analytically, by linearizing the temperature dependence of the material properties. This approach is accurate for systems built from a single superconducting wire. It is still valid for cables operated with low temperature margin, i.e. in the regime where the cable can not support the failure of a single strand. The thermal stability of the cable is then limited to the thermal stability of a single strand.

The first-order approach is to estimate size of the MPZ and then to calculate the enthalpy needed to raise this volume of material to the current sharing temperature [9]. A variation on this method is described in section 3.3 and will there be discussed in more detail.

A more elegant solution is to solve the heat equation over a one- or more dimensional structure, incorporating a temperature-dependent heating term. A comprehensive review of such stability calculations may be found in reference [39].

Modeling: Numerical approach

The interaction between strands in a cable has been found too complex to express in a set of analytical equations. Therefore, a numerical calculation is needed. Two well-documented numerical models used to predict stability may be found in references [40], [41].

The first model [40] calculates the stability of a wire in a cable assuming the wires to be one-dimensional. One wire is connected laterally to two groups of two wires. These two groups are then thermally and electrically connected to an even larger group, which contains the rest of the wires in the cable. This significantly reduces the numerically load, but does not allow for accurate calculations in situations where the thermal margin is such that the cable can recover from multiple strands with a normal zone.

The second network type model is named CUDI [41] and is also used for calculations of thermal stability in this work. CUDI is described in section 3.1. This model takes every strand in the cable into account separately. Furthermore, it takes the cable geometry into account as well as any relevant electromagnetic or thermal interaction that can occur in a Rutherford cable.

Available empirical data

Minimum quench energy measurements are rare. There is some work performed on single wire systems [42], [43]. However, thermal stability measurements on high-J_c Nb_3Sn Rutherford *cables* are not available.

Thermal stability of Nb-Ti Rutherford cables has been measured directly [44]–[47]. Two PhD theses are issued cover this topic [48], [49]. The knowledge gained in [49] is used as a starting point for the design of the experimental setup described in chapter 4.

Nb_3Sn Rutherford cable testing setups

In general, relatively few cable tests have been performed on Nb_3Sn Rutherford cables due to the large effort and time needed to prepare samples. Usually only extracted strands are measured to estimate the cable performance. There are several ways to test the performance

of an actual Rutherford cable.

A setup can be conceived in which a single strand inside a cable is powered [15], [50]. This allows to test cables without the need for a large power supply or a superconducting transformer. However, this method is not suited for MQE measurements since the presence of the unpowered wires is not representative for a cable in a magnet system.

The next step upwards in complexity is testing of a short sample exposed to a magnetic field provided by a solenoid magnet and with a transformer connected to the sample to generate the sample current. This method allows to test only a short sample length, since the applied magnetic field area is less than the bore diameter. One version is built using straight samples passing through a split solenoid [51]. Another version is a U-shaped sample holder developed at the University of Twente [52]. The latter one will be discussed in section 5.2 as it is used for thermal stability studies presented in this work.

A cable can also be tested by constructing a short racetrack coil [23], [53]. This method circumvents the need for a purpose built test station, but the cable can only be measured following the load line of the test coil. This does not allow for a full exploration of the performance limits of the cable, but on the other hand has the advantage that it provides a validation of the preparation method as well as the performance of the cable at the working point of the full-size magnet. The access to the cable surface is limited and the current and magnetic field can not be changed independently. This makes this method unsuited for in-depth thermal stability research.

Finally, a dipole magnet can be used to test a straight cable sample over a longer length. A direct power supply is included for sample powering. A few of such systems are currently in use, as for example the cable test facility at LBNL [54] and the FRESCA test station at CERN [24]. The latter will be presented in section 4.3 as it is used in the thermal stability tests performed for this work. Both test stations were originally designed for Nb-Ti cable testing, but new tooling is developed to allow for Nb_3Sn tests [55]–[58].

1.4.4 Unsolved issues

There are models developed which should in principle be capable to predict the thermal stability of Nb_3Sn Rutherford cables. However, no empirical data are yet available to validate them on this material.

There are some data available for impregnated Rutherford cables, but made from Nb-Ti. In Nb_3Sn cables the current density is much higher, which may be expected to significantly decrease their thermal stability. However, from a thermal stability point of view there are also improvements when moving from Nb-Ti to Nb_3Sn technology; the temperature margin is much higher and inter-strand contacts are copper to copper without coating. Both effects can significantly increase the thermal stability.

To validate the prediction of the thermal stability of Nb_3Sn based accelerator magnets, a comprehensive set of empirical data is needed, which is presently absent.

1.5 Conclusion

Due to the requirement of high current density, superconductors are the most energy efficient conductors to use in dipole and quadrupole magnets for high energy circular particle colliders. The collider with the highest energy at the time of writing is the LHC, which for this reason is built with Nb-Ti based magnets. There are upgrade plans for the LHC which call for a superconductor with a higher critical magnetic field than Nb-Ti. Currently Nb_3Sn technology is the main candidate for the upgrade since it is both mature and cost effective.

Stability is an issue in all superconducting systems, especially in low-T_c superconductors like Nb_3Sn. Due to the low heat capacity of the materials at 2 to 4 K, a relatively small amount of energy of 10-100 µJ may already be sufficient to destroy the superconducting state in part of the conductor. The resulting normal zone will expand through electrical dissipation, possibly bringing the entire coil to the

normal state. The amount of heat that a superconductor can absorb without going into this cascading effect is called the thermal stability margin.

For magnet design it is crucial to know the thermal stability and how to improve it. It can be estimated using analytical or numerical models. This subject has been studied well for Nb-Ti coils, however for high-J_c Nb_3Sn Rutherford cables there are no empirical data available to validate the models.

To this end a project is set up to measure the thermal stability of several state-of-the-art Nb_3Sn cables and a summary of the scientific findings are reported in this thesis.

Chapter 2

Nb_3Sn Rutherford cables

In this chapter the essential properties of Rutherford cables and their strands are described, as well as how these properties are introduced into various models developed to simulate their behavior.

After briefly discussing the geometrical properties of strands and cables in section 2.1, the second section, 2.2, considers the thermal and electrical conductivities and heat capacity. At cryogenic temperatures, all these physical quantities are strongly influenced by the temperature, by the Residual Resistance Ratio (RRR) and by the superconductor to normal transition of the Nb_3Sn filaments.

In the final section, 2.3, the cable samples that were investigated in this thesis and their properties will be presented.

2.1 Topology

Accelerator systems require magnets with a high magnetic field uniformity and relatively high ramp-rates, as explained in section 1.3. To meet both requirements, a twisted cable is required. Cabling is needed because a coil made from a single wire has a too high self inductance to allow for the necessary ramp-rates, while twisting the cable is required to control and to reduce ramp losses and magnetization effects, which can disturb the magnetic field quality.

The cable can be described as a number of strands repeating the same pattern over the entire length of the conductor. This section will define the minimum set of parameters needed to describe the path of a superconducting strand in a Rutherford cable.

2.1.1 Strand geometry

The main geometrical strand parameters are its diameter d and its copper to non-copper ratio f_{CnC}. This is the ratio between the cross-sectional surface areas of the copper and the non-copper components of the strand. There are two other closely related fractions: the copper content, f_{Cu} and non-copper content, f_{nCu}. They are useful in later calculations and defined as follows:

$$f_{CnC} = \frac{A_{Cu}}{A_{nCu}} \quad [-], \tag{2.1}$$

$$f_{Cu} = \frac{f_{CnC}}{1 + f_{CnC}} = 1 - f_{nCu} \quad [-], \tag{2.2}$$

$$f_{nCu} = \frac{1}{1 + f_{CnC}} = 1 - f_{Cu} \quad [-]. \tag{2.3}$$

Here A_{Cu} is the surface area of copper and A_{nCu} is that of non-copper material in the strand's cross section. The f_{CnC} lies for most practical superconductors between 0.5 and 2.0, depending on the type of material used and the application. For Nb_3Sn accelerator magnets, the value usually lies between 1.0 and 1.5. For production reasons it is hard to achieve a value lower than 1. If the value is relatively high, the engineering current density is relatively low and the coil needs significantly more conductor. These limits are not hard but essentially design choices that depend on the priorities of the design.

Other geometrical properties are the number of filaments, the spatial distribution of the filaments in the strand's cross section, the presence of diffusion barriers and the average filament diameter. These properties are only relevant for magnetization and will not be discussed, as they are not expected to affect the cable thermal stability significantly.

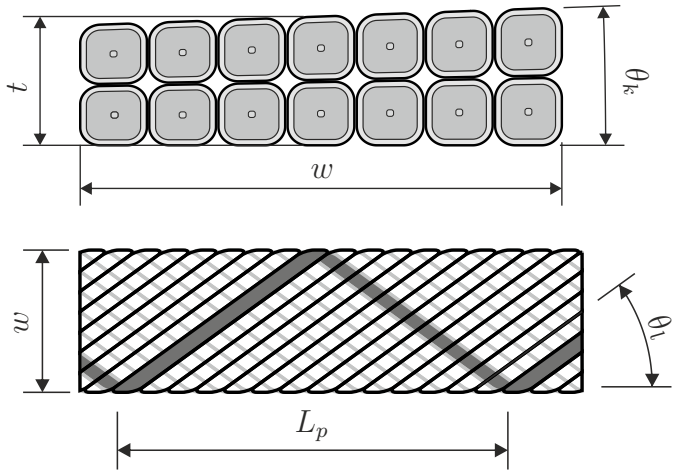

Figure 2.1: Schematic view of the cable, the top figure shows a cross section and the bottom picture shows a top view.

2.1.2 Cable

The geometrical properties of a Rutherford cable are summarized in figure 2.1. The width w of the cable depends on the number of strands and on the compaction factor. As a rough first estimate, w is approximately half the number of strands in the cable times the wire diameter. t is defined as the average thickness of a cable. Typically, it is approximately 1.8 times the wire diameter d. Both w and t depend on the required grade of compaction in the cable design. A keystoned cable will have a thin and a thick edge. The keystone angle θ_k is the angle comprised between the two broad sides of the cable. This angle helps to bring the winding pack into a cylindrical shape around the bore of a dipole or quadrupole magnet (see also figure 1.7).

The transposition pitch L_p is the periodic length in which all the strands return to the same position in the cable cross section. Shorter transposition pitches cause a reduction of ramp losses and provide mechanical stability to the cable during winding of the coil. However, too short transposition pitches can introduce cabling degradation, so

there is a trade-off between ramp losses and mechanical stability on one side and current carrying performance on the other. Therefore, the optimal L_p value is determined by the resilience of the strand against deformation.

The lay angle θ_l is the angle between the axial directions of the strand and the cable. It can be estimated by:

$$\theta_l = \arctan\left(\frac{2w}{L_p - L_{tr}}\right) \approx \arctan\left(\frac{2w}{L_p - 2d}\right) \quad [^\circ]. \tag{2.4}$$

The only unknown is L_{tr}, the length over which the wire travels on the side of the cable where it bends around the edge from one broad side face to the other. This length can be measured easily on the actual cable and it is approximately twice the wire diameter. The precise value also depends on the wire tension during the cabling.

The compaction factor f_C specifies the conductor volume fraction in the "bounding box" of the cable. Obviously a 100% compaction can not be achieved without severely damaging the wires. A value of 78.5% (i.e. $\pi/4$) corresponds to a loose packing, with strands just touching each other without deformation, and not only leaves the wires unsupported but also unnecessary reduces the engineering current density. The optimum value for f_C is typically in between 80% and 95%, depending on the malleability and resulting I_c-degradation in the strand and the desired cable geometry. Note that, f_C is also a relevant property for magnet design since it scales linearly with the engineering current density in the magnet.

$$f_C = \frac{N_{str}\pi(d/2)^2(1/\cos\theta_l)}{t \cdot w} \quad [-]. \tag{2.5}$$

The compaction factor can be calculated with equation 2.5, where N_{str} is the number of strands in the cable. The numerator gives the total area of the strands in the cross section corrected for the ellipticity due to the lay angle. The denominator equates to the surface area of the bounding box around the cable. Since the cable has a trapezoid shape, no corrections for the keystone angle are necessary.

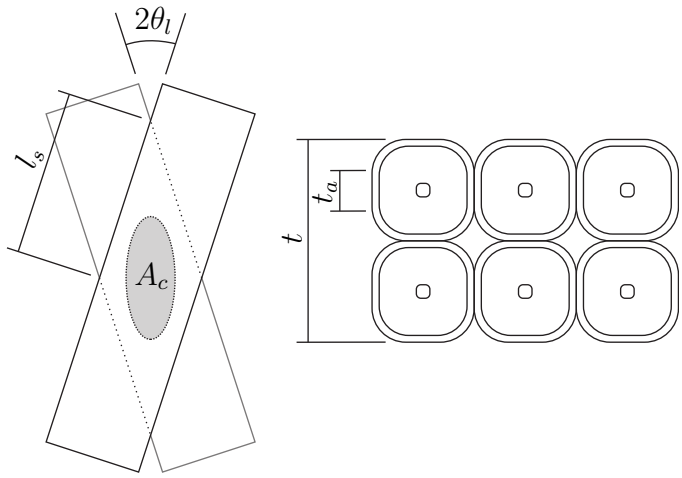

Figure 2.2: Schematic view of the cross- and adjacent-contacts and their relevant dimensions.

Inter-strand contacts

When thermal stability is considered, the most relevant parameters emanating from the geometry are the inter-strand contact areas. These determine the ease of current and heat redistribution among strands.

A schematic representation and naming convention of inter-strand contacts can be found in figure 2.2. The cross contacts are the contacts formed between the two layers of strands in the cable. These are discrete contacts, present at regular intervals along the strands. In numerical calculations, as discussed in chapter 3, the length between two of these contacts is often chosen as the length of one simulation section, l_s. The size of the cross contact area, A_c, depends on the compaction factor of the cable.

The adjacent contact is continuous along the wire. The contact surface has a height t_a, which has a value between zero and half of the cable thickness t. For numerical purposes the adjacent contact area can also be expressed as the area per section length: $A_a = l_s \cdot t_a$.

Model calculations of thermal stability require as input only the

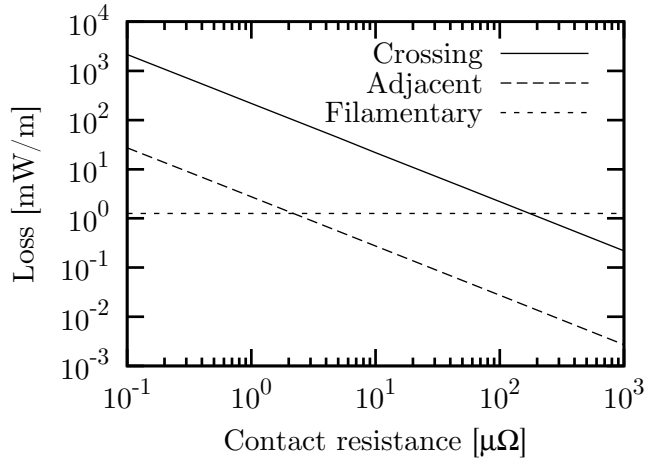

Figure 2.3: Calculated ramp loss in mW per meter conductor in a 40 strands Rutherford cable as a function of the adjacent and crossing contact resistances. For comparison also the inter-filamentary coupling loss is indicated. The loss is calculated per meter of cable for an applied magnetic field perpendicular to the broad side of the cable, at a ramp rate of 0.015 T/s.

contact resistances and the thermal conductances. The contact resistances can be measured directly as is shown in section 5.3. The contact area may be used to estimate the thermal conductance, multiplying it by an estimated heat transfer function. The transfer function depends on the model.

Ramp loss and contact resistances

An accelerator magnet can ramp up with several tesla per minute and the associated dB/dt results in coupling currents in the cables that make up the coil. There are inter-filament coupling currents, inter-strand coupling currents and boundary induced currents [16]. The different types of coupling currents create two unwanted effects; thermal load and magnetic field errors. The thermal load causes temperature rises and additional strain on the cryogenics systems. It

results from the coupling currents that flow through normal conducting boundary layers and the superconductors. The coupling currents also distort the current distribution over the cross section of the cable. Since the magnets are designed with the assumption of a uniform current distribution over the cable cross section, any additional currents introduce magnetic field errors.

The heat load of the ramp losses due to induced currents can be calculated using CUDI, see section 3.1. The result is shown in figure 2.3, where the loss components due to different coupling current paths are indicated. The cross contacts are responsible for the largest losses, since they create the largest pick-up loops. The adjacent contacts create roughly a factor 100 times less loss for the same contact resistance. To limit inter-strand coupling loss to the same order of magnitude as the inter-filamentary coupling loss, the adjacent contact resistance needs to be larger than 2 µΩ (per simulation cell, i.e. per l_s) and the cross contact resistance larger than 200 µΩ.

The contact resistances thus require a minimum value defined by the cooling capacity and required magnetic field quality. If a cable is reacted without core or coating, the contact resistances are often too low for accelerator magnets [18]. During the heat treatment of the cables the copper strands sinter together, resulting in contact resistances well below 1 µΩ. Especially R_c should be kept well-controlled, since it tends to fall below the required value, whereas R_a is commonly found to be in the appropriate range.

R_c can be tuned by inserting a resistive core in the cable, which causes a large increase in the cross-contact resistance without changing the adjacent-contact resistance. Most dipole magnets will need a cored conductor to achieve the set design parameters for ramp loss and magnetic field quality. The samples used in this work are cables for quadrupole magnets or experimental cables for dipole magnets, all without core. Thus the effect of a cored conductor on stability was not experimentally investigated in this work.

2.2 Material properties

At cryogenic temperatures (i.e. in the relevant range from 1.8 to 20 K) the material properties are much more temperature dependent than at room temperature. To perform an accurate calculation using a numerical model, it is essential to know the temperature dependence of the material properties. The electrical and thermal properties of the relevant materials are discussed in the following paragraphs. Additionally, the way how they are implemented in the models is shown.

2.2.1 Electrical resistivity

Superconducting filaments embedded in a normal conducting matrix can be described as a single conductor with anisotropic resistivity. The Residual Resistance Ratio (RRR) is an important measure for the quality of the matrix material within the wire. It is the ratio between the resistivity of the matrix at room temperature and at its operating temperature. In a normal conductor the resistance will decrease with temperature because the largest contributing factor to the resistance at room temperature is the scattering of conduction electrons by lattice vibrations. Since lattice vibrations are greatly reduced at cryogenic temperatures, so is the resistance. What remains is the scattering of electrons by defects in the crystal lattice, which results in the so-called residual resistivity [59]. Since Nb_3Sn has a critical temperature of approximately 18 K, it is in principle impossible to measure the RRR of the matrix material directly, because the temperature range where the residual resistivity is dominant is not yet reached when the Nb_3Sn becomes superconducting, especially in high quality conductors. Common practice is to determine the Resistance Ratio (RR) at a fixed temperature just above the transition point [60], say 20 K in the case of Nb_3Sn.

Resistivity of copper

The temperature dependence of the resistivity of copper is approximated by equation 2.6 [61], which is valid over a large temperature range from 1- to 500 K:

$$\rho_{Cu} = \left[\frac{c_0}{RRR} + \frac{1}{\frac{c_1}{T^5} + \frac{c_2}{T^3} + \frac{c_3}{T}}\right] \cdot 10^{-8} + (37 + 0.05 \cdot RRR) \cdot 10^{-12} \cdot B \quad [\Omega\text{m}]. \tag{2.6}$$

This equation gives the resistivity of copper ρ_{Cu} as a function of temperature, magnetic field and RRR value. c_1 to c_3 are fitting parameters. The first line in the equation defines the temperature dependence and the second one the magnetic field dependence. Note that the RRR value is present in both lines.

Figure 2.4 shows the copper resistivity plotted as a function of temperature for several values of RRR and magnetic field, using equation 2.6. The RRR of high quality Nb_3Sn conductors can be over 200, but, as discussed in chapter 7, it may also be locally degraded to a value of 10 to 20 due to tin leakage during the diffusion heat treatment. Accelerator magnets designed with these conductors usually have a peak magnetic field of 12 to 18 T. It is interesting to note that up to the critical temperature of Nb_3Sn, the resistivity effectively remains constant. It is therefore a valid assumption to keep the resistivity constant with changing temperature for stability calculations where the temperature remains below 20 kelvin.

Resistivity of normal Nb_3Sn

The electrical resistivity of Nb_3Sn in the normal state is much higher than that of copper. A good overview can be found in [62], where it is shown that the resistivity is typically higher than $1 \cdot 10^{-7}$ Ωm and increases with radiation dose and temperature. Using Ohm's law, above T_c the current densities in both materials can be calculated:

$$J_{Cu} = \frac{J_{con}\rho_{sc}}{\rho_{Cu}f_{Cu} + \rho_{sc}f_{nCu}} \quad [\text{A/m}^2], \tag{2.7}$$

$$J_{sc} = \frac{J_{con}\rho_{Cu}}{\rho_{Cu}f_{Cu} + \rho_{sc}f_{nCu}} \quad [\text{A/m}^2], \tag{2.8}$$

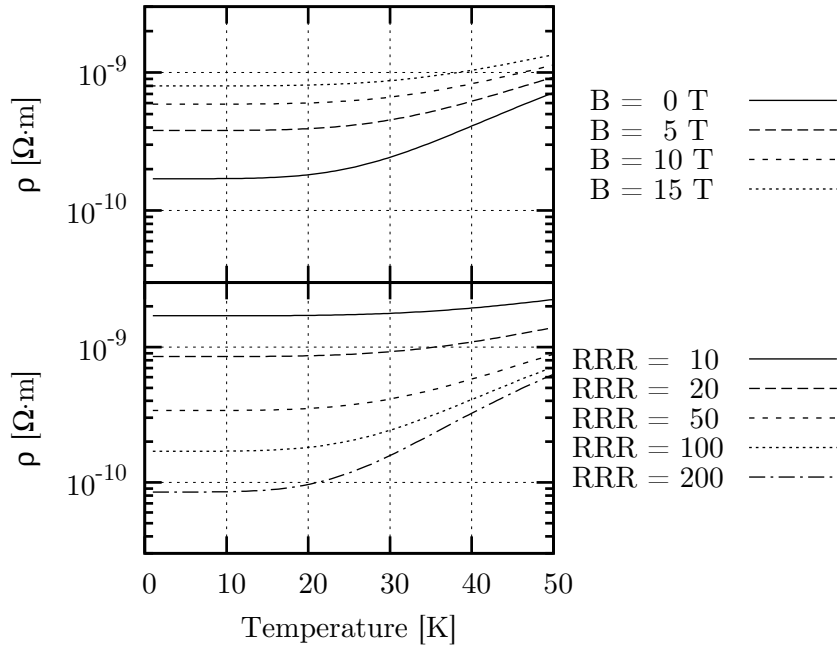

Figure 2.4: Resistivity of copper versus temperature for various values of RRR without applied magnetic field (bottom) and various values of magnetic field with a RRR of 100 (top).

where J_{Cu}, J_{sc} and J_{con} are the current densities in the copper, in the superconductor and overall respectively. The average power dissipated in the conductor is:

$$P = f_{nCu} \cdot \rho_{sc} \cdot J_{sc}^2 + f_{Cu} \cdot \rho_{Cu} \cdot J_{Cu}^2 \quad [\mathrm{W/m^3}]. \tag{2.9}$$

The ratio of dissipated power in the superconductor and copper matrix is:

$$\frac{P_{sc}}{P_{Cu}} = \frac{f_{nCu} \cdot \rho_{sc} \cdot J_{sc}^2}{f_{Cu} \cdot \rho_{Cu} \cdot J_{Cu}^2} = \frac{f_{nCu} \cdot \rho_{Cu}}{f_{Cu} \cdot \rho_{sc}} \quad [-]. \tag{2.10}$$

The conductors considered in this work have ab f_{Cu} value only slightly larger than f_{nCu}, which means that the power ratio is determined

mostly by the resistivity of the two materials. If the RRR of the copper is higher than 20, the total contribution of the Nb_3Sn to the joule heating is less than 1% and may thus be considered negligible.

Scaling law for superconducting Nb_3Sn

The amount of supercurrent that a strand can carry is calculated by multiplying the wire cross section with f_{nCu} and the critical current density J_c. The critical current density may in turn be calculated using a scaling law. Here the expression proposed in [63] will be used, where critical current density as a function of magnetic field, temperature and strain is as follows:

$$J_c(B,T,\epsilon) = \frac{C}{B} s(\epsilon)(1-t^{1.52})(1-t^2)b^p(1-b)^q. \quad [\mathrm{A/m^2}] \tag{2.11}$$

C is a scaling constant, p and q describe the pinning force. $s(\epsilon)$ is a function factoring the strain, b is the reduced magnetic field and t is the reduced temperature, which are defined as:

$$b = B/B^*_{c2}(T,\epsilon), \text{ with } B^*_{c2}(T,\epsilon) = B^*_{c20}s(\epsilon)(1-t^{1.52}), \tag{2.12}$$

$$t = T/T^*_c(0,\epsilon), \quad \text{with } T^*_c(0,\epsilon) = T^*_{c0}s(\epsilon)^{\frac{1}{3}}, \tag{2.13}$$

$$s(\epsilon) = \frac{C_{a1}\left[\sqrt{\epsilon_s^2+\epsilon_{0,a}^2} - \sqrt{(\epsilon-\epsilon_s)^2+\epsilon_{0,a}^2}\right] - C_{a2}\epsilon}{1-C_{a1}\epsilon_{0,a}} + 1, \tag{2.14}$$

$$\text{with } \epsilon_s = \frac{C_{a2}\epsilon_{0,a}}{\sqrt{C_{a1}^2+C_{a2}^2}}. \tag{2.15}$$

Here $B^*_{c2}(T,\epsilon)$ is the critical magnetic field at a given temperature T and strain ϵ, and $T^*_c(0,\epsilon)$ is the critical temperature at a given strain and zero magnetic field. T^*_{c0} is a fitting parameter representing the critical temperature at zero magnetic field and strain. Analogous to this, B^*_{c20} is the fitting parameter representing the critical magnetic field at zero temperature and strain. The superscript star or * indicate that the parameters are effective values, as defined in reference [63]. These are not the values expected in pure Nb_3Sn, but effective

values due to inhomogeneities in the superconducting material in a practical superconductor. C_{a1}, C_{a2} and $\epsilon_{0,a}$ are fitting parameters for the strain sensitivity of the critical surface.

For thermal stability calculations some fitting parameters are irrelevant. It is assumed that the strain state of the conductor is constant. When the scaling law is used to fit a cable measurement the $s(\epsilon)$ is therefore assumed to be equal to one. The fitting parameters for the strain are therefore not relevant for thermal stability.

With the exclusion of the strain sensitivity, there are still five parameters that need to be accurately determined. In reference [63] p and q are assumed to have fixed values of 0.5 and 2.0 respectively. However, reference [64] has shown that it is necessary to leave the fitting parameters for the pinning force free to obtain a more accurate fit at both high and low fractions of the B_{c2}. For the measurements where the critical current is measured over a large magnetic field range and when it is needed to obtain an accurate fit, values of p and q are fitted. Otherwise the fixed values are used. This leaves three free parameters and two conditionally free parameters. The free parameters are varied so that the scaling law fits the measurement with the least squares difference. The value of C is fitted for each sample. If multiple temperature measurements are available the T_{c0} is fitted, otherwise a value of 18 K is used. B_{c20} is fitted for each sample. If the fit deviates more than 1% from the measurement, the values of p and q are adjusted as well, otherwise the default values of 0.5 and 2.0 are used.

Resistivity of a wire

The resistivity change during the transition from superconductor to normal conductor is steep and in order to model this transition correctly, a lot of time steps are needed. By assuming that the current can transfer instantly from the superconductor to the normal matrix the current can be modeled to flow in two parallel circuits, one for supercurrent and one for normal current. To implement this, the equivalent resistivity of the conductor is calculated following:

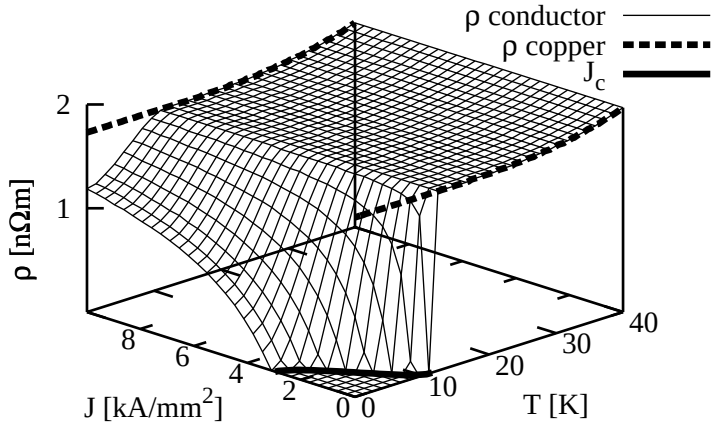

Figure 2.5: Resistivity of the Nb_3Sn strand material as a function of temperature and current density in an applied field of 12 T and with a RRR of 100. The dashed line indicates the pure copper resistivity and the black line shows the J_c (T) curve of the superconductor.

$$\rho_{eq} = \rho_{Cu}\frac{J - J_c}{J} \quad [\Omega\text{m}]. \tag{2.16}$$

This results in the smooth resistivity function shown in figure 2.5. Of course, the function needs to be clipped so that negative values are suppressed. Since calculations using zero resistivity run into numerical difficulty, a minimum is set at a value of 10^{-14} Ωm. This is several orders of magnitude lower than normal values for copper and reduces joule heating to a negligible level.

2.2.2 Thermal conductivity

The cables considered in this work consist mainly of copper and Nb_3Sn and are insulated by impregnated glass insulation. In addition, bronze and thermal barriers like Nb and Ta are present in small fractions. At 4.3 kelvin the heat conductivity of copper [65], Nb_3Sn [66] and glass fiber reinforced epoxy [65] are 680, 0.04 and

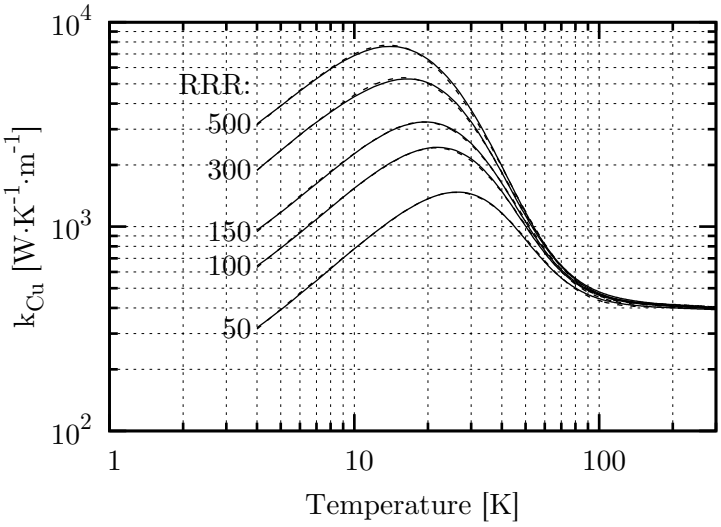

Figure 2.6: Thermal conductivity of copper versus temperature. Continuous lines are results from [65] for different RRR. The long and short dashed lines represent equations 2.17 and 2.18 respectively with a RRR of 100.

0.07 W·m^{-1}·K^{-1} respectively. The large difference between the copper value and the two others is due to the fact that at 4 K the thermal conductivity is dominated by free electrons. Since the glass fiber reinforced epoxy does not have any conduction electrons, it has a comparatively poor heat conductivity. Since the thermal conductivity is thus dominated (by several orders of magnitude) by the copper, the thermal conductivity of the other materials may be neglected.

As shown in figure 2.6, the temperature dependence of the thermal conductivity has a peak between 13 and 26 K, depending on the purity of the material. For low-RRR copper the peak falls around the transition point of Nb_3Sn.

To calculate the heat conductivity of the copper, the Wiedemann-

Franz law may be used:

$$k_{Cu}(T, RRR, B) = \frac{L_0 T}{\rho_{Cu}(T, RRR, B)} \quad [\mathrm{W \cdot m^{-1} \cdot K^{-1}}], \qquad (2.17)$$

where k_{Cu} is the heat conductivity of copper and L_0 is the Lorentz number ($2.44{\cdot}10^{-8}$ $\mathrm{W{\cdot}\Omega{\cdot}K^2}$). The Wiedemann-Franz law breaks down when k_{Cu} approaches its maximum, as can be seen in figure 2.6. This implies that for simulations with a large enthalpy margin the thermal conductivity is overestimated, but for temperatures below 10 K the Wiedemann-Franz law holds. It is even a good approximation for poor quality conductors with a relatively low RRR (<50) up to 20 K, well above the transition point of Nb_3Sn.

In [67] an empirical fit of thermal conductivity with temperature is proposed, which matches the data from [65] within 2% from 1 K to 100 K for all values of RRR:

$$k_{Cu}(T, RRR) = \frac{1}{W_0 + W_i + W_{i0}} \quad [\mathrm{W \cdot m^{-1} \cdot K^{-1}}]. \qquad (2.18)$$

The definition of the parameters W_0, W_i and W_{i0} can be found in appendix A. This relation does not take into account the effect of magnetic field on thermal conductivity, which is not negligible [68]. To take the effect of magneto-resistivity into account, equations 2.18 and 2.6 can be combined:

$$k_{Cu}(T, RRR, B) = k_{Cu}(T, RRR)\frac{\rho_{Cu}(T, RRR, 0)}{\rho_{Cu}(T, RRR, B)}. \qquad (2.19)$$

This equation fits the known data accurately and takes into account the effect of the applied magnetic field. It can be used outside the effective range of the Wiedemann-Franz law.

2.2.3 Volumetric heat capacity

Most often the specific heat at constant pressure C_p is used when the heat capacity of any material is measured, because it is simpler and faster to get an accurate mass measurement than an accurate volume

measurement. However, because of the nature of the calculations, the more practical choice is the volumetric heat capacity C_v. The size of all model elements as well as the mass density are known at room temperature. Since specific heat is reported in literature, the material densities are needed to calculate the volumetric heat capacity. The value for pure copper is used, $8.96{\cdot}10^3$ kg/m^3. The non-copper part of the strand is assumed to consist solely of Nb_3Sn. In theory its density is $8.91{\cdot}10^3$ kg/m^3, however, due to porosity and vacancies in the lattice this is never achieved. The measured density of bulk Nb_3Sn falls between $8.76{\cdot}10^3$ kg/m^3 and $8.82{\cdot}10^3$ kg/m^3 [69], [70]. In this work $8.80{\cdot}10^3$ kg/m^3 is used.

The f_{nCu} can contain small fractions of other materials, but their volume is such that their contribution to the C_v of the conductor is neglected. Note however, that even though its volume fraction is typically small, unreacted residual Nb in the Nb_3Sn section can have a large effect on C_v when it is in the superconducting state. Fortunately, the B_{c2} of niobium is so low (0.4 T) that any appreciable transport current and corresponding self-field will bring it to the normal state.

In figure 2.7 the heat capacity of all relevant materials are shown as function of temperature. The data are taken from the reported values in references [65], [71]–[73]. Unlike normal materials, the heat capacity of superconductors depends heavily on the applied magnetic field. In reference [73] it is found that at 1.9 K C_v is a factor 8 larger at 16 T than at 0 T. For normal metals at low temperature, it is found [74] that the heat capacity follows:

$$C_v(T) = AT + BT^3 \quad [\mathrm{J \cdot K^{-1} \cdot m^{-3}}], \tag{2.20}$$

where A and B are material-specific constants. The linear part of equation 2.20 is the specific heat contribution of the free electrons in the conductor and the cubic term stems from the contribution of the lattice vibrations in the crystal. According to reference [39], equation 2.20 holds for materials in the temperature range relevant for this study.

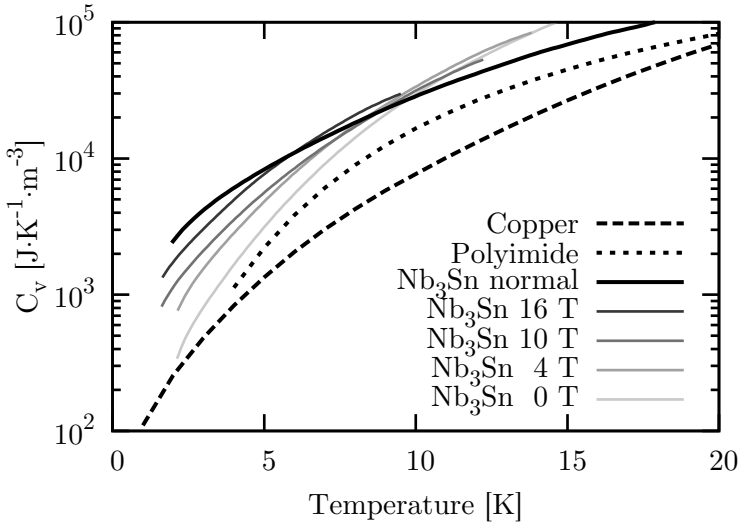

Figure 2.7: The volumetric heat capacity versus temperature of various materials used in accelerator magnets. The thin lines are superconducting Nb_3Sn at various magnetic fields and the thicker lines are for other materials.

The magnetic field dependency of C_v for superconductors results from the coupling of the electrons via the crystal lattice. At low temperature the heat capacity in normal conductors is dominated by the contribution of the free electrons. Because the free electrons in superconductors are bound in Cooper pairs, the heat capacity deviates strongly from the behavior of normal conductors. Furthermore, since the density of states of the Cooper pairs depends on the applied magnetic field, so does the heat capacity.

To calculate the C_v value of Nb_3Sn for any temperature or magnetic field, the measured values from reference [72] and [73] are fitted to equation 2.20 at each magnetic field level. As shown in reference [36], this equation can be used to determine $C_v(T)$ for an arbitrary magnetic field by taking the weighted average of the two closest magnetic field values, see equation B.4. The values of the fitting pa-

rameters are discussed in appendix B.

2.3 Cable samples

For notational simplicity the samples are labeled with a letter. Table 2.1 presents an overview of their properties. The samples are obtained from two different programs, which are discussed in section 1.3.3. The first is the short model coil (SMC) program at CERN, which is set up to gain experience with the construction and operation of Nb_3Sn dipole magnets. These "model" cables have the same properties as the envisaged full-size cables, but are prepared with a reduced number of strands. The cable width and transposition pitch are scaled to maintain the same compaction and lay angle as in the full-size cable design. The strands have a diameter of 1.25 mm and are produced with the PIT process. Sample H is a full-size version, designed to be used in the DS magnet [75].

Sample E to G originate from the US-based LARP program. These cables are used in quadrupole magnets. The wires are RRP-type and have a diameter of 0.7 mm.

The numbering of the cables is done chronologically in both the CERN (SMC) and LBNL (LARP) laboratories. It is the cabling run number given by the cabling institute, which in this thesis is prefixed with an SMC- or LARP- to avoid confusion. The cable names have no relation to any magnets wherein the cables are used. Several of the cables from the SMC program result from cabling tests and were never intended for use in a magnet. Note from the numbers that the first two samples are the very first Nb_3Sn cables to be cabled at CERN.

Table 2.1 contains a summary of the cable sample properties. The column labeled "Wires" gives the number of strands that make up the cable, "Process" indicates the method used to produce the Nb_3Sn strands and "Diam." is the diameter of the strands before cabling. The "(Sub)elements" column gives the number of filaments

Table 2.1: List of cable properties.

# (-)	Name (-)	Wires (#)	Process (-)	Diam. (mm)	(sub)elements (#)	Fil. Diam. (µm)	w × t (mm)
A	SMC001	14	PIT	1.25	288	50	9.7 × 2.2
B	SMC003	14	PIT	1.25	288	50	9.9 × 2.2
C	SMC039	14	PIT	1.25	288	50	10.0 × 2.2
D	SMC042	14	PIT	1.25	288	50	10.0 × 2.2
E	LARP982	27	RRP	0.70	108/127	40	10.0 × 1.25
F	LARP983	27	RRP	0.70	54/61	80	10.0 × 1.25
G	LARP1013	27	RRP	0.70	108/127	40	10.0 × 1.25
H	DS	40	RRP	0.70	108/127	40	21.2 × 1.25

# (-)	θ_k (°)	L_p (mm)	f_C (%)	f_{CnC} (-)	θ_l (°)	A_{eff} (%)	RRR_{str} (-)	RRR_{Cab} (-)	I_c (A)	J_c (A/mm^2)	J_e (A/mm^2)
A	0	80	80	1.19	13	38	66-68	58-61	1320	2356	866
B	0	150	79	1.19	7	36			1326	2366	852
C	0	60	82	1.00	18	41	36-39	73-82	1272	2073	809
D	0	60	82	1.10	18	39	208-227		1042	1783	663
E	1	77	85	1.18	15	39		276-279	406	2300	877
F	1	77	85	0.87	15	46	282-293	378-356	446	2167	963
G	1	80	85	1.13	14	40			482	2668	1041
H	1	150	85	1.13	14	40	48-81		482	2668	1041

in the PIT strands, or the number of sub-elements in the case of RRP, while the "Fil. Diam." column gives an estimate of the filament size in the undeformed strand. The column "$w \times t$" gives the width and the average thickness of the cable.

The second part of the table starts again with the sample label and is followed by the typical cable parameters: keystone angle θ_k , transposition pitch L_p, compaction factor f_C, copper to non-copper ratio f_{CnC} and the lay angle θ_l. Next the effective cross-sectional area A_{eff} is given, which is the percentage of the cable cross section that is non-copper.

The next two columns give the RRR values found in extracted strand measurements, RRR_{str} and cable measurements RRR_{Cab} . The numbers indicate the highest and lowest values found. The number of measurement for the wire ranges from 3 to 5, while the cable measurements are performed on each leg of the FRESCA sample.

The final three columns give the strand critical current I_c and its density J_c at a magnetic field of 12 tesla and a temperature of 4.3 kelvin, as well as the calculated engineering current density J_e at this working point.

2.3.1 Full-size sample

The odd cable out is sample H, a full-size Nb_3Sn Rutherford cable sample tested on the U-shaped sample holder, as described in section 5.2. This sample is a valuable addition to the sample list, since it presents an opportunity to study the thermal stability of a cable as used in dipole magnets and thus to gauge whether the data on downsized cables are representative for the expected performance. Its cross-sectional aspect ratio differs by nearly a factor two from the other samples and the total available enthalpy margin is much higher than of the sub-size cables.

Sample history

Sample H was in first instance prepared to determine the relation between transversal stress σ and the critical current. Since this is in

principle a destructive test, the sample history is discussed here to demonstrate that the data may still be expected to be representative of a typical cable sample.

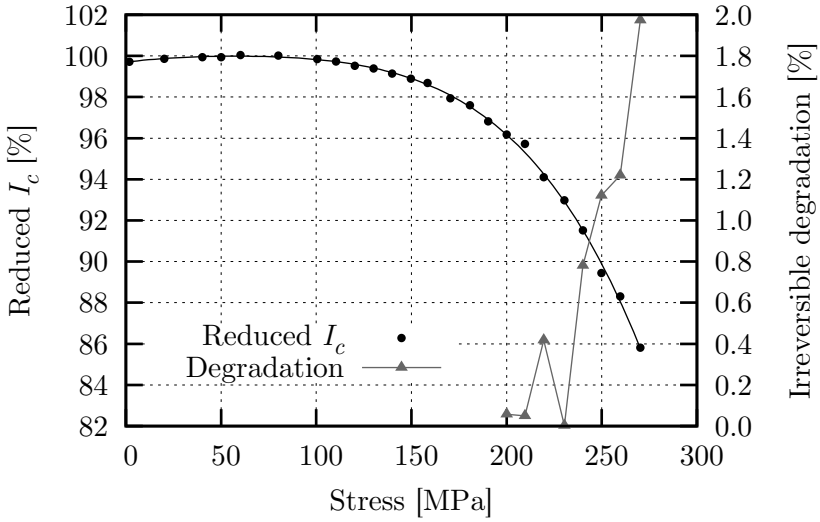

Figure 2.8: The reduced I_c value as a function of the transverse stress σ measured on sample H (black dots). The data are fitted with a fourth order polynomial function (black line). From 200 MPa onwards the critical current is cycled back down to 50 MPa for each point, in order to determine the irreversible I_c degradation (gray triangles).

The $I_c(\sigma)$ measurements are summarized in figure 2.8. The transverse stress is increased in increments of 10 MPa from 100 MPa onwards. The I_c under loaded condition is normalized with its maximal value, resulting in a reduced I_c. A shallow peak in I_c is found around 50 MPa. From 200 MPa onwards, the I_c value is remeasured at 50 MPa transverse stress after each increment. The percentage of I_c degradation at this reference stress level is defined as irreversible degradation. At 220 MPa, the sample shows the first indication of irreversible degradation.

After the data in figure 2.8 were collected, the sample was warmed

up to room temperature and fitted with the instrumentation for stability measurements. Once cooled down again, it was found that the sample had not only recovered the irreversible degradation from the previous $I_c(\sigma)$ tests, but even gained an additional 0.5% in critical current over the starting value at the previous cool down. Presumably this is a result of the second thermal cycle. This shows that the manipulations needed to install the point heaters did not significantly degrade the sample. In contrast to the $I_c(B)$ and $I_c(\sigma)$ measurement series, the sample did become less stable close to the critical surface and many quenches were needed to arrive at the critical current. The sample quenched several times at stationary current as well.

2.4 Conclusion

The topography of Rutherford cables can be modeled using their periodic and predictable shape. The relevant dimensions have been defined and illustrated.

The relevant material properties determining stability are both temperature and magnetic field dependent. Their dependence on temperature and magnetic field can be expressed with the analytical functions presented.

The samples used in this work are presented, both cabling parameters and known material properties are summarized.

Chapter 3

Thermal stability simulations

Three models that describe the thermal stability of Rutherford cables are evaluated, firstly a resistor network type model called CUDI, secondly a straight finite difference model called StabCalc, and finally an analytical description. A schematic illustration is given in figure 3.1.

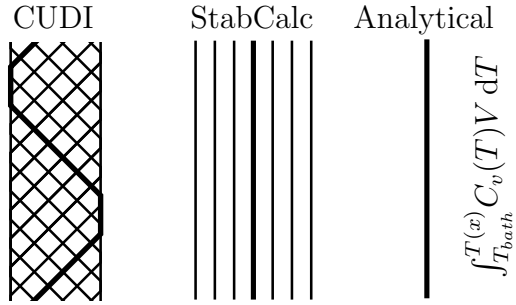

Figure 3.1: Visual summary of the three models, from left to right, CUDI, StabCalc and analytical.

CUDI is a well-developed code that is freely available for research purposes. It solves thermal and electrical flows in Rutherford cables

by simulating them as a resistor network, taking into account inductance and magnetization effects. This enables the model to evaluate time-dependent phenomena, like thermal stability or AC-loss during a magnet ramp. CUDI has one drawback when used for thermal stability calculations in high-J_c superconductors. The spatial resolution of the simulation is fixed by the geometry of the cable and may be too coarse. The length of the discretized sections used in the simulations is approximately 2 mm, conforming to l_s as described in section 2.1.2. As shown in section 3.3.1, the MPZ in the cables studied in this work is typically 2 mm, which means that the cable will quench already when one single model section is normal.

To study normal zones with a resolution down to the size of the wire diameter, the new model StabCalc was developed. By ignoring the 3D cable structure and assuming that the cable can be simulated as single strands, the model is not limited by the relation between geometry and spatial resolution. A second aim of this model is to produce accurate MQE curves with minimal input.

Lastly, an analytical approximation is used to gauge how precise a non-numerical approach can be. As discussed in section 1.4.3, analytical estimates of stability may readily be made for single strands without helium cooling.

3.1 CUDI

CUDI is the most complex and well-developed model that can simulate Rutherford cables. It was originally developed to study the behavior of Nb-Ti cables for the LHC in 1993 [41]. The model has gradually been extended over the years to include additional thermal and electrical properties of superconducting cables in accelerator magnets and is now a publicly available free software package. It has been validated extensively [49] for the thermal stability modeling of Nb-Ti cables. A short description of the model and the relevant user input is presented here. The details about the thermal and electrical

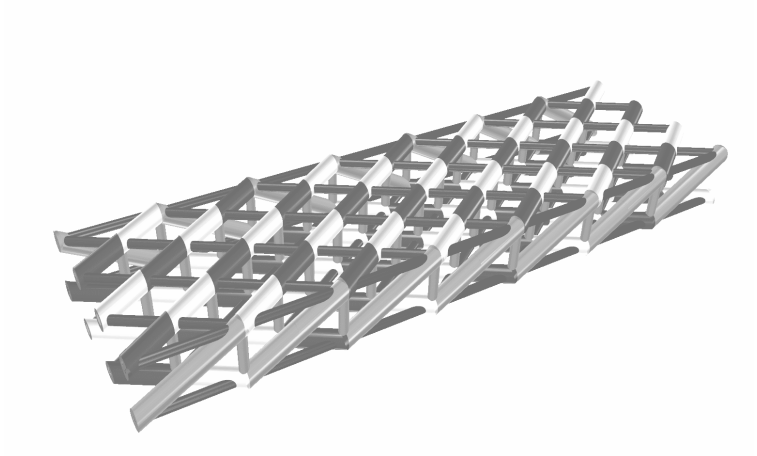

Figure 3.2: Schematic view of the resistor-inductance network used in CUDI. The thick cylinders are the sections in the strand, the black and white colors indicate how the sections are distributed. The thinner black rods denote the adjacent connections, while the gray ones represent the crossing connections.

solving techniques are described comprehensively in the manual [61].

CUDI is a resistor-inductance network model that can simulate the cable as a 3D structure of 1D strands, coupled at regular intervals depending on the cable geometry, see figure 3.2. This means that the spatial resolution of the model is fixed and cannot be changed freely. The strands are divided in so-called sections (the thicker cylinders in figure 3.2). The section lengths l_s are determined by the distance between successive crossing contacts in the cable as explained in section 2.1.2. The crossing contacts are the gray rods between the two layers of strands, the black rods represent the adjacent contacts. Note that the adjacent contacts lie parallel to the strands underneath. If one section becomes normal and the current is shared with the two neighboring strands, the sharing will occur through the adjacent and crossing contacts.

The properties of the model sections are calculated using the pa-

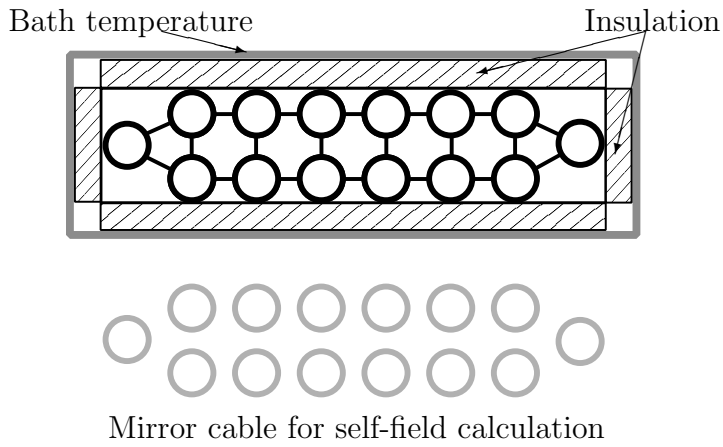

Figure 3.3: Schematic drawing of the boundary conditions used in the CUDI model.

rameters that were introduced in section 2.2 as input. These are used to calculate the electrical and thermal conductivities of all the elements in the model.

The boundary conditions at the start and end of the simulated cable section are constant current and fixed temperature. This means that if a propagating normal zone approaches one of the ends of the simulated cable section, the results are affected by the presence of an unrealistic infinite heat sink. It is therefore required that the simulated cable section is always much longer than the expected minimum propagation zone. This has to be taken into account when a simulation is repeated for various conditions, and the operational parameters move further away from the critical surface so that the MPZ starts to increase.

The lateral boundary conditions of the cable are depicted in figure 3.3. The thermal boundary is an infinite heat sink at bath temperature separated by a layer of material modeled as a relatively high thermal resistance with zero heat capacity. This insulation can be

varied at the short edges, but the same conductivity is used for the broad sides. As will be explained in section 4.2, heat cannot easily be removed from the cable over the broad faces. These are used as support surfaces and thermal flow is obstructed by materials with a poor thermal conductivity. A thermal resistance corresponding to the thermal conductivity of a 2 mm thick layer of polyimide is used as insulation. The short faces, however, are exposed directly to the helium bath and here the thickness of the electrical insulation and its estimated thermal conductivity are given as input parameters.

The magnetic boundary condition consists of 2 parts. Firstly, the external magnetic field, which can be applied in any direction. Secondly, the self-field created by the simulated cable and its return lead is determined. It is assumed that the return lead carries the same current as the cable sample. The external and self-field are added to obtain the total magnetic field distribution over the cable sample.

The values of the coupling constants for current and heat conductions between model sections may be freely chosen in CUDI. For the electrical resistance, measured mean values are used. As discussed in section 2.1.2, for the cables analyzed here, the adjacent contacts have a more than a hundred times lower resistance than the crossing connections. This implies that the two layers of strands in the cable are practically decoupled. This fact is used as the basis for a new model called StabCalc, which is presented in the next section.

3.2 StabCalc

StabCalc features a simplified geometry for which the governing equations are solved. The simplifications reduce the numerical load significantly. StabCalc assumes that the thermal stability of a Rutherford cable can be modeled by considering it as a collection of straight parallel wires. This assumption is based on the knowledge that the system is adiabatic and that the current densities are high. Current

redistribution takes place locally, so that the geometry of the cable is assumed to be irrelevant. The model is solved with the Finite Difference Method (FDM), meaning that the governing partial differential equation is solved by rewriting it as a normal differential equation which applies to a finite element and then solving this equation in all the elements spanning the model. The thermal part of the model is solved using the heat equation [76]:

$$\frac{\partial T}{\partial t} - \frac{\boldsymbol{k}(T)}{C_v(T)}\nabla^2 T - \frac{q(T, \boldsymbol{I})}{C_v(T)} = 0. \tag{3.1}$$

T and t are temperature and time, k and C_v the temperature-dependent heat conductivity and specific heat, and q the temperature- and current-dependent heat generation. The required material properties are the same as in CUDI and are described in section 2.2.

The quasi-static approximation of Maxwell's equations [77] is used to solve the evolution of current in the cable. This approximation yields the following expression for the magnetic field in a body carrying current:

$$\frac{\partial \boldsymbol{B}}{\partial t} - \nabla \times \left(\frac{\boldsymbol{\rho}(\boldsymbol{I}, T)}{\mu_0} \nabla \times \boldsymbol{B} \right) = 0. \tag{3.2}$$

The magnetic field $\boldsymbol{B}$ is generated by the current $\boldsymbol{I}$ in the body, whose relaxation is governed by the distribution of the current- and temperature-dependent resistivity $\boldsymbol{\rho}$. The derivation can be found in appendix C. The equation is transient and thus takes inductive effects into account. The "quasi-static" part in its name reflects the fact that it does not take into account any electromagnetic waves. This simplification is appropriate as long as the magnetic field changes are slow enough for RF-loss to remain negligible compared to joule heating and AC-loss, which is the case for even the fastest ramping Nb_3Sn magnet. The equation is difficult to solve in the general 3D case since the necessary boundary conditions require a large area around the conducting body to be modeled. However, for a 2D situation such as StabCalc, the boundary conditions are compact. Rewritten

to model a current in a 2D plane, equation 3.2 takes the following form:

$$\frac{\partial B_z}{\partial t} = \frac{1}{\mu_0}\left(\rho_x \frac{\partial^2 B_z}{\partial y^2} + \frac{\partial \rho_x}{\partial y}\frac{\partial B_z}{\partial y} + \frac{\partial \rho_y}{\partial x}\frac{\partial B_z}{\partial x} + \rho_y \frac{\partial^2 B_z}{\partial x^2}\right). \tag{3.3}$$

The derivation can be found in appendix C. Equation 3.3 assumes that the geometry consists of a conductor that is infinitely long in the z-direction and which also has constant material properties in the z-direction. The current components in the x and y directions can then be calculated. The resistivity term is described as a diagonal tensor. This makes it possible to model an orthotropic resistivity, featuring a low (zero) resistivity in the strand direction (x) and finite resistivity between the strands (y). The current density in the two directions can be calculated using:

$$J_x = \frac{1}{\mu_0}\frac{\partial B_z}{\partial y} \wedge J_y = \frac{1}{\mu_0}\frac{\partial B_z}{\partial x} \quad [\mathrm{A/m^2}]. \tag{3.4}$$

This current density is scaled to a current in the strand cross section to evaluate the output of the model. The implementation of equation 3.3 can be seen in figure 3.4. The exact discretization can be found in appendix C. The modeled volume is assumed to be infinite in the z-direction. The strands are laterally confined in a single calculation cell. The total current in the element is then calculated as J times the surface area of the strand.

It is known that the self-inductance of a round wire is about 15% higher than the one of a square-sectioned wire with the same size [78]. This difference is somewhat alleviated because the strands are compacted in the cable and are no longer round, which is taken into account by reducing the width of the simulated wires. For a cable with a fill factor of 78.5% (touching circular strands), the error in the self-inductance is 15% and for a completely compacted cable the error would be 0%. Because of the irregular shape of the compacted strands, their exact inductance is hard to estimate.

Concerning the mutual inductance, reference [78] shows that there is a negligible difference between squares and wires. In conclusion,

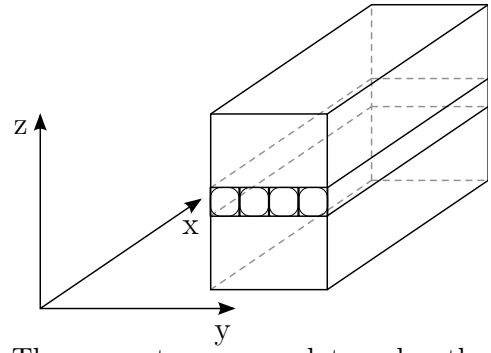

Figure 3.4: The geometry assumed to solve the 2D-quasi static Maxwell's equation in StabCalc. The block extends infinitely in positive and negative z-directions and all properties and parameters are assumed to be constant in this direction.

StabCalc might overestimate induced current redistribution and therefore overestimate the value of MQE slightly for poorly compacted cables.

The size of the 2D calculation cells is chosen such that they are exactly one wire diameter wide and are approximately square. A schematic view is given in figure 3.5. The cell size in the axial direction is a free parameter, but reducing it below the wire diameter does not allow to gain any further physical insight. Any temperature variation on a scale smaller than the wire diameter requires a different kind of model and has to take into account the filament distribution. For thermal stability calculation it is assumed that these effects are irrelevant as the empirically observed energy needed to quench the wire is much higher and directly drives a length equal to several wire diameters into the normal state. On the other hand, when the element length is decreased, more cells are needed to model the same lengths of cable. Since the heat capacity of the cells goes down with their size as well, more time steps are needed to allow the model to converge. In short, decreasing the cell size does not gain any insight and costs a lot more numerical effort.

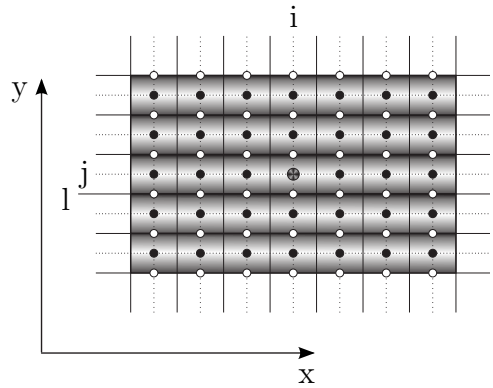

Figure 3.5: The meshing used to solve the FDM. Calculation cells are divided by the solid lines. The dashed lines are the center lines. The black circles indicate the nodes where the temperature is calculated and the white circles the nodes where B_z is calculated.

3.3 Analytical estimates

The highly non-linear material properties of low temperature superconductors make analytical estimates difficult, imprecise or a combination of both. Nevertheless, a calculation method is presented here that is commonly applied in the field of applied superconductivity to furnish first-order estimates of various quantities relevant for thermal stability.

3.3.1 Minimum Propagation Zone

Thermal stability can be described by defining a Minimum Propagation Zone or MPZ. A small section of wire with length l has risen in temperature to the point where all superconductivity is lost. This strand section experiences both internal heat generation by joule heating and cooling by heat conduction to the still cold surroundings. The tipping point between recovery and propagation is reached when the conduction cooling equals the joule heating [9], section 5.2, leading to the following estimation:

$$\frac{2kA(T_c - T_{bath})}{l_{MPZ}} = J_c^2 \rho A l_{MPZ} \Rightarrow \quad [\mathrm{W}], \tag{3.5}$$

$$l_{MPZ} = \sqrt{\frac{2k(T_c - T_{bath})}{J_c^2 \rho}} \quad [\mathrm{m}]. \tag{3.6}$$

The first equation expresses the cooling on the left hand side and the joule heating on the right. The second one represents the resulting expression for l_{MPZ}, the length of the MPZ. Both expressions comprise heat conductivity k, the strand cross-sectional area A, the critical temperature T_c, the bath temperature T_{bath}, the critical current density J_c and the normal state resistivity ρ. The copper to non-copper ratio f_{CnC} is used to scale J_c and ρ to the effective values of the wire and not the values of the superconductor or the stabilizer alone.

Characteristic operating conditions for Nb_3Sn are the pool boiling temperature of helium (4.2 K), applied magnetic field of 12 T and a J_c value of $2.5 \cdot 10^9$ A/m^2. Under these conditions, the thermal conductivity of copper with a RRR of 100 is approximately $k = 700$ W$\cdot$m$^{-1}\cdot$K^{-1} and its resistivity is approximately $\rho = 7 \cdot 10^{-10}$ Ωm. The T_c-value is calculated using the scaling law from section 2.2.1. In figure 3.6 the MPZ length predicted by equation 3.6 is plotted using these characteristic values for Nb_3Sn conductors.

In high-J_c Nb_3Sn conductors there is already significant joule heating occurring before T_c is reached. As soon as the temperature surpasses the current sharing temperature the first joule heating occurs. Joule heating depends quadratically on the normal current density $P = \rho_m J_n^2$. Here P is the joule heating in W/m^3, ρ_m is the resistivity of copper and J_n is the current density in the matrix. J_n is zero when the temperature is lower than T_{cs} and maximal when T exceeds T_c. In between both temperatures, J_n depends on the temperature dependence of the critical current.

According to [79] the average between T_c and T_{cs}, T_{mean} is a better approximation than the values themselves. Following this, equa-

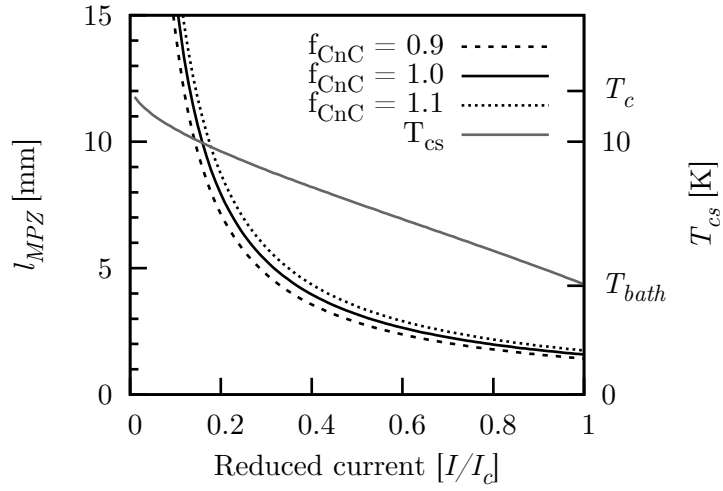

Figure 3.6: Estimate of the MPZ length as a function of reduced current in a representative Nb_3Sn conductor at characteristic operation conditions, calculated using equation 3.6. On the right axis the T_{cs} is plotted with the solid gray line. Several values of f_{CnC} are used to show the band of typical high-J_c wire values for this parameter.

tion 3.6 is rewritten as:

$$l_{MPZ} = \sqrt{\frac{2k(T_{mean} - T_{bath})}{\rho J_n^2}} \quad [\text{m}]. \tag{3.7}$$

The effect on the l_{MPZ} can be seen in figure 3.7. When T_{cs} is used instead, the minimum propagation zone length goes to zero at I_c as expected. When T_c is used the same value as in figure 3.6 is found. Finally, the T_{mean} line falls in between the previous two.

The MQE is estimated by calculating the enthalpy needed to bring a strand section of l_{MPZ} from the bath temperature to the respective final temperature. To this end, the weighed volumetric heat capacities are multiplied with the volume of the minimum propagating zone and integrated from the bath temperature to the T_{mean}.

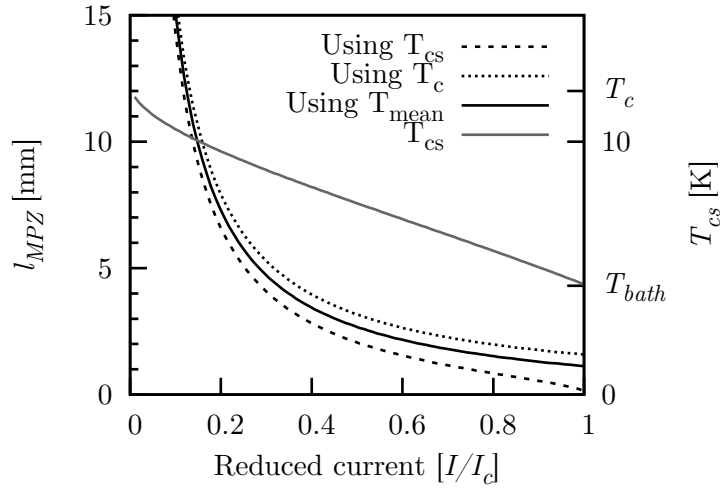

Figure 3.7: Estimate of the MPZ in a Nb_3Sn conductor as a function of reduced current using different variables for T_{mean} in equation 3.7.

The material properties described in the previous chapter are used to determine the heat capacities.

3.3.2 Heat capacity estimate

As discussed in section 3.3, the heat capacity can be fitted with a third order polynomial. Two options have been explored:

$$C_{v1}(T) = C_{cv}T^3 \qquad [\mathrm{J}\cdot\mathrm{K}^{-1}\cdot\mathrm{m}^{-3}], \qquad (3.8)$$

$$C_{v2}(T) = C_{cv1}T + C_{cv2}T^2 + C_{cv3}T^3 \qquad [\mathrm{J}\cdot\mathrm{K}^{-1}\cdot\mathrm{m}^{-3}], \qquad (3.9)$$

where the C_{cv} variables are adjustable parameters used to fit the emperical $C_v(T)$ relation. The zeroth order term is left out since C_v should go to zero at T=0.

Both approximations are plotted together with the values used in the numerical models in figure 3.8. For this example the copper to non-copper ratio f_{CnC} is chosen to be 1. The fits are made by minimizing the root mean square of the residue over a temperature

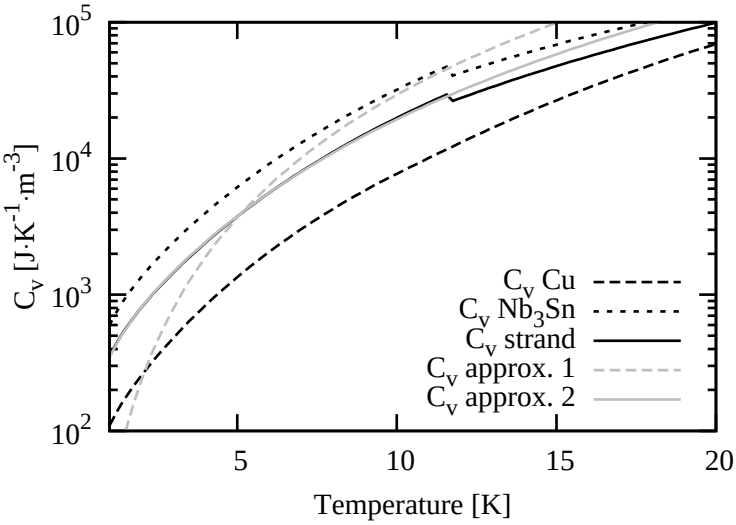

Figure 3.8: The heat capacity as a function of temperature for copper, Nb_3Sn, and for a strand, with the two approximations superimposed in gray.

range from $T = 1$ K to $T = T_c$. This avoids fitting the discontinuity in the C_v at the transition. The first approximation works well at higher temperatures, close to T_c, but at lower temperatures the second approximation is needed to achieve a good enough fit.

3.3.3 Energy estimate

The enthalpy margin can now be estimated with a trivial integration over the temperature rise, multiplied with the MPZ volume:

$$H(T_{mean}) = \int_{T_{bath}}^{T_{mean}} C_v(T) l_{MPZ} A \, \mathrm{d}T \quad [\mathrm{J}], \tag{3.10}$$

where A is the cross-sectional area of the strand. This approximation ignores the temperature profile along the strand and assumes a "block-shaped" temperature rise. The ensuing expressions show a

fourth order temperature dependence:

$$H(T_{mean}) = A \cdot l_{MPZ} \cdot \frac{C_{cv}(T_{mean}^4 - T_{bath}^4)}{4} \quad [\mathrm{J}], \tag{3.11}$$

$$H(T_{mean}) = A \cdot l_{MPZ} \cdot \left[\frac{C_{cv3}(T_{mean}^4 - T_{bath}^4)}{4} + \frac{C_{cv2}(T_{mean}^3 - T_{bath}^3)}{3} + \frac{C_{cv1}(T_{mean}^2 - T_{bath}^2)}{2} \right], \tag{3.12}$$

using equations 3.8 and 3.9 respectively. These expressions still need two numerical calculations, one for T_{cs} and one for T_c. So a purely analytical estimate in the form of a closed $H(B, J, T_{bath})$ expression is not achievable unless the scaling laws on Nb_3Sn are simplified at the cost of accuracy. Due to the relative ease at which these values can be solved numerically, this is left out of the scope of this thesis.

3.4 Conclusion

Three models have been introduced that are capable of predicting the thermal stability of Nb_3Sn Rutherford cables.

The first is CUDI, a full 3D resistor-inductance network model that takes all cable physics into account with high fidelity, but with coarse meshing.

The second is StabCalc, a finite difference model comprising an array of parallel strands with fine meshing, but ignoring the cable geometry and any outside influences aside from the applied magnetic field.

The third is an analytical single strand estimate widely used in the field of applied superconductivity as a first approximation of the thermal stability in conductors.

Chapter 4

Sample preparation for the FRESCA cable test facility

High-J_c Nb_3Sn wires are brittle and sensitive to strain. Sample preparation and instrumentation can therefore have influence on the measurement results. To ensure that the measurements on cable samples truly reflect the performance limits of the cable sample, unaffected by the preparation, careful handling is mandatory to avoid damage by unnecessary strain on the sample. The heat treatment, impregnation, instrumentation and fixation of the sample are described in section 4.1. This is followed in section 4.2 by the method to apply transverse pre-stress to fixate the cable sample. Estimates of the effect of instrumentation and loading on the test results will be given as well.

The cable samples are measured in a test station specially designed for testing superconducting cables for accelerator magnets. The test station is introduced in section 4.3. The range of possible test conditions is specified. The magnetic field in the sample under test conditions is calculated as well. In section 4.4, the methodology of the measurements and the expected errors are described. Furthermore, the data acquisition and processing is explained.

Section 4.5 is devoted to the numerical validation of the measure-

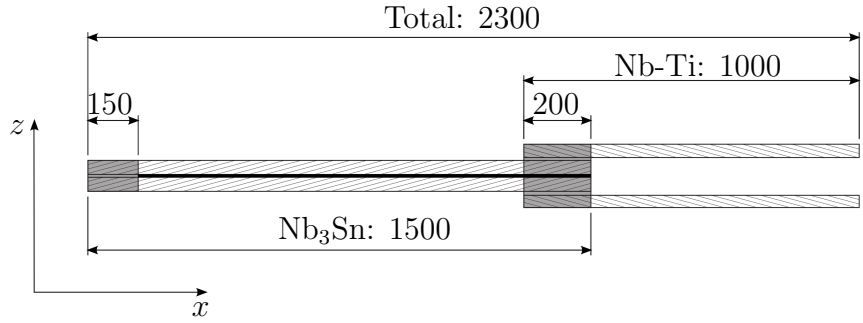

Figure 4.1: Layout sketch of the sample. The Nb_3Sn cable sample (left hand side) is connected to the two current leads by Nb-Ti cables (right hand side) and soldered connections (dark gray). The numbers indicate the dimensions in millimeter.

ments. Aspects that cannot be directly measured, such as heat flow, magnetic field distribution and transversal stress distribution, are numerically calculated in order to quantify their possible influences.

4.1 Sample preparation

The shape of the sample is defined by the FRESCA test station, which will be presented in section 4.3. Here the sample preparation method and the instrumentation which is directly attached to the sample are presented.

4.1.1 Layout

The sample layout is shown in figure 4.1. The sample coordinate system is indicated in the bottom right, $x = 0$ at the tip of the sample holder, y and z axis are parallel to the width and thickness of the sample cables respectively. The x-axis is set at the center line of the sample and therefore the FRESCA magnet bore.

This is a so-called hairpin configuration, by which the current is injected in one of the two Nb-Ti leads, flows down one of the Nb_3Sn legs, crosses over at the bottom joint and then returns through the

other leg. The minimum length of the sample is given by the profile of the applied magnetic field. The soldered joints have to be outside the high field section (see appendix D). The Nb-Ti cable sections are busbars interconnecting the sample and the current leads.

Both legs can be completely instrumented, but most of the time only one of the two legs is used while the other leg has a few voltage taps for measuring the critical current and to allow for quench detection.

4.1.2 Heat treatment

To form the Nb_3Sn phase in the conductor, a heat treatment is necessary. The optimum combination of consecutive temperature levels and duration depends on the type of Nb_3Sn wire in the cable. After the heat treatment the shape of the sample is fixed, so the sample has to be held in the desired shape during the heat treatment using a heat treatment mold, as shown in figure 4.2. This consists of square steel bars with the same lateral size as the cable width, kept in place with a clamping system of bolts. The bottom and top plates help to ensure a homogeneous temperature distribution across the sample.

The cables are wrapped with glass fiber tape. This serves two purposes. Firstly, it ensures that the cable does not sinter to the steel bar, secondly it reinforces the epoxy used to impregnate the sample in a later stage. Because the sample is brittle after the heat treatment, the glass fiber tape is wrapped around the cable before the heat treatment. This same procedure is also used in magnet coil windings and thus results in a representative sample.

4.1.3 Impregnation

Since Nb_3Sn is a brittle material, it cannot sustain the electromechanical forces without proper support. Because of the voids in the cable, pressure concentrations arise in contact points in the cable between crossing strands. To fill these voids, the cable is vacuum impregnated with epoxy resin. In addition impregnation guarantees suppression of strand movement, which helps to prevent severe training of the

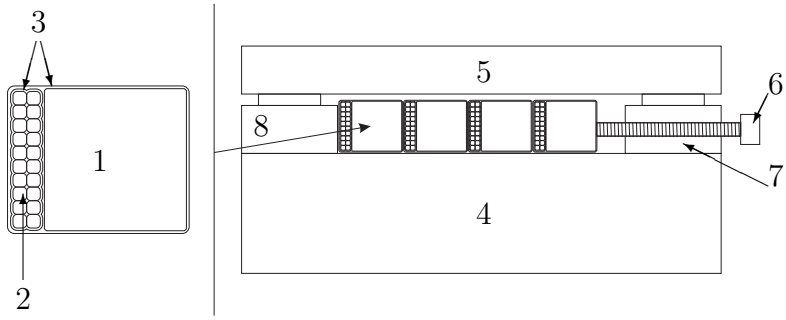

Figure 4.2: Sketch of the sample heat treatment mold. A steel bar (1) is used on which the sample (2) is fixated with glass fiber tape (3). A stack of these is placed on a steel base plate (4). The stack is compressed by a bolt between two bars (7 and 8), which in turn are bolted to the base plate. A cover plate is placed on top (5).

conductor sample.

The cable sample is placed in a tightly fitting mold already wrapped in glass fiber tape. The mold is pumped vacuum and then slowly filled with resin while the vacuum is maintained. In the ideal case the resin is penetrating the cable by the capillary force. The use of glass fiber tape improves the process, because the voids between the fibers are much smaller than those in the strands, so the capillary force is much stronger. This reduces the chances of voids forming in the sample. To control the impregnation time, the samples are impregnated in a tilted position, so that the total travel distance of the fluid level is greatly reduced, see figure 4.3.

At the start the system is pumped and left to degas. When a satisfactory low pressure is achieved, a small amount of epoxy resin is deposited in container 1 from outside the vacuum chamber through a controlled valve. This is allowed to seep into the mold. The container is slowly filled with short bursts of epoxy resin. In this way a controlled build up of resin is achieved at the entry side of the mold. When the resin appears at the exit side of the mold, a large amount

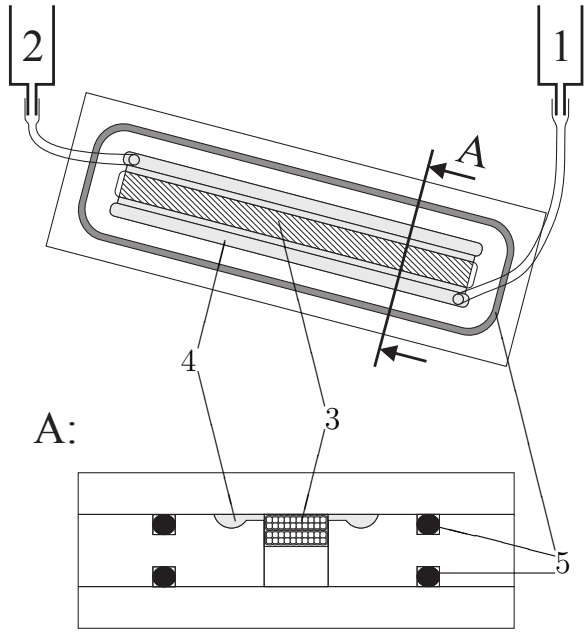

Figure 4.3: Schematic view of the impregnation process; the top picture shows the process with the top cover removed and the bottom picture is a cross section at A. The sample (3) is impregnated with resin from container 1. The resin is distributed over the sample by a slit (4). The mold is sealed with O-rings (5).

of epoxy is deposited in the container to create some additional flow. After the resin is left to settle for a short while, the vacuum is broken and the mold is put under ambient pressure. Finally, the mold is placed in a furnace to cure the epoxy.

4.1.4 Instrumentation

The sample is fitted with the required instrumentation before or during the assembly of the sample holder.

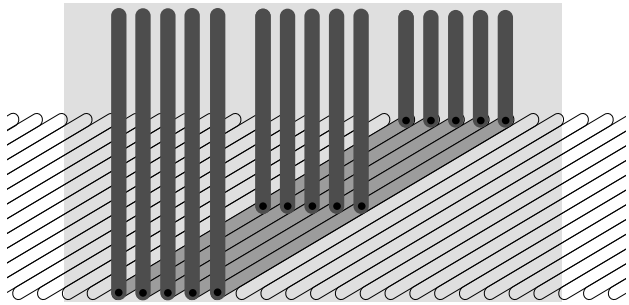

Figure 4.4: Schematic layout of the strand heaters. Five strands (highlighted with darker gray) are tested at three different locations.

Voltage taps

Voltage taps are used to measure potential differences across the sample at certain key locations. This allows to record the voltage-current curve and also to enable proper quench detection. The first samples were measured using so-called voltage tap strips. The strips have the same length and width as the cable sample and are placed between the cable and the filler piece in the assembly. This ensures that the location of the voltage taps is always the same. To create the electrical contact, the insulation locally has to be removed from the wide edge of the sample. Since this is the face of the cable that sees the transverse pressure, this method induces a small risk of local stress concentrations in excess of what the sample can sustain. In later samples, wires soldered to the thin cable edge are used, which leaves the wide edge of the sample clear of any manipulations. This removes the risk of damage due to pressure concentrations and leaves more options to define the positions of the voltage taps. Both systems are more accurately described in appendix D, together with the magnetic field profile across the sample as provided by the FRESCA magnet.

MQE heaters

To determine the thermal stability of the cables, it is essential to apply controlled thermal perturbations to the sample. For this purpose

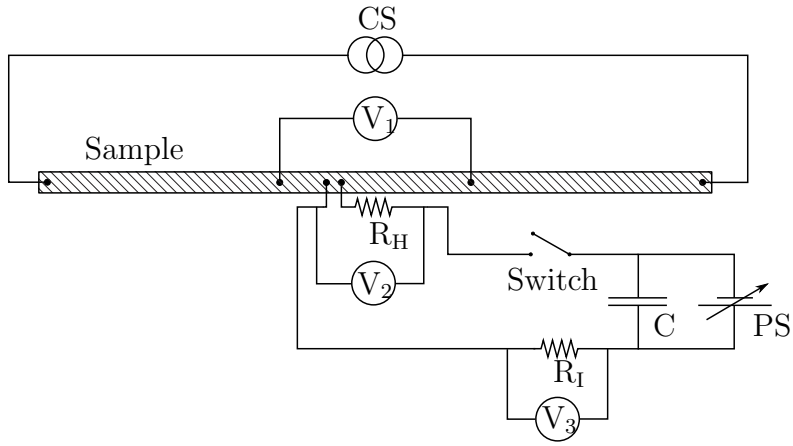

Figure 4.5: Electrical scheme of the heater powering. To avoid any earthing conflicts, both circuits are floating.

special Minimum Quench Energy, or shortly, MQE heaters are developed. They consist of a self adhesive sheet of polyimide with copper paths printed on. The layout of the paths is shown in figure 4.4. The sheet is slightly wider than the cable, so that it extends into the open space in the sample holder. Here the electrical connections can be made to wires leading to the heater power supply. A 0.5 mm diameter hole is made transversing both the copper path and the polyimide. Since the copper is insulated from the cable, there is no electrical connection yet. This connection is made by filling the hole with a graphite-loaded epoxy paste. The paste forms a spot heater with a size smaller than the strand diameter in direct contact with a selected strand in the cable sample. The efficiency of the heater will be discussed more thoroughly in section 4.5.3. To achieve maximal efficiency and minimal response time, the heater uses the cable as return lead. To close the circuit a similar conductive strip is used. A small strip of polyimide covered with a copper path, is placed on the sample. This strip is positioned with the copper path directly on the cable. It is placed one twist pitch away from the heaters, so that it will touch the same strands on which the heaters are placed.

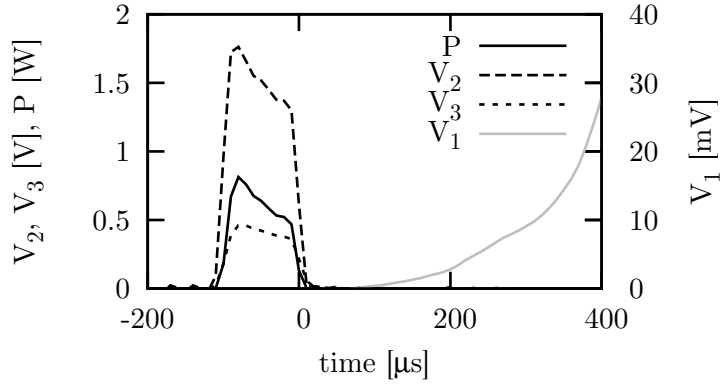

Figure 4.6: Sample voltage response to a heat pulse plotted against time. The voltages are labeled the same as in figure 4.5. P is calculated as described in the text.

The heaters are powered by a pulse generator in single pulse mode. The electrical scheme is shown in figure 4.5. The heater resistance (R_H) is connected via a timed switch (Switch) to a capacitor bank (C), charged by a variable power source (PS). To regulate the total deposited energy, the voltage drop over the capacitors is varied. Alternatively, the time the switch is closed can be varied to regulate the energy. For most experiments the shortest possible pulse yields the most interesting value, so the voltage is changed while the pulse length remains constant. The voltage is measured with a digital oscilloscope at V1, V2 and V3. V1 is used to determine if the sample quenches due to the heat pulse. V2 and V3 are used to measure the energy of the heat pulse. V2 measures the voltage drop over the heater as a function of time and V3 does the same for the drop across a known resistor (R_I). To retrieve the energy, the voltages are multiplied, divided by R_I and then numerically integrated. An example of a sample response to a heat pulse is shown in figure 4.6. This particular heat pulse indeed induced a quench in the sample. The voltages from the scheme in figure 4.5 are shown as a function of time.

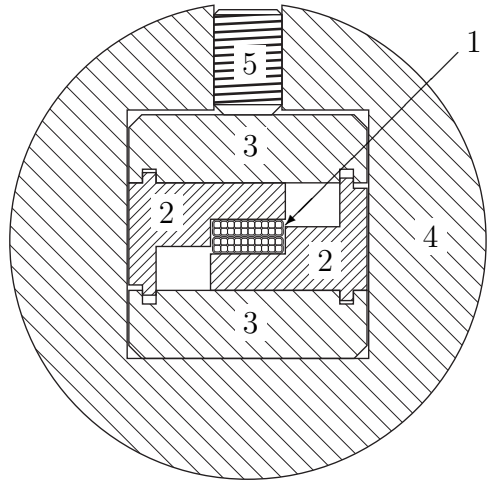

Figure 4.7: The sample (1) is placed between to glass fiber reinforced filler pieces (2), which are bolted to a stainless steel blade (3). The blades are compressed in the collar (4) by a bolt (5).

4.2 Sample holder

The first sample holder to test Nb_3Sn cable samples in FRESCA was made in 2004 [55]. This sample holder is optimized for robustness and protection of the sample. However, it does not leave any access to the sample for additional instrumentation, such as MQE heaters. Therefore, a new design is made with the emphasis on flexibility and sample access.

The entire sample holder is 2 meters long, but the only relevant part is the section of the sample holder in which the Nb_3Sn sample is positioned. This has a fixed cross section over the full 1.15 m length, which is shown in figure 4.7. The sample is located in the center and it is surrounded by filler pieces of glass fiber reinforced epoxy. The filler pieces are custom made for each sample to ensure a uniform stress distribution over the sample. Around the filler pieces, two stainless steel plates are placed, the so-called blades. The dimensions of the filler pieces are chosen such that together with the blades they form

a 35.0 by 35.5 mm rectangle, which can be slid into the collar. The collar is a 69 mm diameter rod of stainless steel with a rectangular hole in the center where the previously described parts can be placed. Every 40 mm there is an M16 bolt, which is used to apply transversal pre-stress on the sample. The bolts are tightened using a torque wrench, set at a certain value depending on the desired level of pre-stress and on the cable sample width. Following common practices for bolt dimensioning the required torque for the desired force is calculated.

The support structure is made from 316LN stainless steel, which has the required structural properties and has negligible magnetization [80]. The steel parts of the sample holder (blades and collar) are made from the same material.

There are two rectangular holes left open by the filler pieces, which allow for the electrical connections of various sensors and improved cooling of the sample. As shown in figure 4.7, each filler piece does not support the opposing steel blade. Care is taken that a 0.5 mm play is left after assembly, ensuring that any force exerted on the steel bar is transferred completely to the sample. If the filler piece bears any force, the stress on the sample would be unknown and the stress distribution could be changing over the width of the sample.

4.3 Cable test station

The FRESCA test station was designed in the late 90's to test the Nb-Ti cables for the LHC [24]. The setup is suitable also for testing other conductors. Already in 2005 the first Nb_3Sn cable tests took place in FRESCA [56].

A schematic drawing of the test station is shown in figure 4.8. The magnet can generate a magnetic field up to 10 T over a length of 500 mm. The temperature of the sample can be regulated at 1.9 or at 4.3 K. The maximum cable test current is 32 kA.

Since the magnet is relatively large and requires a long time to

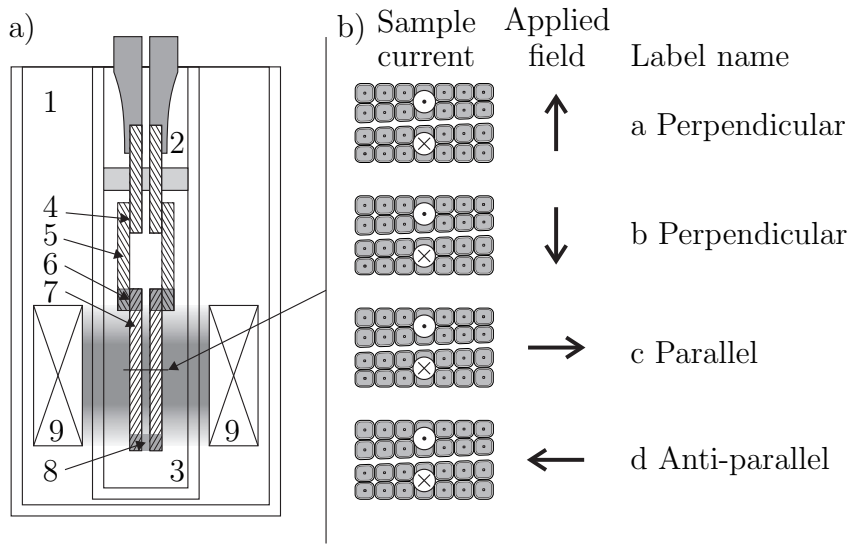

Figure 4.8: Schematic drawing of the FRESCA test station a) and the four possible sample current and applied magnetic field combinations b). The FRESCA test station comprises an outer cryostat (1), top inner cryostat (2) (4.3 K), lower inner cryostat (3) (1.9 or 4.3 K), indium clamping joints (4), Nb-Ti current leads (5), top joints (6), cable sample (7), bottom joint (8) and the magnet (9). The colored area indicates the location of the applied magnetic field.

cool-down compared to the sample, a double cryostat is used. This means that it possible to operate the magnet at 1.9 K while the sample temperature is 4.3 K . The inner cryostat that houses the sample is divided by the lambda plate in an upper and lower half. The upper half connects the room temperature current leads to superconducting leads. The sample is connected to the power supply via copper current leads, which are soldered to Nb-Ti cables carrying the current through the lambda plate. The lambda plate isolates the sample from the helium bath in the upper cryostat, enabling to cool-down the sample to below the lambda point (2.17 K). Indium clamping joints are used to connect the sample to the current leads. Indium is used instead of solder because it results in a connection that still has

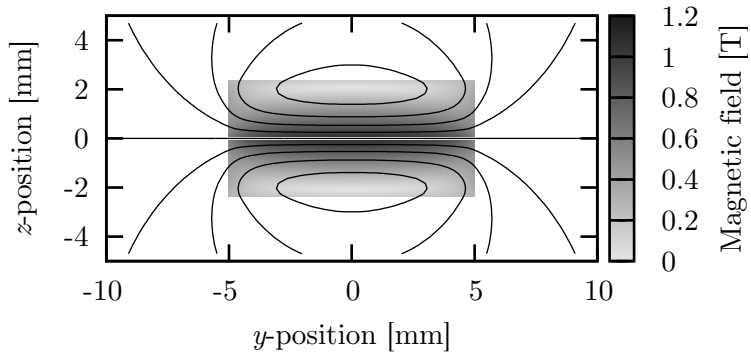

Figure 4.9: Magnetic field map of the self-field in a typical sample cross section at a test current of 10 kA, showing the magnetic field value in tesla. The density plot indicates the absolute magnetic field value and the black lines are the equipotential lines of the vector potential.

an acceptably low resistance (2 nΩ vs. 0.5 nΩ in the soldered joint), but avoids re-soldering the current leads for every sample. To make the joint, a 0.1 mm thick sheet of pure indium is placed between the two Nb-Ti cables. This sandwich structure is compressed between two copper blocks. The two blocks are wider than the cables with one row of bolts on either side of the cable to maintain pressure on the joint. Additionally, the sample contains three soldered joints, two top joints and one bottom joint; these will be discussed in a later section.

The sample can be oriented either perpendicular or parallel to the magnetic field and the polarity of the magnet can be inversed. This results in four different permutations of the applied magnetic field (figure 4.8 b). As discussed in section 4.1.1, the sample consists of two cables with inverted current flow in a bifilar configuration. The self-fields of the two cables add up in between them and negate each other on the wide outer faces of the sample stack (see figure 4.9). This results in a peak magnetic field on the wide "inner" side of the

cable, i.e. the side nearest to the other cable. Conversely the self-field is zero in the center of the strands on the opposite side of the cable. Since the peak magnetic field is about 1 T per 10 kA, the gradient over the cable is approximately 1 T/mm per 10 kA. The precise value depends on the geometry of the sample cross section.

When the self-field and the applied magnetic field are superimposed, this results in a total magnetic field in the sample cross section, such as shown in figure 4.10. The values taken in this example (20 kA at 9 T) are characteristic for these cables. The four directions result in a varying value and location of the peak magnetic field, transversal pressure and torque. It is trivial but nevertheless important to note that at the position where the self-field is zero, the total magnetic field is equal to the applied magnetic field. This will be a vital factor for the evaluation of the MQE measurements later on, since the stability experiments will be carried out at this position.

As an example the EM forces are calculated for the four cases presented in figure 4.10. The transversal inward force (i.e. perpendicular to the wide side of the cables), is nearly zero for the perpendicular cases, -16 kN per meter conductor in the applied magnetic field. This is purely the result of the self-field of the cable as in these cases the applied magnetic field does not contribute to the transversal stress. For the parallel and the anti-parallel cases the applied magnetic field does contribute and the values are -196 and +164 kN per meter respectively. This results in a transversal stress of -20 and +16 MPa for a 10 mm wide conductor respectively. The torque is strongest in the perpendicular case, 440 Nm per meter. The torque is zero in the two parallel cases.

The sample must be properly supported to withstand these forces. First of all, the supporting material must be strong enough and secondly, the wires in the cable must be supported evenly without any stress concentrations. How this is achieved is explained in section 4.2.

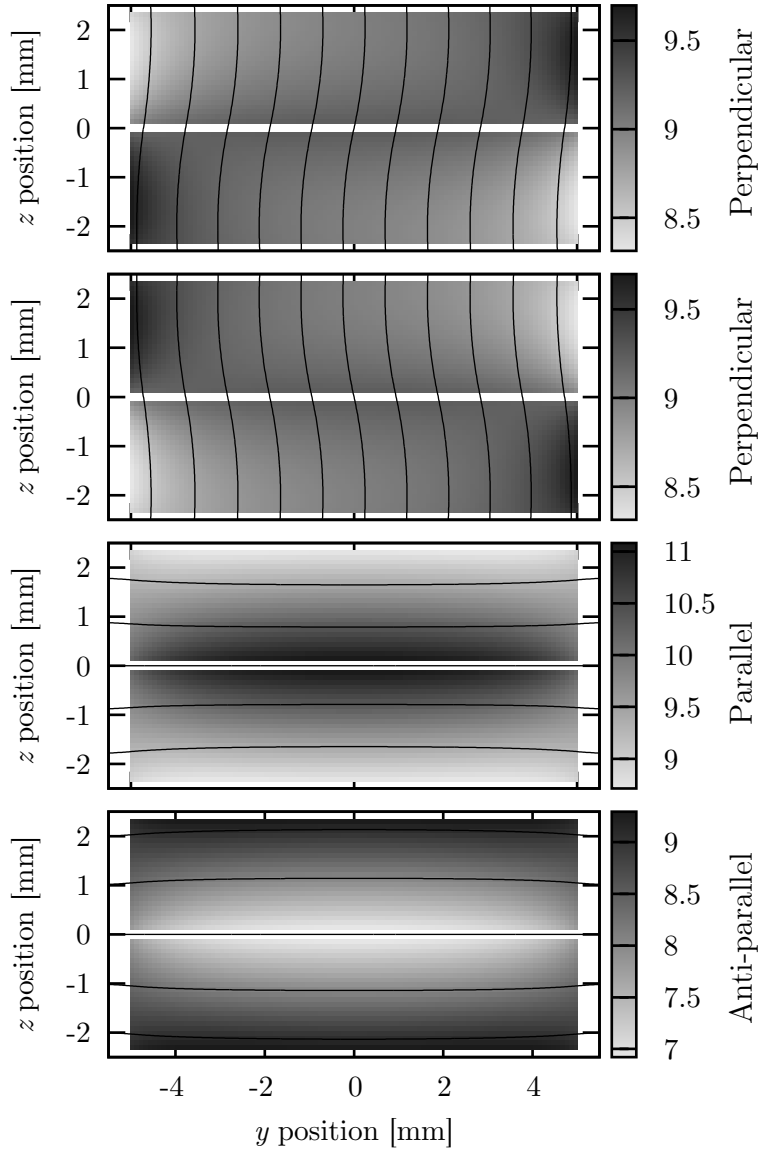

Figure 4.10: The total magnetic field as a function of the location in the sample cross section at a test current of 20 kA. An external magnetic field of 9 T is applied in the four directions given in figure 4.8. The density plot indicates the magnetic field value and the black lines are the equipotential lines of the vector potential.

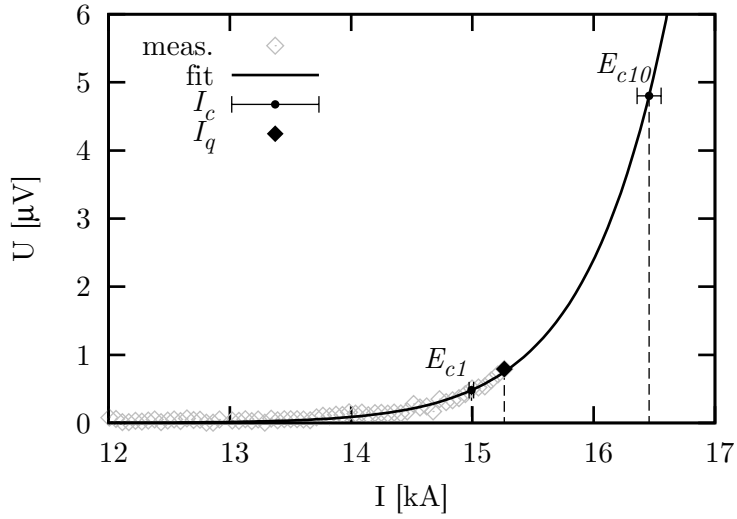

Figure 4.11: Sample voltage versus test current in a typical I_c measurement. The open symbols show the measurement, the line is the n-power law fitted to the measurement and the closed symbols are the derived I_c and I_q values.

4.4 Measurement procedures

The data points that are presented elsewhere in the thesis are not measured directly, but they are determined with the aid of different algorithms applied to the data acquired from the instrumentation. In the following sections the algorithms are presented and their possible influence on the results is discussed.

4.4.1 Critical and quench current measurements

The critical current can be defined with the aid of several criteria, such as a critical electrical field, resistivity or dissipation level [81]. Here the electrical field definition is chosen, with a criterion E_c of

1 µV/m. To determine the I_c value, the n-power law is applied:

$$E = E_c \left(\frac{I}{I_c} \right)^n \quad [\text{V/m}]. \tag{4.1}$$

Here E is the electrical field over the sample found by dividing the potential difference of the voltage taps by the distance between them. The distance is ∼0.5 m depending on which pair is used. The n in the formula is the so-called n-value. The function is fitted to the voltage-current curve with I_c and n as fitting parameters. An example is shown in figure 4.11.

The I_c point with the label E_{c10} is calculated with a criterion of 10 µV/m, which is commonly used for Nb_3Sn wire measurements. Often a cable measurement only reaches about a fifth of the critical electrical field. This results in an error on the I_c of 0.6%. If the criterion is lowered to 1 µV/m (E_{c1}), the error reduces significantly to 0.1%. The differences in normalized I_c between cable and wire are often only a few percent, so to make a fair comparison lowering the criterion is mandatory.

The current at which the cable develops a propagating normal zone is noted as the quench current. In the present work, its value is defined as the current for which the voltage over a single voltage tap pair exceeds 10 mV and does not recover without reducing the current to zero. This is commonly the last point measured in the U(I) curve indicated by the diamond marker in figure 4.11.

Magnetic field correction

As explained in section 4.3, the self-field of the samples is significant and can even exceed the applied magnetic field in some cases. Therefore, all the I_q and I_c values will be reported using corrected values of the magnetic field. The results will be compared using the peak value of the total magnetic field value in the conductor cross section, B_{peak}. The calculation of this quantity will be described in detail in section 4.5.1 and appendix E.

This is standard praxis for the reporting and compensation of I_c values. However, its use for the comparison of I_q values is debatable,

since a quench may originate from any location in the cable cross section. This implies a large uncertainty in the magnetic field error of approximately 0.1 T/kA transport current.

To verify which magnetic field value is more relevant, several measured datasets have been compared and checked for correlation between the $I_q(B_{app})$ and $I_q(B_{peak})$. The most striking example is sample D, shown in figure 4.12. When the data is plotted against applied magnetic field, the result is a data cloud that converges only at zero applied magnetic field. With the correction applied, the results become more consistent. Note that the I_q measured in anti-parallel applied magnetic field (downward pointing triangles) briefly increases when the applied magnetic field increases from zero to 2 tesla. In this case the applied magnetic field decreases the peak magnetic field in the conductor. This reduction in peak magnetic field clearly increases the I_q. Note that the extracted strand values are also corrected for peak magnetic field.

These observation constitute strong evidence that, just like I_c, the I_q values in the cable are limited by the value of the peak total magnetic field in the sample cross section.

Typical measurement

The I_c and I_q values are thus measured as a function of the peak magnetic field in the sample cross section. As an example, figure 4.13 shows some fictional measurement results (fictional data are used to illustrate all relevant effects in a single plot). For this example, the sample is assumed to be measured in parallel applied magnetic field, resulting in a 0.1 T increase of the peak magnetic field per 1000 A test current. At zero applied magnetic field and maximal test current (32 kA), the peak magnetic field in the sample is therefore 3.2 tesla. The result is a "slanting" of the experimentally accessible window. Whenever the test current is ramped up, the peak magnetic field in the sample cross section B_{peak} starts to deviate from the applied magnetic field following the sample load line (the thick black line in figure 4.13). The slope is determined by the geometry of the cable

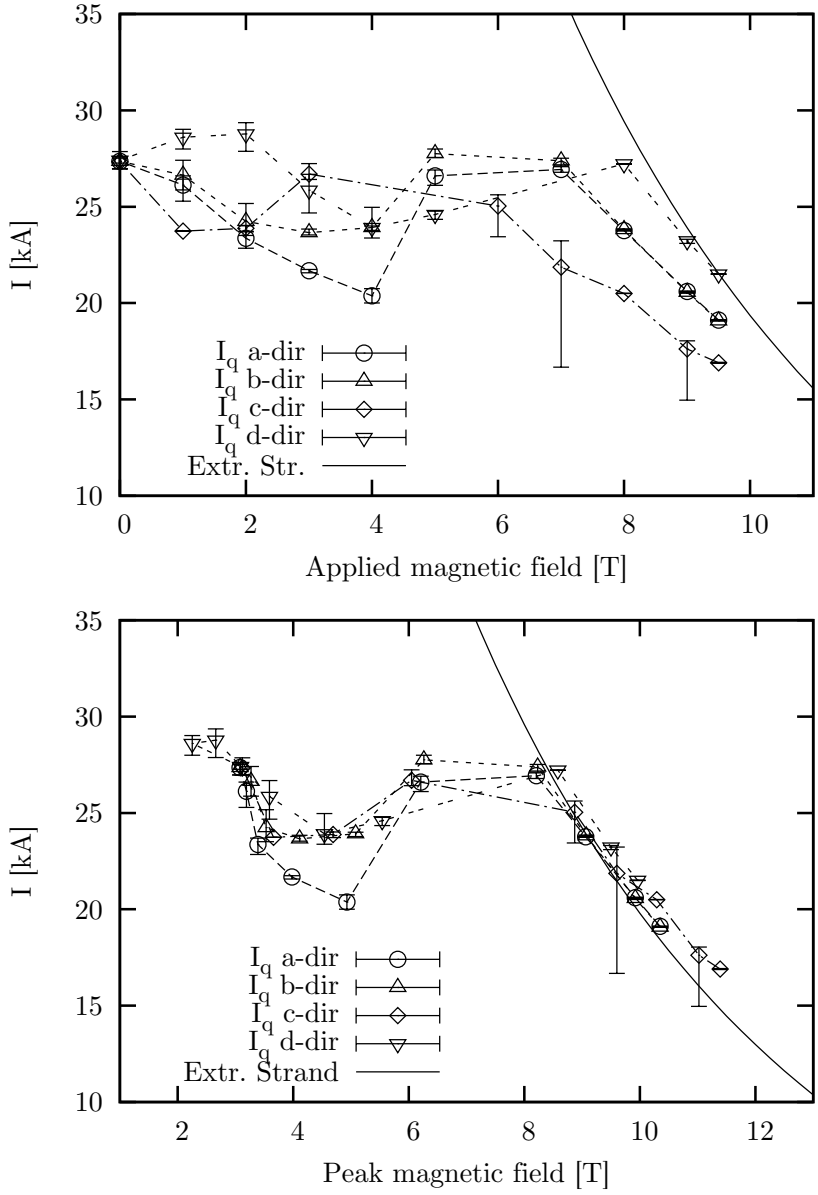

Figure 4.12: Quench currents plotted against applied magnetic field (top) and peak magnetic field (bottom). These results are obtained with sample D.

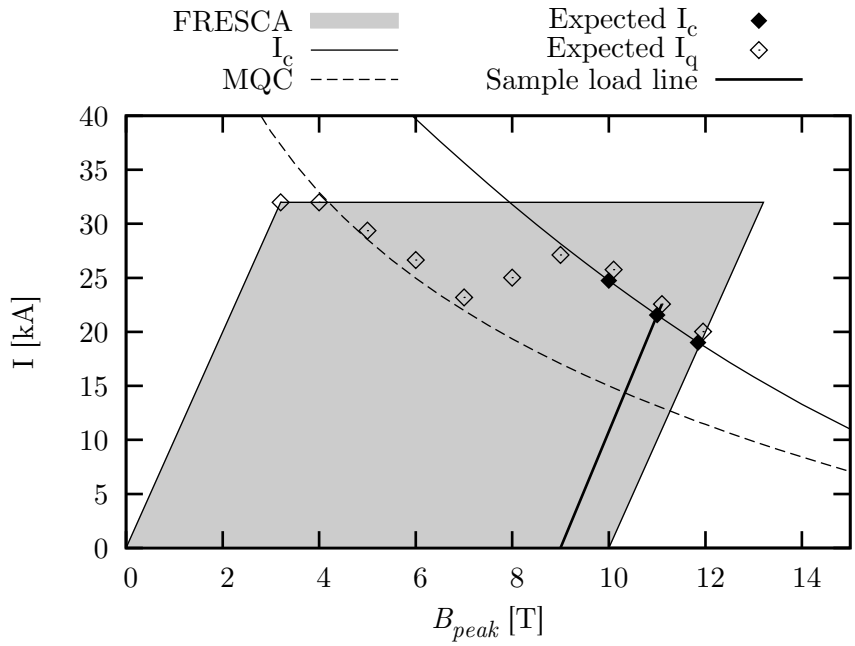

Figure 4.13: Fictional data illustrating the current carrying performance versus the peak magnetic field. The gray area shows the limits of the test station, the thin line shows the limits of the critical current, the dashed line the minimum quench current MQC, the open symbols denote the quench currents and the closed symbols the critical currents. The thick black line shows the load line of the sample for a 9 T test.

and by the direction of the applied magnetic field.

If the sample is limited by self-field instabilities, the quench current tends to follow the minimum quench current (MQC) line (dashed line in figure 4.13), as described in section 1.4.1. Until the magnetic field is high enough so that the self-field instabilities are not limiting any more.

In a measurement the test current is ramped up at a constant rate until the cable quenches. There are three different possible outcomes

of such an experiment, all shown in figure 4.13:

1. The sample reaches the critical current limit and quenches due to ohmic heat generated by the normal current;
2. The sample quenches prematurely due to a flux jump, a thermo-magnetic instability or a large mechanical perturbation;
3. The sample reaches the power supply limit but does not quench.

In the first case, the critical current is evaluated and the quench current is recorded. The I_c and I_q can differ by 1 kA or more in extreme cases, see figure 4.11. The quench current can be either larger or smaller than the critical current, depending on the cooling of the sample and on the n-value.

In the second case the quench current is recorded. Since the quench is triggered by a random thermal fluctuation or mechanical motion, some spread in the results is expected when the measurement is repeated.

In the final case, the result is omitted from the plot, since it contains no information on the sample properties. In this example they are included for illustrative purpose.

In a typical measurement at high magnetic field the sample will reach I_c, then will undergo a transition to the instable regime, dominated by the thermo-magnetic instabilities. There is no guarantee that this will happen as the transition can move to higher or lower field. If the cable is less stable, it may well never reach I_c over the measurable range of the test station. If it is more stable, it can reach the power supply limit before it becomes unstable.

4.4.2 Minimum Quench Energy

The procedure to measure MQE is identical to the one explained in [49]. Before the MQE measurement starts, the magnet of the test station is ramped to the desired magnetic field level. This induces coupling currents in the sample, which could influence the current distribution. To remove them, the sample is brought to quench with a fast current ramp and the resulting data is discarded. This fast

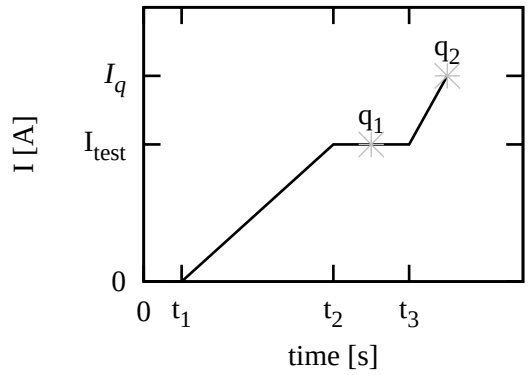

Figure 4.14: Current versus time plot of an MQE measurement. The current ramp starts at t_1 and ramps to the test current I_{test}. From t_2 to t_3 the operator can activate the heater, resulting in a possible quench q_1. If the sample does not quench a fast ramp starts at t_3, to quench the sample at its quench current I_q.

ramp brings the sample temperature over the critical temperature, temporarily extinguishing all superconductivity in the sample and thereby reducing coupling currents to a negligible level.

The following MQE procedure is summarized in figure 4.14. First the current is ramped up to the test current. The ramp rate is fixed at 300 A/s to ensure repeatable results. Here the current is kept at a stationary level for several seconds to allow the operator to activate the heater. If the sample quenches at q_1, the energy is recorded as a quench energy and the measurement cycle is finished. If not, the sample is quickly ramped up further to the normal quench current of the sample, to quench at q_2. The increased ramp rate reduces the measurement time. The sample has to be quenched after each heat pulse to ensure that each measurement has the same starting conditions.

To obtain the quench energy of the sample, the heater energy is changed between cycles. After the first test, the energy is doubled if there is no quench or halved if there is. This is continued until an

upper limit for the minimum quench energy and a lower limit for the maximum no-quench energy is found. As soon as both these values are obtained the mean value is used for the next cycle, reducing the difference in energy by a factor two compared to the previous step. This is repeated until the difference between the minimum quench energy and maximum no-quench energy limits is less than 10 % of the average of the two values. This finally results in a 5 % error in the MQE value.

Once this value is obtained, the two data points enclosing the quench energy are treated as described in section 4.1.4. The measured heater voltage and current are multiplied and integrated over time to find the precise energy dissipation. The energy is then multiplied with the appropriate heater efficiency factor to correct for heat leakage, as calculated in 4.5.3. The procedure results in a single MQE point for one value of current, magnetic field and temperature. On average it takes 5 cycles to arrive at the required accuracy level.

4.4.3 Residual Resistivity Ratio

The RRR value of the cable samples is determined by comparing the resistivity at room temperature with the value just before the transition. The resistivity is determined by measuring the voltage drop over a length of conductor at a stationary current. The same voltage taps as for the critical current measurements are used. Because the cable is in the normal state, a relatively small current of 10 A is applied at room temperature. Because the current is constant and the cable is impregnated with epoxy, larger currents might slowly warm up the sample over time. When the temperature drops, the current can be increased, since the resistivity decreases as well.

A typical measurement result is shown in figure 4.15. The voltage drop is first measured at room temperature. Between 290 and 260 K there is a small gap in the temperature data caused by a small heat leak to the external cryostat, which results in a slow cool-down of the internal cryostat. During this period the instrumentation is checked and the test station is prepared for the cool-down and no data is

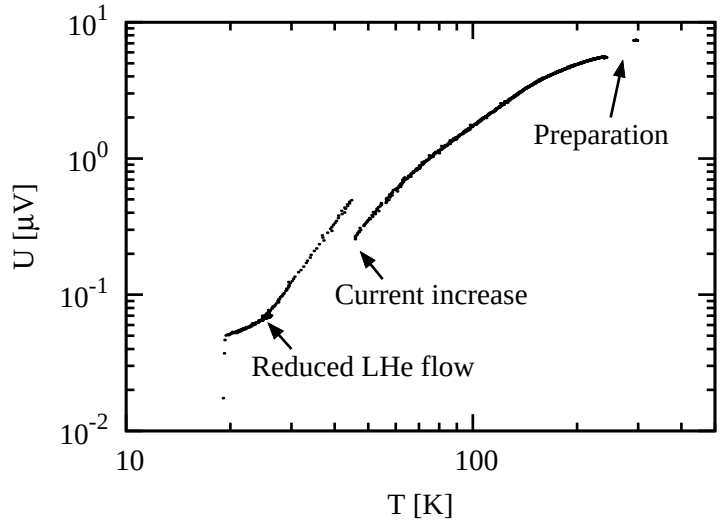

Figure 4.15: Voltage as a function of temperature during an RRR measurement. The voltage drop over a VT pair is measured with a stationary current. At 45 K the current is doubled to increase the accuracy of the measurement.

taken. Once the actual cool-down of the internal cryostat has started, the measurement is resumed. When the temperature reaches 45 K the current in the sample is doubled to 20 A to increase the accuracy of the measurement.

Around 30 K the inlet of liquid helium into the cryostat is throttled in order to decrease the cool-down rate. With this setup, approximately one point every 20 seconds is registered. In figure 4.15 it is clearly seen that around 30 K the point density changes due to the change in cool-down rate. This is deliberatly done to increase the accuracy. There is a clear transition at 18 K, where the sample becomes superconductive. To determine the RRR value an average of the last 10 points before transition are taken and compared to 10 points taken at 290 K. The value of the voltage drop at room temperature is divided by the low temperature value and multiplied by

a factor two to account for the change in current.

4.5 Numerical estimates

There are known errors in the system that need to be estimated in order to evaluate the results properly. In this section the self-field calculation will be explained. Furthermore, the influence of the transverse pressure on the sample and of the efficiency of the spot heaters will be discussed. Magnetic field value, stress and heat flow are quantities, which are difficult to measure accurately inside an object. However, using a FEM simulation a good estimate can be made.

4.5.1 Self-field estimate

The cables tested comprise high-J_c strands and high current density implies a high self-field. To make a fair comparison of the cable performance with respect to the performance of the constituent wires, the magnetic field has to be known in both types of samples [82]. The calculation of the magnetic field distribution in the cable cross section is explained in detail in appendix E. In short, the cable is assumed to be infinitely long and to have a perfectly homogeneous current distribution. The main components of the applied- and the self-field are found in the y and z-direction. There will be a small axial component in the self-field when the cable is twisted, but this is neglected here.

These assumptions allow for a 2D model of the cross section of the sample. The model lays an equidistant grid over the two cables and divides the current over these points. Each element is considered as an infinitely long wire, for which the magnetic field can be calculated with the Biot-Savart law.

Examples of the calculations are shown in figures 4.9 and 4.10. The I_c and I_q measurements are corrected by using the peak magnetic field found in the cross section of the cable, assuming that the current

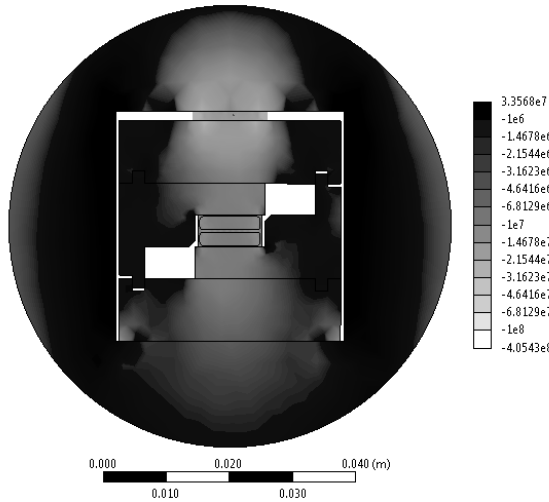

Figure 4.16: Pressure distribution in a cross section of the sample holder after cool-down. Note that this is a logarithmic color scale where black means no stress or tensile stress and white means high compressive stress.

is homogeneously distributed over the cross section.

4.5.2 Transversal pre-stress estimate

A small section of the sample holder is reconstructed in a 3D FEM model. Figure 4.16 shows a cross section of such a model. To limit the numerical effort, the smallest repeating part of the sample holder is modeled with periodic boundary conditions. The periodicity in the sample holder is determined by the 40 mm distance between bolts that apply the pressure on the steel blades.

The model takes into account the applied pre-stress, the differential shrinkage during cool-down and the effects of the electromagnetic force. The Young's modulus and dilatation of the materials from room temperature to 4.3 kelvin are required input. The values were found in the NIST online cryogenic material property database [65]. The glass fiber reinforced epoxy has anisotropic material properties.

The direction of the glass fibers in the filler pieces are known and is taken into account in the simulation. The bolt and collar have the same properties, since they are both made of stainless steel. Because the stress distribution in the collar is not relevant, the collar is modeled as a solid object, with the bolt simulated as a small disc inserted between the top blade and the collar.

To apply the pre-stress on the sample, a common numerical trick is used. From room temperature 293 K to 4.3 K realistic values for the material properties are used. From room temperature to an arbitrary higher value, 400 K, the Young's modulus is taken constant and the dilatation is set to zero for all materials except the disc. The disc gets a high negative dilation coefficient, which is chosen such that the model has the correct pre-stress at room temperature. So the model starts at 400 K with a completely stress free situation. The model cools down to 293 K, while the materials maintain their properties except the small disc, which expands and brings the model to the correct pre-stress. The temperature dependent material properties are taken into account as the model system cools from room temperature to 4.3 K.

In figure 4.17 the stress in the z-direction of the sample is plotted as a function of the axial x-direction, as defined in figure 4.1. There are two issues that can be learned from this example; firstly the variation in stress is ± 10 MPa and secondly there is a 5 to 6 MPa loss of pressure after the cool-down. The axial distribution of the stress is a result of the finite rigidity of the stainless steel blades in the sample holder. To improve this, a more rigid or thicker material is needed. The loss of pressure is due to the choice of materials. To improve this, either a filler material with a smaller dilatation factor is needed or the collar material must be replaced by a material with a higher dilatation factor.

At the start of the measurement, there is a homogeneous stress (σ_{start}) throughout the thickness (z-direction) of the cable. Since the electromagnetic forces are a volumetric force in the sample area, there will be a gradual change in the stress as function of distance to

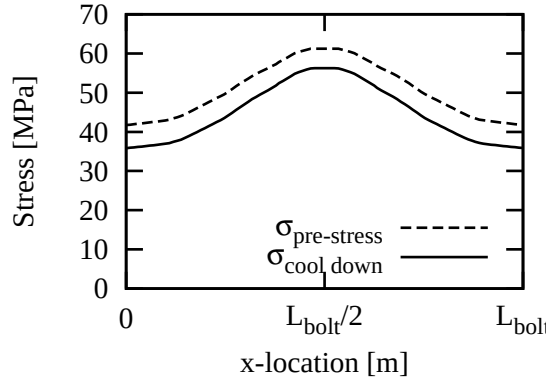

Figure 4.17: Stress distribution in the axial direction of the sample, after application of pre-stress (dashed line) and after cool-down (continuous line). L_{bolt} is the distance between two bolts (4 cm). The centerline of the bolt is placed at $L_{bolt}/2$.

the cable surface once the current is no longer zero. In the perpendicular applied magnetic field cases, there are no large forces in the direction of the applied stress. Therefore, only the parallel magnetic field directions will be examined here. If the self-field of the sample is neglected, the extremes in stress within the sample are approximated by:

$$\sigma_P = \sigma_{start} - \frac{I \cdot B}{w} \quad [\mathrm{N \cdot m^{-2}}], \tag{4.2}$$

$$\sigma_{AP} = \sigma_{start} + \frac{I \cdot B}{w} \quad [\mathrm{N \cdot m^{-2}}], \tag{4.3}$$

where I is the transport current, B is the applied magnetic field and w is the width of the sample. Then σ_P and σ_{AP} are the extremes in the stress in the sample for the parallel and anti-parallel field directions respectively. If one assumes the conductor to be perfectly homogeneous, the stress distribution will have the shape as figure 4.18. In the anti-parallel magnetic field configuration, the Lorentz force pushes the two legs of the sample together and the compressive stress is maximal on the central plane of the sample.

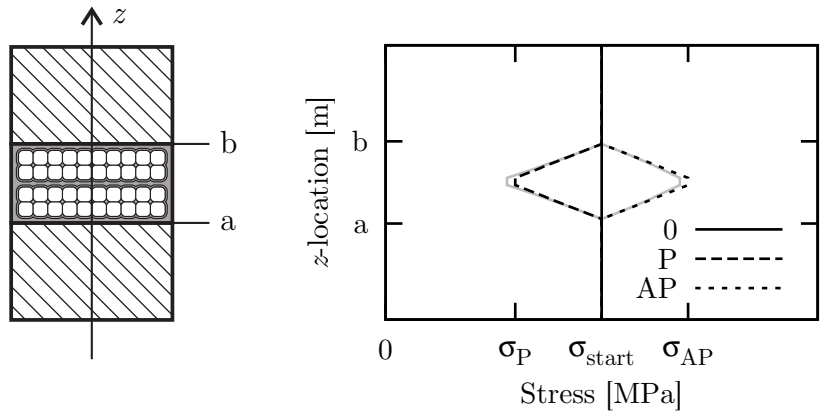

Figure 4.18: Pressure distribution in the z-direction of the sample. On the left a schematic drawing of the sample showing the position of the stress approximation plotted in the graph on the right. The stress is calculated at the start (0) and end of a measurement in the Parallel (P) and Anti-Parallel (AP) applied magnetic field direction. The stress distribution is plotted with (gray) and without (black) correction for the self-field.

In the parallel configuration, the Lorentz forces point outwards and counteract the applied compressive stresses. In the most extreme case (I = 32 kA, B = 10 T, w = 10 mm and parallel field configuration) the stress can be as high as 32 MPa. This means that the pre-stress applied on the sample must be more than this value. Since the epoxy has poor tensile properties the stress in the sample cannot be allowed to change sign. Tensile stress on the sample might result in rupture of the bond between the two cables in the sample and large irreversible I_c degradation.

Large variations in stress throughout the sample may also result in more subtle variations in the I_c, since Nb_3Sn is a strain dependent superconductor. According to [83] the Young's modulus of polycrystalline Nb_3Sn at 4.3 K is around 80 GPa. This means that the electromagnetic component in strain is approximately 0.04%. Interestingly, in the anti-parallel configuration the highest strain is found

in the center plane of the sample, where the magnetic field is the lowest. When some typical values are used with the scaling law from [64], it is found that around the working point of 10 tesla 0.04% extra strain will result in 5% reduction of I_c, whereas the reduction of the magnetic field by approximately 3 tesla will give 75% increase in I_c. This means that it is highly unlikely that the sample will be limited by the volume that experiences the enhanced strain levels.

As stated before, the self-field is ignored here to simplify the calculations. If the self-field is taken into account, the gray lines in figure 4.18 are obtained. In the parallel case the peak stress would be somewhat lower than calculated, because the self-field adds up to the applied magnetic field and exacerbates the effect. The self-field makes up about 10 - 20% of the total field, so if a safety margin of a factor two is used, there is no chance that the stress becomes tensile in the sample. In the anti-parallel case, the self-field counter acts the applied magnetic field, therefore the peak stress is alleviated some what. This means that the margins estimated for the possible reversible I_c loss seem even more secure.

4.5.3 Heater efficiency estimate

To scale the results from the quench energy measurements correctly, the precise amount of heat flowing into the conductor needs to be known. A similar approach as in [84] is taken. The parasitic heat flow to other parts than the strand is taken into account as well as the reduced efficiency due to finite diffusion time of the heat from the heater to the strand. Since a different type of heater is used than in [84], the calculation had to be repeated.

To obtain fair values for both correction effects, an estimate of the heat flow from the heater to its surroundings over time is made. Due to the complex geometry, a three dimensional model is required. So a non-linear transient FEM model is set up.

The layout of the FEM model geometry is shown in figure 4.19, with the insulating materials removed to better visualize the heater system. The heater is built on and insulated by adhesive polyimide

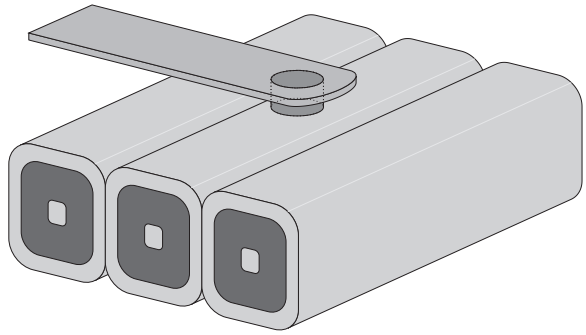

Figure 4.19: Schematic layout of a strand heater positioned on the strand surface. Surrounding materials (polyimide and glass fiber reinforced plastic) are removed to better visualize the heater.

tape. On top is a thick layer of glass fiber reinforced epoxy. The model includes the temperature dependencies of the thermal and electrical properties.

The model heat input is the same as in a measurement, a square potential pulse is applied to the current lead of the heater, while the cable remains at constant potential. The first conclusion is that the resistance of the current lead is negligible compared to the resistance of the heater and thus the same holds for the heat generation. To simplify the thermal model, the heat generation outside of the heater is neglected. With this heat generation as input, the thermal model is used to estimate heat flow to the various components: the heater touches three different components. The cable, the heater current lead and the polyimide insulation on the top and the sides of the heater. The surfaces touching the polyimide are summed up in one value.

The result is shown in figure 4.20. The heater element first needs to warm up to achieve a sufficient thermal gradient to generate appreciable heat flux to its neighboring components. The heat flux towards the current lead of the heater stabilizes faster because the heater generates more heat in the vicinity of the lead. At the end of the heat pulse the heat flux reaches its maximum.

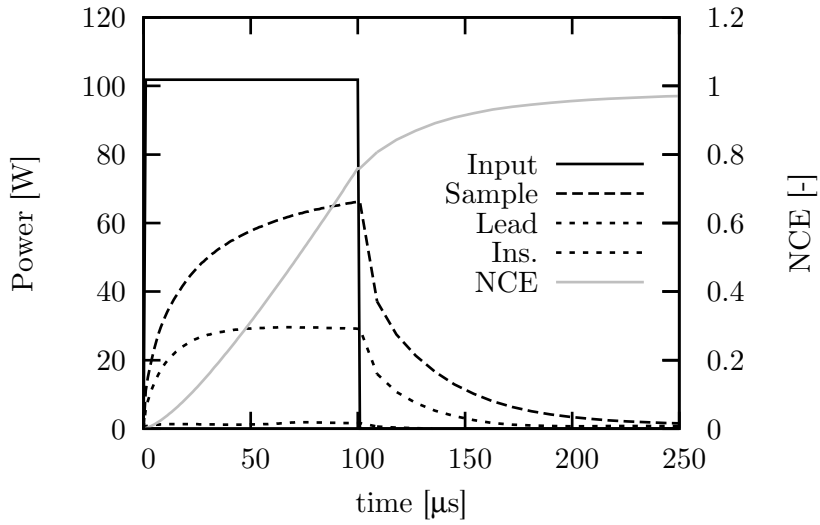

Figure 4.20: Simulated heat flows over time from the heater to various surrounding parts. "Input" is the power of the heater, "Sample" is the heating power to the sample, "Lead" is the heating power into the current lead of the heater, "Ins." is the heating power to the insulation around the heater and "NCE" is the Normalized Cumulative Energy going into the sample.

After the power supply is turned off, there is still residual thermal energy left in the heater and this will flow into the surroundings over some time. The heat flow is integrated over the entire heating cycle to quantify the energies that ends up in the various parts of the experiment. After 1 ms 69% of the total input energy has ended up in the strand. However, after the input pulse ends, the heat flux to the sample diminishes rapidly but still a significant amount of heat is deposited in the sample. To visualize this the Normalized Cumulative Energy (NCE) is plotted. At 100 µs 75% of the total energy that will be deposited in the strand is actually delivered. Therefore, around 25% will be delivered at a much decreased power. For cases where the MPZ is small and the quench develops quickly, the efficiency is

52% (69% times 75%). When the temperature margin is large the reaction time can be much slower and the efficiency will be close to 69%. The results are assumed worst case and the minimum quench energy is estimated at 52% of the input energy.

4.6 Conclusion

Sample details, sample holder and the cable test facility are presented. It is possible to mount a 1.5 m long bifilar hairpin sample, of which 1.15 m has the same insulation and surrounding materials as those commonly used in Nb_3Sn accelerator magnets.

Tests are possible in a background magnetic field up to 10 tesla, applied in four directions. The magnetic field in the sample cross section is calculated to make the necessary corrections for the $I_c(B)$ measurements. Both the absolute value and the location of the peak magnetic field are different for the 4 directions.

The electromagnetic forces on the sample are estimated in order to validate the amount of compressive pre-stress that needs to be applied to the samples and also to show that the effect on the I_c is negligible. A numerical estimate shows that the pre-stress of the sample changes during cool-down, but remains within acceptable limits for the test of the sample.

Specific features of the sample holder enable thermal stability tests on Nb_3Sn cable samples. The tests are performed using 0.5 mm diameter point heaters. To make quantitative statements on the MQE, it is essential to quantify the efficiency of the heaters to determine how much energy is actually transferred. A numerical analysis estimates the efficiency at 52% of the heater input power.

Chapter 5

Complementary measurement techniques

Aside from the cable tests in the FRESCA facility, several complementary measurements are performed for comparison and validation purposes. The performance of cables and magnets is normally compared to equivalent properties measured on the wires it is composed of. The following section will give a short description of these measurements. Several cable samples are tested using a cable test facility at the University of Twente. This setup will be described in the second section of this chapter.

5.1 Strand critical current

The common practice to determine the I_c of a single round superconducting wire is to wind and react it on a titanium barrel. The barrel can withstand temperatures of up to 875 °C in combination with a copper coated sample, see the phase diagram in ref. [85]. It can be reaction heat treated together with the cable samples. In this case, it is referred to as a witness strand. Both virgin wires and extracted strands from a cable section can be wound on a barrel. These are referred to as virgin and extracted samples respectively.

Figure 5.1: Rendering of two titanium I_c barrels. The grooved center section is the titanium barrel and the smooth end sections are copper terminals (left). The wire is wound around the barrel and clamped with two bolts (right). The wire is soldered to the terminals to achieve a low-resistance joint (not shown here).

An example of a barrel type sample holder for wires used at the University of Twente is shown in figure 5.1. There are minor differences between these barrels and the ones used at CERN: the inner diameter is smaller and copper terminals are connected differently to the barrel. However, previous work [86] has shown that the measured I_c of an identical conductor differs less than 2 % between CERN and the University of Twente. Measured values from the two laboratories will therefore be directly compared without further notice. When the measurements of the samples are compared to cable data, the values are multiplied with the number of strands in the cable.

Even though the turns on the barrel have a relatively large spacing, the self-field is still considerable and needs to be compensated for fairly comparing measurements [87]. In appendix E.2 the algorithm for determining the peak magnetic field on the wire sample is explained.

5.2 U-shaped sample holder for cables

The setup was designed and built in 1992 to investigate Rutherford cables for dipole magnets, see ref. [88]. A relatively short length of cable is placed on a stainless steel holder so that the cable is bent in a U-shape, see figure 5.2. The sample is placed in the bore of a solenoid, which generates the required applied magnetic field. Additionally, an electromagnetic press can be used to apply a transverse pressure on the cable. The test current is provided by a superconducting transformer.

There are several notable differences between this cable test setup and the FRESCA test station. The cable sample is much shorter and the sample section in high magnetic field is only 45 mm. However, much higher test currents are achievable up to 50 kA. Since the sample holder is mounted in a 79.5 mm diameter insert, it can be placed in any solenoid magnet which has a cryogenic bore of at least 80 mm. Currently the highest available magnetic field for this test station is 14 T. The electromagnetic press can apply a transverse force up to 240 kN. The maximal transverse stress depends on the surface area. On a 20 mm wide cable a stress up to 267 MPa can be applied.

In figure 5.3 the measurement range of the U-shaped sample holder is compared to the measurement range of the FRESCA test station. The U-shaped test station is capable of I_c measurements on much larger cables. The trade-off between sample size and measurement range is worthwhile for cables samples with a working point at 15 tesla or high critical currents. The FRESCA station has a higher peak magnetic field correction than the U-shaped setup because it has a bifilar sample. The peak self-field is approximately twice as large in the FRESCA station. If the two cables were pressed together and the copper layer is neglected the peak self-field would be exactly twice the peak self-field in the U-shaped sample holder. In practice it is slightly less due to the insulation between the cables and the stabilizing copper around the strands.

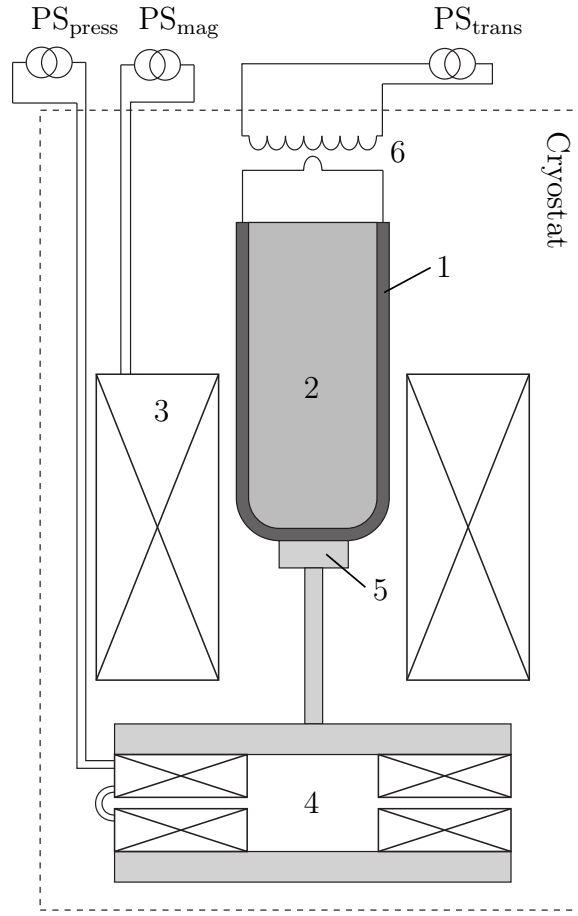

Figure 5.2: Schematic view of the U-shaped cable measurement setup at the University of Twente. The sample (1) is mounted on a stainless steel sample holder (2), the bottom of the U is placed in the center of the bore of a solenoid (3). Two anti-series connected identical coils (4) form a magnetic press, pushing a steel block (5) onto the sample with a well-controlled force. The sample is powered with a superconducting transformer (6) to reach the required test currents.

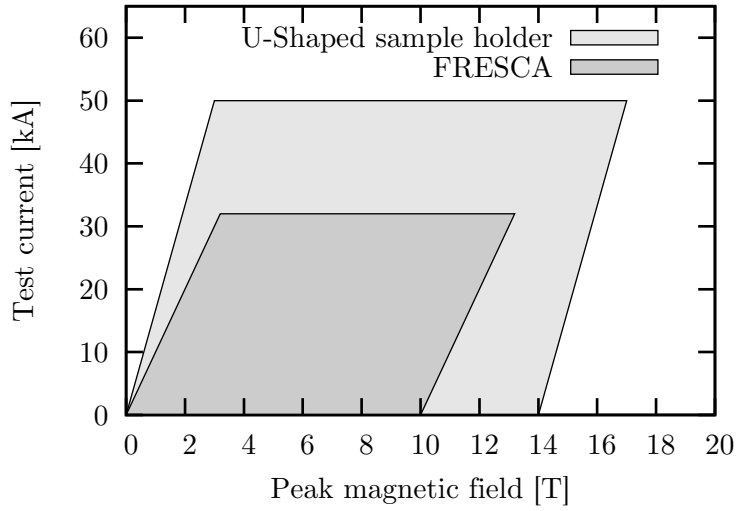

Figure 5.3: Measurement range of FRESCA compared to the U-shaped sample holder regarding test current and peak magnetic field in the sample. A typical sample size is used to calculate the peak magnetic field.

5.2.1 Adapted point heaters

The setup is adjusted to allow for thermal stability tests of full-scale Nb_3Sn cables for dipole accelerator magnets. The heater design shown in section 4.1.4 is modified to suit the U-shaped sample holder. Since there is less space available than in FRESCA samples it is not possible to measure the same strand at multiple locations. Instead of 5 strands with 3 heaters each, there are 9 strands with one heater each. The heaters are placed at the same distance from the edge as the point heaters used in FRESCA. Three heaters are placed 1 mm from the thick edge, three placed in the center of the cable and three 1 mm of the thin edge of the cable.

The cable sample is prepared with MQE heaters placed in the center of the high-magnetic field area of the setup, see figure 5.4. The return lead for the heater current is placed at the sample joint,

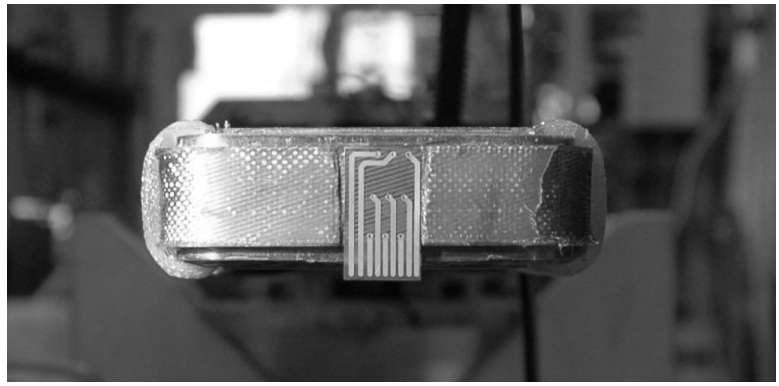

Figure 5.4: Photograph of the point heater system, before full assembly. The heater paste and polyimide insulation is not yet applied.

so that no additional sample manipulation is required. The heater dimensions and materials are identical to those used in FRESCA, so the efficiency is expected to by identical. For a schematic drawing of the test cross section see figure 5.5.

The cable is placed on the U-shaped sample holder (1), and placed in position with the side plates (2). After the cable and the glass fiber tape are impregnated with epoxy (3), the side plates are removed. The top layer of epoxy and glass fiber tape is removed and the heater system (5) is installed. This is the time when the picture in figure 5.4 is taken. The heater system is laying several tenths of millimeters under the original sample surface.

Several layers of adhesive polyimide tape are used to recreate the surface before the insulation was removed. The side plates (2) are re-installed, however, on one side the plate is extruded to make room for the electrical connections (dashed line). A stainless steel block is placed on the sample to apply adequate stress on the cable surface to counteract the electromechanical forces. The stress is applied by bolts on a stack of disk springs to maintain the pressure even though there is some discrepancy in the thermal dilatation of the various materials.

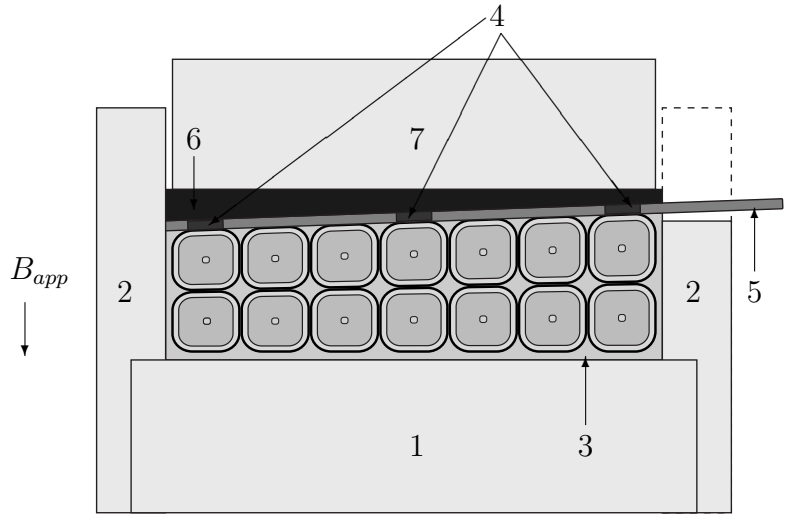

Figure 5.5: Cross section of the sample at the location of the heaters. The cable is placed on the sample holder (1) enclosed by two plates (2). The sample is impregnated with epoxy resin (3), which is removed at the broad side to fixate the heaters (4) integrated in a polyimide foil (5). Several layers of polyimide foil (6) are used to create a flat surface on which a steel block is placed (7). The number of strands in the cable is reduced for illustrative purposes. The applied magnetic field is indicated on the left. The direction of the current flow is into the page.

There is no direct contact of the cable with the helium bath. As is shown in figures 4.7 and 4.16, the FRESCA sample has direct contact with the helium bath at the thin edges of the sample. Here the sample is completely insulated with epoxy. The sample is enclosed in stainless steel on three sides and polyimide on the fourth.

The sample consists of a single active cable, with the applied magnetic field transverse to the broad side of the cable. This results in a significant difference between the applied magnetic field and the local magnetic field in the sample at the edge heaters. Furthermore, the self-field of the cable adds up to the applied magnetic field at the thick edge and subtracts from the applied magnetic field at the

thin edge. The magnetic fields are calculated with a FEM model as described in appendix E.3.

5.3 Contact resistance measurement

The contact resistance between the strands are required input parameters for the estimate of the MQE using numerical calculations. To determine the average values of R_a and R_c in a cable sample, an electrical contact resistance measurement is performed. A section of the cable sample is measured in a purposely built press described in [89] and the method is described in [90]. Two opposing strands

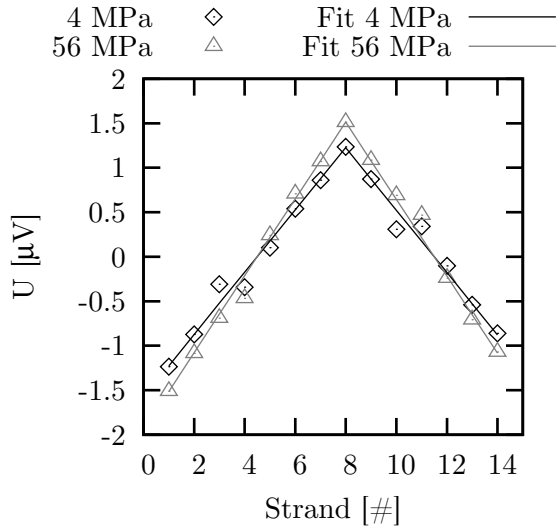

σ_{tr} MPa	R_c µΩ	R_a µΩ
<4	>100	0.46
56	>100	0.58

Figure 5.6: Electrical potential of each strand in the cable sample (left) and the results of the fit (right).

are selected and connected to current leads. Up to 14 strands are equipped with voltage taps. The sample is cooled down to 4.3 kelvin and a current up to 100 ampère is applied to the sample. The voltage taps are read out resulting in a potential measurement for each connected strand, as shown in figure 5.6.

Next a CUDI simulation is set up, with the same length and number of strands as the sample. The same current is used and the voltages are requested as output. The values of R_a and R_c are varied in the model until a minimum is found in the difference between the measurement and the simulation.

Sample A is tested at two different transverse stress levels, to determine the influence of the stress on the measurement. First the cable is loaded just enough to keep the sample in place on the sample holder at less than 4 MPa transverse stress. The sample is cooled down and measured. Afterwards the sample is warmed up and re-assembled under higher transverse stress, 56 MPa, which is comparable to the stress during the FRESCA tests. The setup is cooled down once more and the contact resistances are determined again. There is a small difference in the results, but, it is not possible to discriminate between the effects of the thermal cycle and the applied pressure.

Transverse pressure does not change the R_c and the R_a values significantly, as can be expected for impregnated Rutherford cables.

All samples tested for thermal stability in the FRESCA test station are measured in this setup. The results are summarized in table 5.2. The samples have a high R_c, which is caused by the low

Table 5.2: Contact resistances values found for the samples used for MQE measurements.

Sample name	R_c μΩ	R_a μΩ
A	>100	0.6
C	>1000	9.4
E	180	0.5
G	2000	510

transverse pressure on the samples during heat treatment and impregnation. The cross contacts are effectively not in contact after the heat treatment. When the samples are impregnated the voids are filled with epoxy resin and the cable is fixated in this configuration.

5.4 Conclusion

Standard ITER type titanium barrels are used to perform virgin wire and extracted strand critical current measurements. Corrections for self-field are well understood enabling a fair comparison between cable sample and wire sample.

A second setup for testing cable samples is presented, the so-called U-shaped sample holder used in the cable test facility at the University of Twente. The sample preparation is faster and less material is needed than for FRESCA samples. The sample length is much shorter, but the test currents are higher. This setup is adapted to allow for the use of point heaters to probe the thermal stability of the sample.

The contact resistance between strands in FRESCA cable samples can be measured electrically. The contact resistance can then be split in average R_c and R_a values using CUDI. This is done for the samples tested in the FRESCA test station.

Chapter 6

Limitation of transport current due to self-field instability

Arguably, the most important figure of merit for any superconducting application is the critical current density the conductor can carry at the operational conditions. Only few Nb_3Sn cables have been tested extensively due to the relatively high cost involved. Often only extracted strands are tested before magnet construction starts. In this respect, the present study provides a unique comparison of several cables and thus allows observing common trends.

Cable quench currents are compared to witness strand results, in order to determine whether cable quench currents can be extrapolated reliably from witness strand performance.

6.1 Strand-to-cable comparison

Severe quench current limitations below the critical surface often are the result of magneto-thermal instabilities in the wire, as discussed in section 1.4.1. Flux-jump instabilities can be avoided by reducing the filament size, which is properly implemented in the design of any

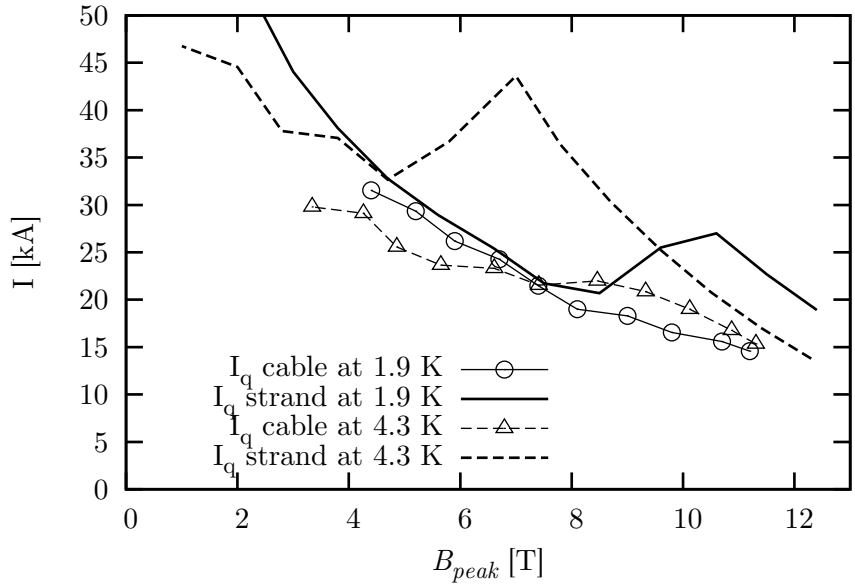

Figure 6.1: Measured quench currents versus peak magnetic field of sample F. The symbols denote the average value of the quench current of the cable while the lines indicate the quench current of the strand multiplied by the number of strands in the cable.

modern Nb_3Sn wire. Self-field instabilities are more difficult to avoid, since they depend on the conductor heat treatment, which may affect its RRR value, and on the operational conditions that determine the engineering current density. The overall result is that at low applied magnetic field conductors quench at a much lower current than at a higher applied magnetic field. As a consequence, a local minimum in the $I_q(B)$ curve is observed.

Such local minima can be seen for example in the strand data shown in figure 6.1. Another notable feature here is that the cable largely follows the same quench curve as the strand at 1.9 K. The data show a close match between strand and cable quench currents below 8 tesla peak magnetic field, but at higher magnetic field values

where the strand recovers to the critical surface the cable continues to suffer from premature quenches. At 4.3 K the cable also tends to follow the same curve as the strand at low magnetic field.

In recent studies [38] it is convincingly shown for the first time that the disturbance spectrum can be directly linked to the magnetic field at which a conductor starts to quench prematurely. Sample E (not shown) follows the same trend as cable sample F in figure 6.1, i.e. its self-field stability improves at a higher magnetic field than the strand measurement. This indicates that the support of the cable samples on the FRESCA sample holder seems to result in a stronger disturbance spectrum than a properly wound single wire sample.

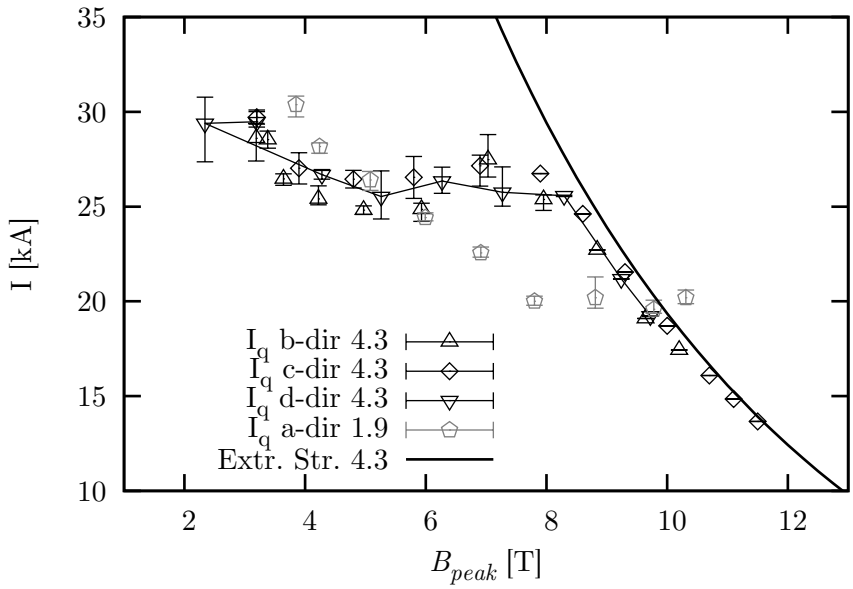

Figure 6.2: Quench currents versus peak magnetic field B_{peak} of sample G. The symbols denote the average value of the quench current and the "error" bars show the minimum and maximum values, the "d-dir" dataset has a line connecting the data points. Different symbols indicate different applied magnetic field directions.

6.2 Cable self-field limitation

The clear cut behavior of cable sample F is nice to demonstrate the principle effect, but most samples perform better. In order to quantify the impact of self-field instabilities on the cable performance a minimum quench current I_{low} and its corresponding magnetic field B_{low} are defined. The I_{low} represents the lowest quench current not on the critical surface and B_{low} represents the magnetic field at which it occurs. If the value of I_{low} falls below the expected nominal current of the magnet, self-field stability may compromise the magnet's performance. A conductor in a magnet system will experience all magnetic field levels from zero to peak magnetic field. This means that the lowest quench current has to be above the nominal current of the magnet design. In present-day high-J_c Nb_3Sn conductors this can still be an issue, see for a practical example references [57] and [91].

In figure 6.2 the results measured on sample G are shown. The cable is measured at 4.3 K in three different directions of applied magnetic field b, c, and d (see section 4.3, figures 4.8 and 4.10). After self-field correction, the three data sets follow the same pattern. The vertical "error" bars in the figure indicate the range of observed I_q values. At a peak magnetic field higher than 9 T, the cable follows the critical surface. In this high-field region, the maximum and minimum quench currents differ insignificantly (by less than 20 A at 20 kA). At magnetic fields lower than 9 tesla, the cable becomes unstable, the minimum and maximum quench currents start to differ significantly and the critical surface is no longer followed. For this cable, the value of I_{low} is 24.2 kA corresponding to a B_{low} of 5.9 T. Since the cable is designed to function at 12 T carrying approximately 12 kA, the margin between I and I_q is very large and the coil will be limited by I_c when prepared correctly.

When the cable is cooled down to 1.9 K, it becomes less stable. It does not reach the critical surface and between 5 and 10 tesla the cable performs even worse than at 4.3 K. The I_{low} decreases to

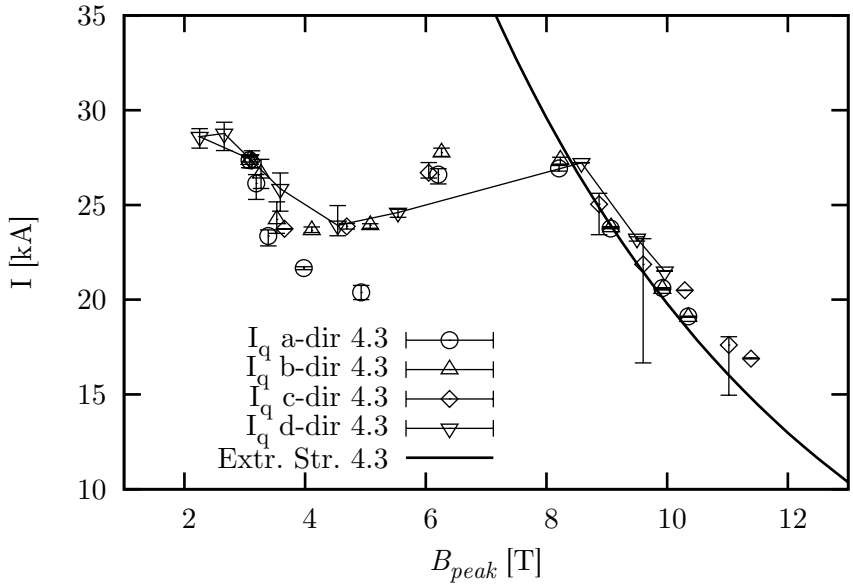

Figure 6.3: Quench currents versus peak magnetic field B_{peak} of sample D. The symbols denote the average value of the quench current and the "error" bars show the minimum and maximum values, the "d-dir" dataset has a line connecting the data points. Different symbols indicate different applied magnetic field directions.

19.8 kA at 7.8 T, which is however still above the expected operating current of 14.6 kA at 1.9 K [92].

The results for sample D are shown in figure 6.3. The conductor cross section of this cable is 74% larger than the previous sample G, but the critical current did not increase accordingly because this particular sample suffered from significant cabling degradation. Most likely due to this degradation, the sample did not show a clear transition as defined in section 4.4.1 making it impossible to extrapolate the I_c values. Above a peak magnetic field of 8 T the measured quench current does seem to follow the critical surface estimated from the extracted strand. This data is a strong indication that in this

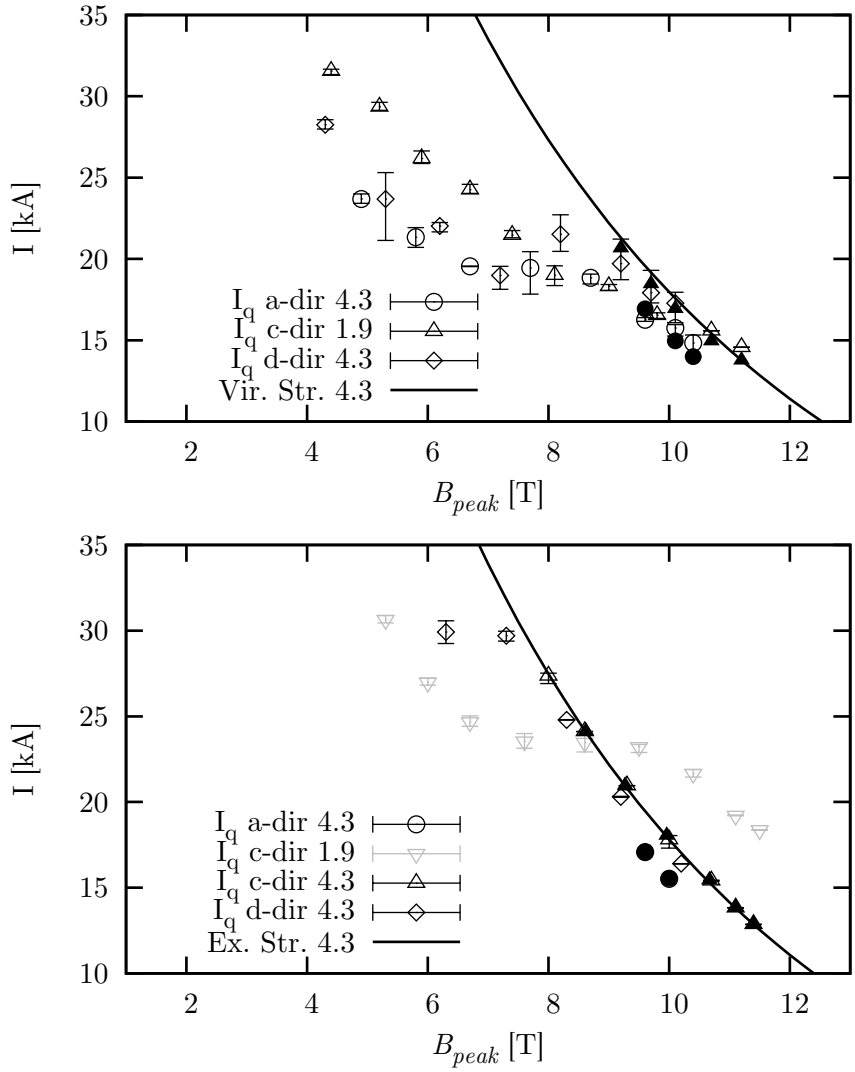

Figure 6.4: Quench currents and I_c versus peak magnetic field B_{peak} of samples F (top) and E (bottom). The open symbols denote the average value of the quench current and the "error" bars show the minimum and maximum values, the "d-dir" dataset has a line connecting the data points. The closed symbols show the evaluated I_c points. Different symbols indicate different applied magnetic field directions.

magnetic field region the sample is limited by its critical current and not instabilities. Taking this into account, an I_{low} value of 20 kA at a B_{low} of 4.9 T are found for this sample.

In figures 6.2 and 6.3, the data points for the anti-parallel "d-dir" applied magnetic field direction are connected with a line. The data points are plotted in order of increasing applied magnetic field value, so that for this particular orientation a small loop becomes clear at low peak magnetic field. The data sets converge when there is no applied magnetic field, as shown in section 4.4.1 figure 4.12. The anti-parallel configuration first rises in quench current since the self-field counteracts the applied magnetic field. Only when the applied magnetic field value exceeds the self-field, the quench current decreases below the I_q value obtained without applied field.

The next two data sets are obtained on two comparable cables from the LARP program. The wire and cable parameters are nearly identical, but there is a factor two difference in the sub-element size of the strands. The results are shown in figure 6.4. The I_c values of the witness strands from both cables are nearly identical. The variation in strand architecture results in a significant difference in quench current performance of the two cables at magnetic fields below 10 tesla.

Sample E clearly has I_{low} and B_{low} values of 17.8 kA and 7.7 T respectively, but sample F features much higher stability due to the smaller sub-elements. At 1.9 K sample F shows a local minimum, but at 4.3 K the current supply limit was reached before a clear minimum is found.

6.3 Conclusion

At relative low magnetic fields (less than 8 T), the self-field instability induced quench current of a cable corresponds to the measured quench current of witness strand. In contrast to the strand measurements, the self-field instabilities restrict the quench current of the

cable sample well below its critical surface up to higher magnetic fields. In accordance with reference [93], this is likely due to an increased disturbance spectrum of the cable sample.

In order to quantify the impact of self-field instability on the cable performance efficiently, a minimum quench current I_{low} may be defined. In four cable samples the I_{low} value is shown to surpass the critical current at 12 tesla. From a self-field stability point of view, these conductors are therefore all suited for their intended use in high-field magnets.

Chapter 7

Non-uniform cable properties

During the cabling process certain systematic deformations are introduced, and they may locally alter the strand properties. This leads to a statistical distribution of cable properties over the cable cross-sectional area.

Two effects can be probed by measurement. Firstly, it will be shown how the critical current density distribution can be derived from multiple critical current measurements performed in two directions of the magnet field. Secondly, RRR values measured in witness strands and cables can show small deviations which indicates that the current redistributes around poorly conducting sections in the cable cross section.

7.1 Critical current distribution in Rutherford cables

A Nb_3Sn Rutherford cable normally shows slightly degraded I_c performance when compared to its constituent wires (3-5%). This degradation is usually introduced at the thin and thick edges of the cables

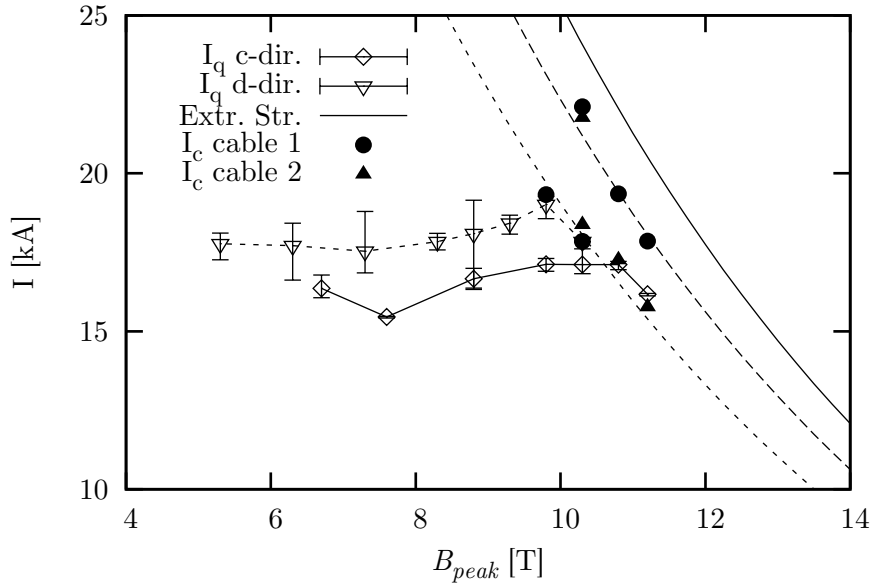

Figure 7.1: Quench and critical currents of sample B versus peak magnetic field B_{peak} at 4.3 K. The open symbols denote the average value of the quench current and the "error" bars show its minimum and maximum value. The closed symbols represent the evaluated I_c points.

[94] and causes the critical current to depend on the position of the peak magnetic field [82]. In the FRESCA test station the position of the peak magnetic field may be located at each of the 4 sides of the cable, depending on the orientation of the applied magnetic field, see figure 4.10.

This causes the data to depend on the direction of the applied magnetic field, even after self-field correction. For example, in figure 6.4, the critical current values measured in perpendicular applied magnetic field do not match those found in parallel magnetic field. The differences are caused by a shift in the position of the peak magnetic field in the sample cross section.

As a further illustration, the critical current values measured in the two legs of sample B are plotted and labeled differently in figure 7.1. There is a clear difference between the two legs of the sample. This cable suffered from significant degradation and the two legs clearly have a different critical current. Their critical current values fall 38% *or* 45% short of the values obtained on the virgin strand and the values switch from one leg to the other depending on the direction of the applied magnetic field.

Cable sample B is an experimental sample made to check whether cabling degradation can be reduced by limiting the number of strand cross-overs. This is tested by increasing the transposition pitch by a factor 2, while keeping all other cabling parameters constant. As a side effect the compaction factor is decreased to 79.4%. As discussed in section 2.1.2, a characteristic Nb_3Sn cable has a compaction factor of 85%, while an undeformed wire stacking results in a compaction factor of 78.5%, corresponding to a "circle in a box". Because of the low compaction the strands are free to self-arrange in an unequal distribution over the cable cross section. When such a cable is rolled, see figure 1.3, the pressure per strand is higher at the side with less wires. This results in more deformation and degradation in the strands at one side of the cable.

After the measurement, the cable sample was sliced and at nine positions cross sections were examined by microscope. A picture of such a slice is shown in figure 7.2, which may for reference be compared to figure 1.4. The latter image is obtained from cable sample C, which has the same width and thickness. The damaged filament clusters are counted in each cross section of cable sample B. In the less dense side of the cable 32 broken filament clusters are found, whereas only two were found at the denser side of the cable. This observation clearly confirms that the deformation is far from uniform.

In rectangular cables, degradation is normally expected to be symmetrically distributed since the wire deformation is symmetric. In key-stoned cables a minor difference between the thin and thick

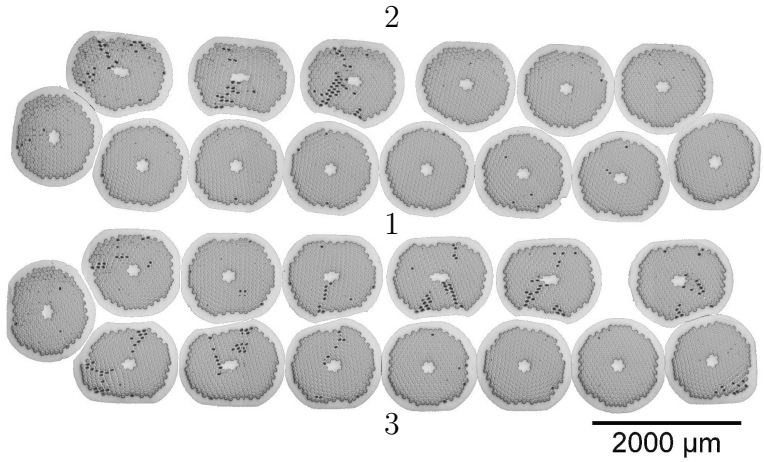

Figure 7.2: Cross section of sample B. Due to the very low compaction factor, there is one extra strand in the bottom layer compared to the top layer. The peak magnetic field in parallel applied magnetic field orientation is situated around position 1 while in the anti-parallel case it is found around positions 2 and 3, as shown in figure 4.10.

edges is expected, since there is a slight difference in compaction [6] and therefore also in likelihood of deformation. This implies that no difference in degradation is expected between the parallel and anti-parallel applied magnetic field configurations, but a slightly lower critical current is expected in perpendicular magnetic field. To test this hypothesis the procedure, described in reference [95] is used. It is assumed that the I_c value is determined by the conductor volume experiencing the peak magnetic field in the wire or strand in the cable. The peak magnetic field for each may be calculated with the algorithms described in section 4.5.

A simplified version of the critical current scaling law as described in section 2.2.1 is fitted to the data. The strain in the samples is assumed to be comparable. Furthermore, the data sets are measured over a limited range of applied magnetic field values, making it impossible to fit the parameters for the pinning force at low and high magnetic field. The scaling parameters p and q have therefore been

set to their default values of 0.5 and 2. This leaves the upper critical field at zero temperature B_{c20}, the critical temperature at zero magnetic field T_{c0} and the scaling constant C to be fitted. The assumptions above result in a simplified scaling law:

$$I_c(B,T) = \frac{C}{B}(1-t^{1.52})(1-t^2)b^{0.5}(1-b)^2 \quad [\mathrm{A}], \tag{7.1}$$

$$b = B/B^*_{c20}(1-t^{1.52}), \tag{7.2}$$

$$t = T/T_{c0}*. \tag{7.3}$$

The three remaining scaling law parameters are fitted to the extracted strand data while the cable results are fitted by only varying the scaling constant. The scaling factors for the cable are then normalized to the ones found for the witness strand. This is a convenient and objective method to determine the difference in critical current data at different magnetic fields.

Table 7.1: Percentage of extracted strand performance of the cable, calculated using the peak magnetic field.

Direction\Sample	**D**	**E**	**F**
Parallel	99%	101%	100%
Perpendicular	93%	88%	88%

With this method the results in table 7.1 are obtained. In the parallel magnetic field direction, when the peak magnetic field is situated in the least deformed part of the cable cross section, the performance matches that of the extracted strand nicely. In perpendicular magnetic field the cable performance is clearly worse, because it is limited by the $I_c(B)$ properties at the edge.

By comparing the results as a function of the peak magnetic field in the sample cross section, the intrinsic assumption is made that there is no current redistribution possible in the strand. If it assumed that the current can redistribute over the strand cross section, the peak magnetic field in the center of the strand has to be used. To

this end the I_c data of the strands and cables are all re-evaluated using the peak magnetic field selected from the magnetic field values in the center of the strands.

Table 7.2: Percentage of extracted strand performance calculated using the peak magnetic field in the center of the wire.

Direction\Sample	D	E	F
Parallel	100%	97%	100%
Perpendicular	97%	92%	92%

The results of this re-evaluation are shown in table 7.2. The difference between perpendicular and parallel magnetic field performance has decreased, but is still significant. The real values most likely fall somewhere in between those shown in tables 7.1 and 7.2, depending on the ability of the strand to sustain inter-filament current redistribution when operating in the vicinity of its critical surface.

The measurements show that there is indeed a systematic degradation of the critical current at the thin and thick edges of the cable samples, thus confirming the findings in reference [82]. It is fair to assume a 10% reduction of the critical current at the thin edge of the cable for this sample set. This corroborates the RRR findings, which are discussed in the next section.

7.2 RRR distribution in Rutherford cables

In cable samples A, C and F the RRR value of both extracted strands and cables are measured and the results are listed in table 7.3. In samples C and F the RRR value of the cable is significantly higher than of the extracted strand.

In Nb_3Sn Rutherford cables it is common to find higher strand deformations at the thin and thick edges of the cable than in the

Table 7.3: RRR values measured on extracted strand and cable.

Sample	RRR_{str}	RRR_{cab}
A	66-68	58-61
C	36-39	73-82
F	282-293	378-356

center, which leads to locally degraded critical current, as shown in the previous section. When this degradation is caused by filament damage, it is also likely that the copper stabilizer is contaminated with tin. Tin concentrations as low as 0.3% are known to result already in degraded RRR values [96]. Table 7.4 shows this effect at various locations along the extracted strands of cable sample H. The RRR value is degraded in the thin edge of the cable. This confirms earlier reports [97] and [98].

Table 7.4: RRR results of extracted strands in sample H, from table 8.1.

Position	RRR
Straight part	77-81
Thick edge	81
Thin edge	48

When a cable suffers from degraded RRR values along its thin edges, a higher RRR value is expected for the cable as a whole than for an extracted strand. In a single strand measurement, the current is forced through the degraded part of the matrix, while in a cable it can redistribute around the degraded sections following the path of least resistance, comprising better conducting sections lying in parallel.

When no local RRR data are available for the extracted strand, its degraded and unaffected values can still be estimated from the

overall cable and strand data based on a simple resistance model. Assuming that on average two strands at each edge of the cable are degraded, the factor normal-to-degraded matrix f_{n2d} will be approximately $(N_{str}-4)/(N_{str})$, with N_{str} the total number of strands in the cable. Assuming that in the cable the current can transfer directly without additional resistance, the measured resistivities of extracted strand and cable can be estimated from Ohm's law:

$$\rho_{str} = \rho_{deg} \cdot (1 - f_{n2d}) + \rho_{nor} \cdot f_{n2d} \quad [\Omega\mathrm{m}], \tag{7.4}$$

$$\rho_{cab} = 1/\left(\frac{1 - f_{n2d}}{\rho_{deg}} + \frac{f_{n2d}}{\rho_{nor}}\right) \quad [\Omega\mathrm{m}]. \tag{7.5}$$

Here ρ_{cab} and ρ_{str} are the cable and strand resistivities respectively, whereas ρ_{deg} and ρ_{nor} represent the degraded and normal resistivities. The resistivity of copper for varying values of RRR and temperature $\rho(RRR, T)$ can be estimated with equation 2.6. To calculate the expected RRR values of the cable and the strand, the resistivity at room temperature T_r is divided by the resistivity at T_c:

$$RRR_{str} = \frac{\rho(RRR_{deg}, T_r) \cdot (1/f_{n2d} - 1) + \rho(RRR_{nor}, T_r)}{\rho(RRR_{deg}, T_c) \cdot (1/f_{n2d} - 1) + \rho(RRR_{nor}, T_c) \cdot f_{n2d}}, \tag{7.6}$$

$$RRR_{cab} = \frac{1/\left(\frac{1-f_{n2d}}{\rho(RRR_{deg},T_r)} + \frac{f_{n2d}}{\rho(RRR_{nor},T_r}\right)}{1/\left(\frac{1-f_{n2d}}{\rho(RRR_{deg},T_c)} + \frac{f_{n2d}}{\rho(RRR_{nor},T_c)}\right)}. \tag{7.7}$$

Here RRR_{cab} and RRR_{str} are the measured cable and strand RRR values respectively, while RRR_{deg} and RRR_{nor} represent the degraded and normal RRR values to be determined. This set of equations has 3 parameters for two measured values. To determine the RRR values, the factor f_{n2d} is therefore fixed as $(N_{str} - 4)/(N_{str})$ so that the other two values can be solved.

The results of such analysis on cables C and F are shown in table 7.5. The estimated values are extreme but not implausible, showing that a RRR degradation at the thin edges of the cable can indeed affect the measured global RRR in the way seen in table 7.3. Two

Table 7.5: Estimated RRR values.

Sample	$\mathbf{RRR_{nor}}$	$\mathbf{RRR_{deg}}$
C	105	14
F	504	108

remarks are in order. Firstly, the values in table 7.5 are the RRR values used in the calculation. In measurements the resistivity just above T_c is compared to its value at 293.15 K, which would result in an RRR value of 410 for a strand with a matrix RRR value of 500. In this light, the values become even less extreme. Secondly, the degradation can occur in a single edge, as demonstrated by direct measurements on sample H, see table 7.4. In this case f_{n2d} is most likely less, most likely $(N_{str}-2)/(N_{str})$. If the degradation is uniform over the cable no significant difference is noted between a cable or extracted strand measurement, like in sample A.

In summary, the observations show that the matrix resistivity may vary over the width of the cable and can also be asymmetrical. These effects may have a strong impact on a cable's MQE value, as will be demonstrated in sections 8.1.1 and 8.1.2 of the next chapter.

7.3 Conclusion

For several of the investigated cables the critical current density is shown to be $\sim 10\%$ less in the edge than in the center. This confirms previous findings and corresponds to known locations of increased deformation and ensuing filament damage in the cable cross section.

The same holds for the RRR value. This may be observed directly in short sample measurements over straight and bent sections of an extracted strand. It is also shown that due to current redistribution the RRR values obtained on cable samples will in general be higher than those measured on extracted strands.

As will be confirmed in the next chapter, this implies that the edges of a Nb_3Sn Rutherford cable may have a significantly poorer thermal stability since the critical current, heat conductivity and electrical conductivity are all lower than in the center of the cable.

Chapter 8

Minimum Quench Energy, Measured and Calculated

The measured thermal stability of various Nb_3Sn cable samples are compared mutually and to model predictions. The collected dataset is unique in the number of cable samples and allows for a good insight in thermal stability of Nb_3Sn Rutherford cables. Since the choice of samples was dictated more by availability than by design, there is no purposeful difference in cable properties. Therefore, the results are grouped by the varied test parameters, which allows to focus on a given aspect of thermal stability rather then studying a single sample or a trend in the samples.

In the first section the experimental results are introduced and in the second section the outcomes of the models are compared to the measurements.

8.1 Minimum Quench Energy measurements

The results presented here were obtained with the quench heaters as described in section 4.1.4. Only fully evaluated values are plotted,

i.e. the data after the corrections for heat loss have been applied, see section 4.5.3. The results are bundled in three sections depending on which parameter was varied during the test.

Transport Current
: This relation is most commonly reported, since the sample current is a direct input in the stability theorems and thus may be straight forwardly compared to theoretical values and scaled directly.

Magnetic Field
: The magnetic field dependence of the MQE is the most interesting one from a magnet design perspective. In this case, the thermal stability is affected by the change in T_{cs} and T_c resulting from the variation in magnetic field.

Load Line Test ($B = C \cdot I$)
: The change in applied magnetic field is linearly coupled to the transport current in the sample. This simulates the operational conditions on the load line of a magnet, where the magnetic field acting within the windings is directly linked to the operating current.

Additionally, the bath temperature is changed between the tests. The temperature dependence is discussed for each of the three above categories in a subsection.

8.1.1 Transport current dependence

Making abstraction of experimental limitations, the thermal stability can in principle be studied in the current range from zero to I_c. Note that at the critical current, MQE is small but non-zero. When the current is reduced the stability increases, since both the length of the minimum propagating zone and the value of T_{cs} increase. As a result the MQE quickly increases over several orders of magnitude, so that the data are best interpreted on a logarithmic scale.

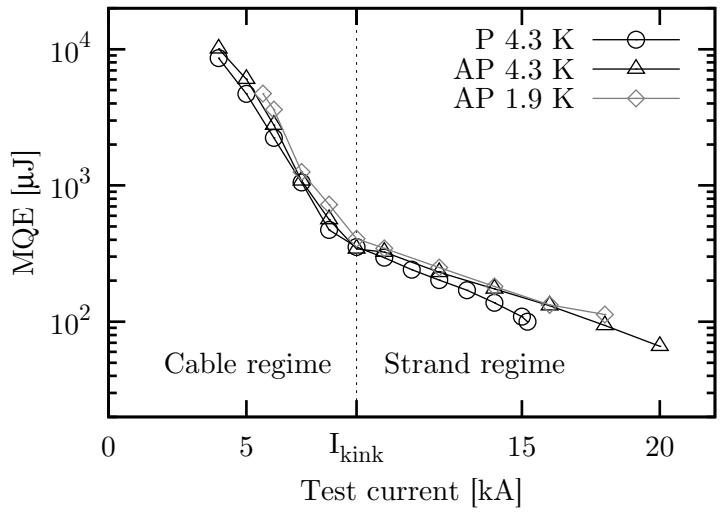

Figure 8.1: Minimum quench energy of sample E as a function of test current at 9 T magnetic field applied in parallel (P) and anti-parallel (AP) field.

A typical example is given in figure 8.1, where the thermal stability is determined at a fixed applied magnetic field of 9 tesla for varying test current and bath temperature. The three data series show approximately the same behavior, consisting of two slightly curved lines that intersect around 7 kA transport current. The resulting "kink" in the curve is associated to the transition from collective strands, or cable, to single strand behavior. The current at which the transition takes place is referred to as I_{kink}. At higher transport currents, the cable quenches completely as soon as a single strand reaches the normal state, while below I_{kink} the cable can sustain one or more normal strands for a short duration of time.

There is approximately 5 kA difference in I_c between the anti-parallel (19.8 kA) and parallel (14.9 kA) field directions, due to the large self-field as explained in section 4.3. In the center of the sample between the two cables, a self-field of approximately 0.1 T/kA

is generated. The heaters are placed on the outer surface of the sample, at a location where the deviation from the applied magnetic field is small (see figure 4.9). The fact that the two measurements barely deviate confirms a) that the influence of the self-field is small at the outer edge of the sample stack and b) that there is only a weak interaction between the two layers of strands in the cable. The data corresponding to the two applied magnetic field orientations only start to deviate significantly when the "P" measurement nearly reaches I_c.

These results illustrate how the thermal stability depends mostly on the local $I_c(B)$ value at the position of the disturbance and not on the I_c value of the entire cable. Because of this, the samples are studied in the anti-parallel magnetic field configuration, since the data obtained are almost the same, but the measurement range is greatly increased.

Influence of bath temperature

The bath temperature is varied between 1.9 K and 4.3 K. Figure 8.1 shows how the cool down to 1.9 K results in only a small increase in the thermal stability. This is to be expected since the current sharing temperature remains the same, so that only the extra enthalpy to heat the sample from 1.9 to 4.3 K is required compared to the 4.3 K data. Since the heat capacity increases with a linear and a cubic component of temperature, see equation 2.20, the enthalpy gain from the lower bath temperature is small compared to the enthalpy needed to heat the material from 4.3 K to the current sharing temperature T_{cs}.

For example, the energy needed to heat a cubic centimeter of equal volume ratio copper and Nb_3Sn from 1.9 to 4.3 K is 3.9 mJ, whereas the 4.3 to 6.7 K span (same 2.4 K difference) requires an enthalpy increase of 11.5 mJ. In addition, the heat conduction decreases when the temperature is reduced, further negating any stability gain from a reduced bath temperature. The change from 4.3 to 1.9 K in T_{bath} only marginally increases the value of I_{kink} in this case.

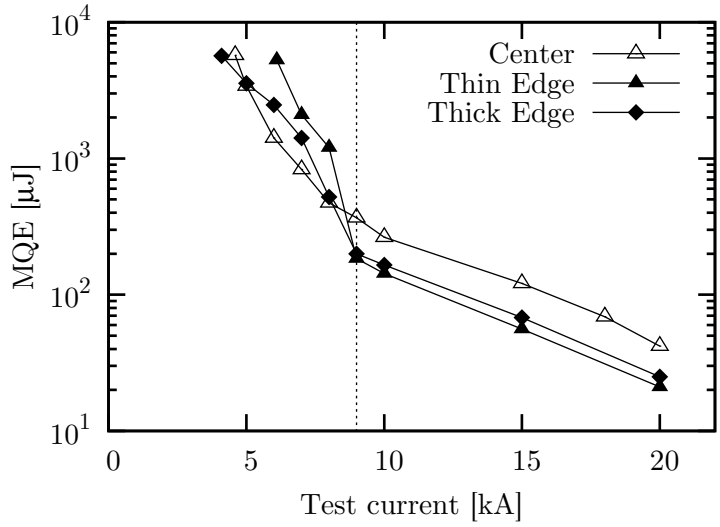

Figure 8.2: Minimum quench energy of sample E as a function of transport current at 9 T applied magnetic field. The results are obtained with point heaters on the same strand but at three different locations across the wide cable face.

Influence of heater location

The heaters are placed at the center and at the edges of the cable, as shown in figure 4.4. This way the two expected extreme values of MQE of the cable are found [47]. Figure 8.2 shows how in the single strand regime the thermal stability is roughly a factor 2 smaller at the edges of the cable than in its center. There is a small difference between the thin and the thick edge of the cable. The thick edge seems marginally more stable than the thin edge in the single strand regime, but less stable in the collective strand regime. The differences are small ($18 \pm 2\%$) and only marginally significant, as discussed in section 8.1.4. The strands are more deformed at the thin edge due to the higher compaction, leading to possible I_c degradation and reduced RRR due to tin poisoning of the copper. The slope of the MQE(I) curve in the collective strand regime is steeper at the edges

than in the center. The higher compaction ratio increases the thermal and electrical coupling between the strands, making the transition more pronounced. A more extreme case will be shown in section 8.1.2, where also a clear difference is observed between thin and thick edges.

Proof of collective strand regime

In order to support a single strand in its normal condition, the cable must be able to absorb the released thermal energy while maintaining the superconducting state in the remaining strands. At the same time, impregnated cables have a limited cooling to the helium bath and current densities in Nb_3Sn conductors are high. This might make the transition to the collective regime at appreciable transport currents seem implausible.

The voltage signals across the heated sample section are therefore analyzed to confirm that the kink in the curves 8.1 and 8.2 is due to a transition in the stability regime and not to some non-linear material property. Figures 8.3.b to 8.3.f show these voltages recorded over time for the MQE results in figure 8.1. For five test current values the U(t) curves are evaluated, corresponding to the closed symbols in figure 8.3.a. As discussed in section 4.4.2, during the MQE measurements the energy is repeatedly varied until the highest no-quench energy and the lowest quench energy differ by less than 5% from their mean. For each numbered measurement, the U(t) curves at the lowest quench energy (solid) and highest no-quench energy (dashed) are overlaid. The heater output is also plotted in gray to indicate the time of the perturbation. Except for the first case, the voltage line is a smoothed fit to the measurement. For reference, an unfiltered trace is plotted as gray dots in the graph.

The data in figure 8.3.b and figure 8.3.c are taken at higher transport current and thus lower temperature margin. There is no voltage build up visible at the highest no-quench energy. This implies that it is not possible for the cable to support a normal zone by redistributing current among the remaining superconducting strands.

In contrast, the graphs in figure 8.3.d show a clear voltage build

up even when the cable recovers. The graphs in figure 8.3.d and figure 8.3.e show a second regime where a single wire quenches and the graph in figure 8.3.f shows a third order recovery. In the last case, presumably the cable recovers when 3 strands have become normal, the central wire on which the heater is placed plus its two neighboring wires. In figure 8.3.e and figure 8.3.f the voltage signature of even higher order regimes may be seen during the quench. However, the cable is unable to recover from this disturbance.

Note that the time scale in the plots 8.3.b-f varies systematically. In figure 8.4 the collapsing normal zones, indicated by the arrow labeled "1" in figures 8.3.d-f, are compared in a single plot. The measured data is fitted with an exponential function of the form $U(t) = A \cdot (e^{-B \cdot t} - e^{-C \cdot t}) + D$. The parameters A to D are fitted using the data over the range of -2 to +3 ms from the start of the heat pulse. The offset determined in the parameter D is subtracted from all fits and measurement data in figure 8.4 to obtain a single base line.

The recovering normal zones are all marked by a comparable peak value of voltage. This approximately constant peak voltage indicates that the minimum propagating normal zone length increases with decreasing current. This confirms that an increase of minimum quench energy originates partly from an increase in the MPZ length and partly from the increase in enthalpy required to reach the current sharing temperature.

Also the recovery time remains constant at approximately 1 ms. This is characteristic for a system dominated by linear thermal conduction. Admittedly, the parameter space is limited and the fitted functions force an exponential decay, but when pool boiling is involved more non-linearities are expected due to transitions between boiling regimes (film and nucleate boiling) [99].

Full-size cable results

To complement the FRESCA data, a full-size cable sample H is tested on the U-shaped sample holder. The results are shown in figure 8.5.

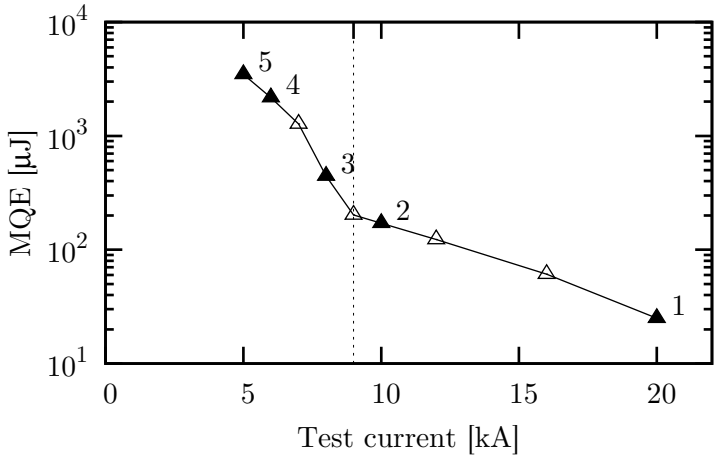

Figure 8.3.a: Minimum quench energy versus test current of sample E. For each of the labeled points 1-5, the evolution of the voltage with time is plotted in figure 8.3b to f.

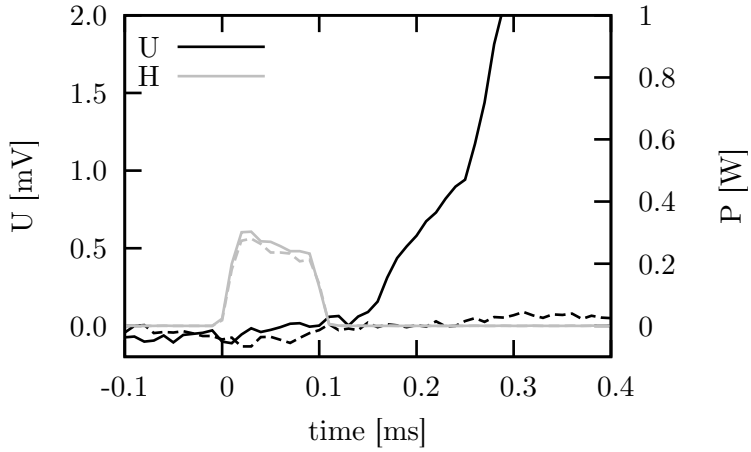

Figure 8.3.b: Sample voltage and heater power versus time for 20 kA test current. Continuous lines indicate the values found at the lowest quench energy and the dashed lines show the results corresponding to the highest no-quench energy. The input wave form is clearly distinguishable due to the short x-range of this plot.

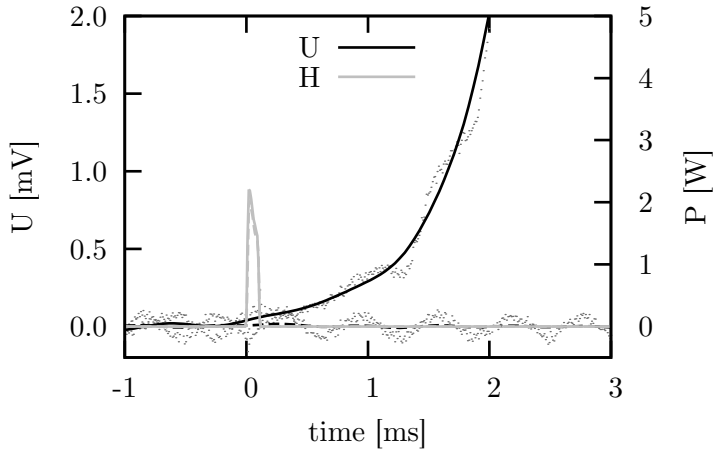

Figure 8.3.c: Sample voltage and heater power versus time for 10 kA test current. Continuous lines indicate the values found at the lowest quench energy and the dashed lines show the results from the highest no-quench energy. There is no significant voltage signal when there is no quench.

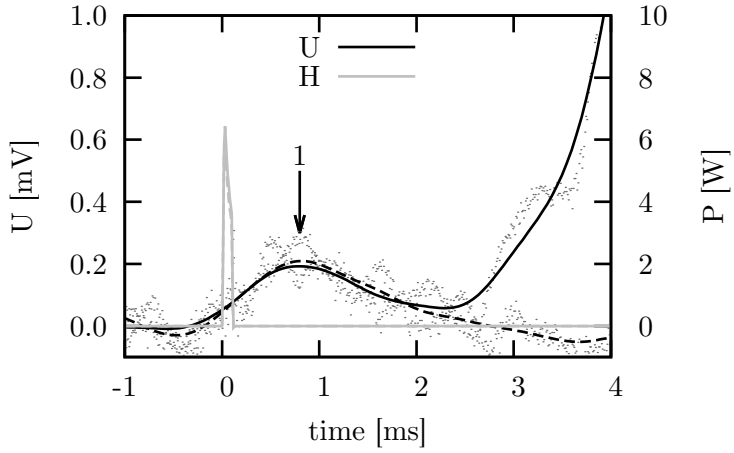

Figure 8.3.d: Sample voltage and heater power versus time for 8 kA test current. In this case there is a voltage signal even when the cable recovers. The transient normal zone in the cable reaches its largest extend at the time indicated by the arrow.

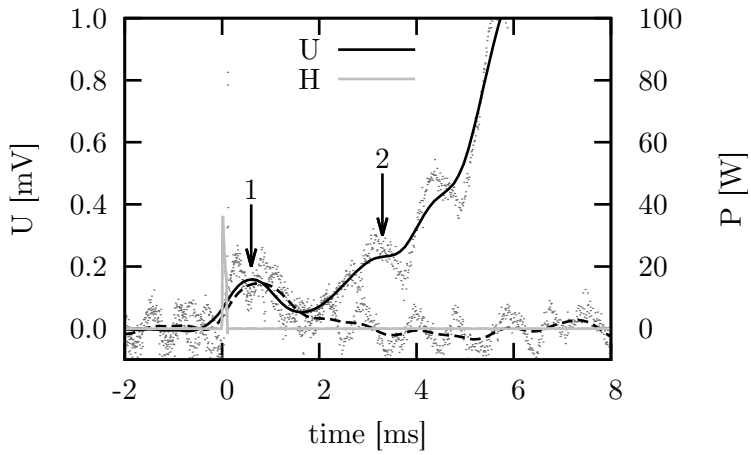

Figure 8.3.e: Sample voltage and heater power versus time for 6 kA test current. The transient normal zone in the cable reaches its largest extent at the time indicated by the arrow. During the quench, there is a second transition visible at arrow 2.

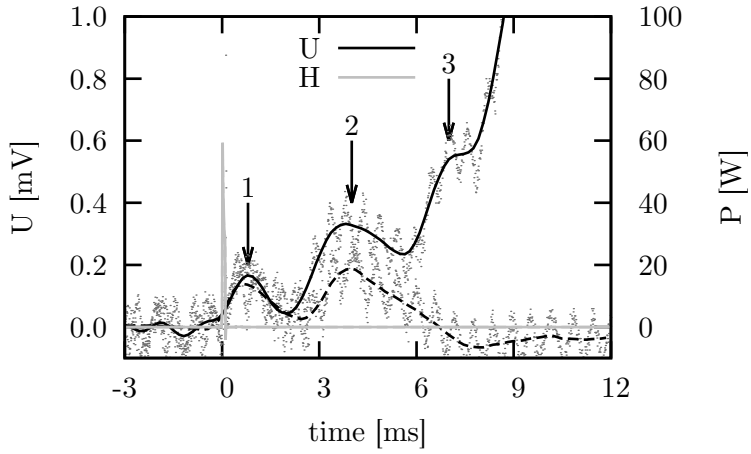

Figure 8.3.f: Sample voltage and heater power versus time 5 kA test current. The second transition at arrow 2 is now visible in the no-quench data, while a third transition appears during the quench.

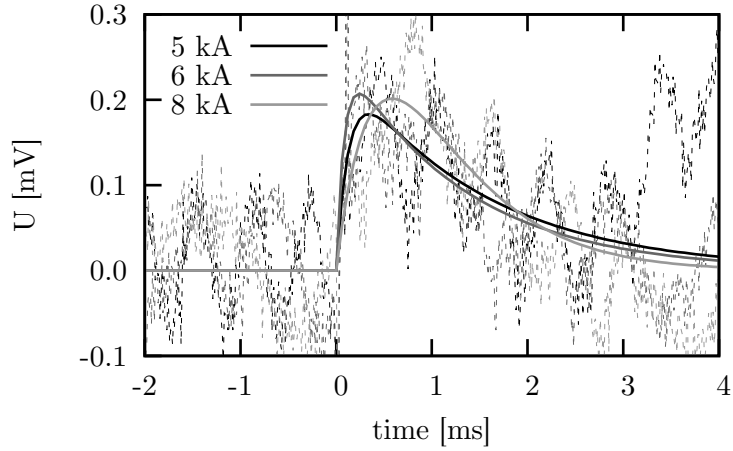

Figure 8.4: The sample voltage over time traces of the three no-quench cases shown in figure 8.3 overlaid on (thin dashed lines). A double exponential decay is fitted to the data (thick solid lines).

Only the data obtained with the center heater are shown, since in this test station heaters cannot be compared to one another due to the large difference in local magnetic field (0.12 T gradient over the cable per 1 kA, see section 4.5.1). In fact, the center heater is the only one that can be evaluated as a measurement in static magnetic field, since the self-field effect is negligible at this point. The edge heaters experience the self-field and cannot fairly be compared to FRESCA data where the test current has negligible effect on the local magnetic field. They are measured and are discussed in a later section.

The transition is less sharp than in previous measurements, but is nevertheless visible. The values of I_{kink} are accentuated with an arrow.

8.1.2 Magnetic field dependence

For a magnet design, the relationship between thermal stability and magnetic field at a constant current is more relevant than its dependence on the transport current. Note that a magnet has the same

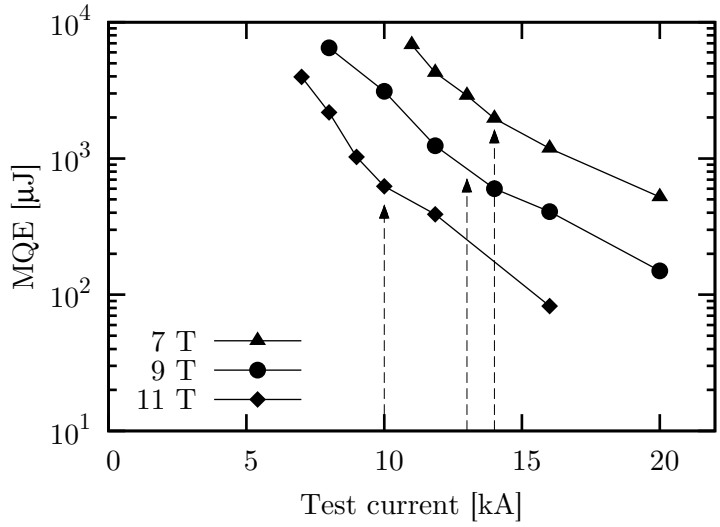

Figure 8.5: The minimum quench energy in the center of cable sample H as a function of the test current. Different symbols correspond to different applied magnetic fields. The arrows indicate the approximate location of the transition from collective to single strand behavior.

current in each turn, while the magnetic field varies from turn to turn from almost zero to the peak magnetic field. For a magnet operating at a stationary current, the MQE(B) curve is thus a direct measure for the stability in various locations throughout the cross section of the magnet.

For sample C, the magnetic field dependence of the MQE is measured at two transport currents 15 and 20 kA, see figure 8.6. The general trend in this figure is the same as in figures of MQE versus transport current: at low applied magnetic field there is a steep downward slope. At a certain magnetic field a sudden transition can be noted where the slope becomes less steep. The transition is again due to the change-over between stability regimes. The transition point is referred to as B_{kink} in this case. Below B_{kink}, MQE increases

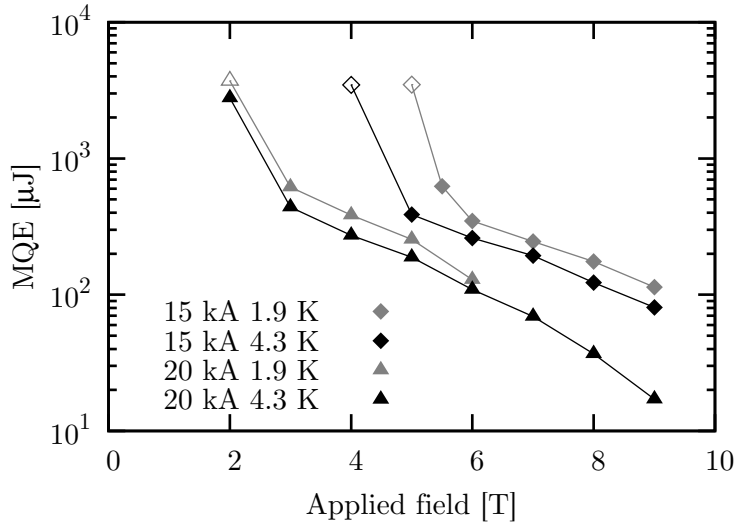

Figure 8.6: Minimum quench energy of sample C as a function of applied magnetic field at 15 (diamonds) and 20 kA (triangles) transport current and bath temperature of 1.9 (gray) and 4.3 K (black). The open symbols denote that only a maximum no-quench energy was measured.

rapidly above the maximal attainable heater energy output due to the transition to the collective strand regime.

Influence of bath temperature

When the bath temperature is reduced from 4.3 to 1.9 K, there is a small increase in the MQE values observed in the single strand regime while the value of B_{kink} shifts to higher magnetic field. This is unlike figure 8.1 where the I_{kink} is unaffected by the change in bath temperature. The sample is unstable at 1.9 K so that the 20 kA measurement could only be performed at magnetic field below 6 tesla.

When the current is reduced from 20 kA to 15 kA, the stability improves in two distinct ways. Firstly, in the single strand regime the enthalpy margin increases and secondly the B_{kink} shifts to a higher magnetic field.

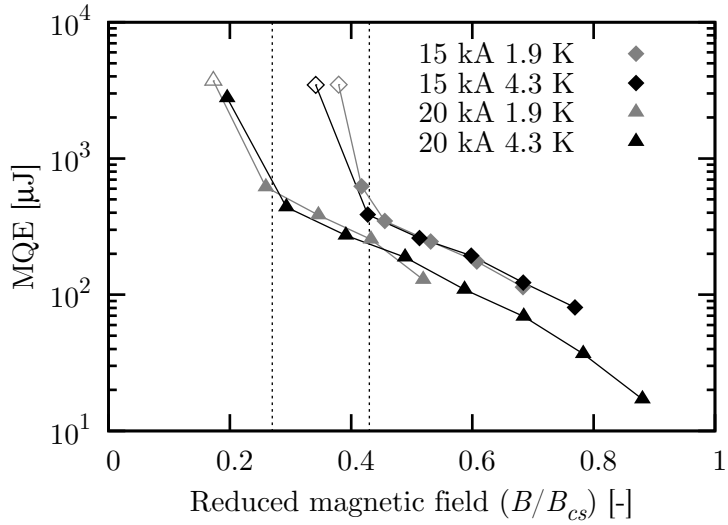

Figure 8.7: Minimum quench energy of sample C as a function of reduced magnetic field at 15 (diamonds) and 20 kA (triangles) transport current and at a bath temperature of 1.9 (gray) and 4.3 K (black). The open symbols denote that only a maximum no-quench energy was measured.

The 20 kA line is taken to test the thermal stability at low temperature margin, but the 15 kA line represents a more realistic operating current for the short model coil made from this cable. The load line for the real magnet is chosen conservatively and at the nominal field of 12 T the current is approximately 13.2 kA [23]. Therefore, the cable in the magnet is expected to be more stable than the diamond symbols in figure 8.6.

Scaling with the current sharing magnetic field

MQE measurements can conveniently be compared when plotted as function of the reduced current. This method is successfully used for Nb-Ti cables [44], [47]. Analog to this, a reduced magnetic field may be defined as $b \equiv B/B_{cs}$, the magnetic field divided by the current sharing magnetic field B_{cs}. This is the magnetic field at which the

critical current of the sample reduces to the transport current. When the measurements are compared at reduced magnetic field the data measured at different temperature collapse, as in figure 8.7. Note that by using this scaling the temperature dependence in b_{kink} also disappears.

It is not possible to compare the results from the two test current levels using b directly, since the current density is an important factor for the stability. Indeed, the dissipated power during a temperature excursion above T_{cs} increases with the square of the current density. This allows a cable to sustain longer normal zones for a longer time at lower current densities but constant b.

Figure 8.7 *seems* to indicate that a magnet operated at 1.9 K has the same stability as a magnet operated at 4.3 K, assuming that the magnet will be operated at the same fraction of B_{cs} at both temperatures. However, to reach this magnetic field level, a higher transport current is needed. In the data presented here there is no correction made for the increased transport current. This means that the stability over the cross section of a magnet is lower at 1.9 K than at 4.3 K. This will be further illustrated in the next section with a direct measurement.

Figure 8.7 also nicely shows how the use of more conductor can increase the stability of a magnet. The change from 20 kA to 15 kA can be interpreted as a 33% increase in conductor used in the magnet to improve stability. The effect in the single strand regime is significant but not impressive, but the B_{kink} value improves from 26% to 42% of B_{cs}. Consequently, a much larger fraction of the coil will fall in the higher stability regime during nominal operation.

Full-size cable

In figure 8.8 the MQE of cable sample H as a function of peak magnetic field is plotted. The open symbols show the thermal stability at 11.85 kA, the nominal operating current of the magnet for which this conductor is intended. The order of magnitude of the thermal stability is typical for similar impregnated sub-sized Nb_3Sn cables.

However, in these MQE$(B)|_{I_0}$ data, there is no clear transition from the single strand to the collective strands cable regime.

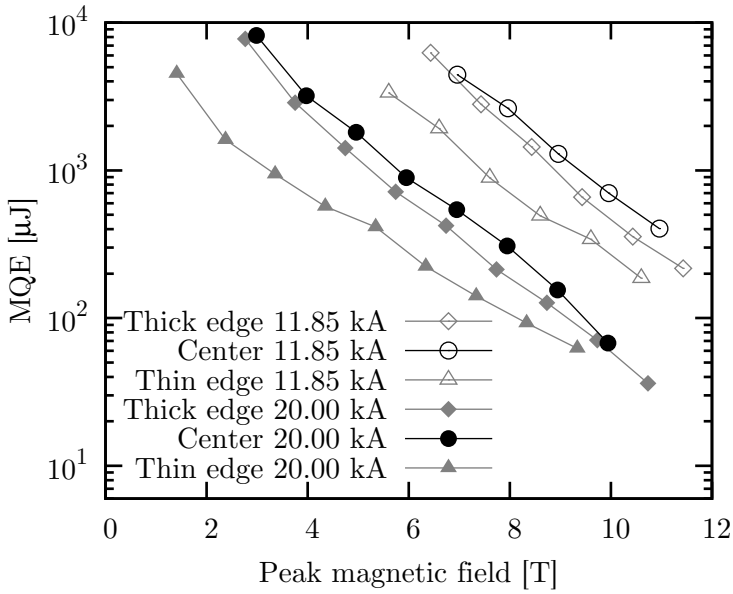

Figure 8.8: The minimum quench energy as a function of the local peak magnetic field of sample H. The open symbols are measurements taken at a test current of 11.85 kA and the closed symbols at a test current of 20.00 kA. Different symbols correspond to different locations of the quench heaters.

In figure 8.5 there is a transition at all magnetic field levels. From the previous MQE(I) data it can be deduced that at 11.85 kA test current there is a transition between 9 and 10 tesla applied magnetic field. However, in figure 8.8 the effect is so weak that it is not conclusive from the curve within reasonable error margin.

Figure 8.8 also shows how there is a difference of approximately a factor two between the measured MQE values in the center of the cable and those at the thin edge. Unlike the previous cables, there is also a large difference between the thick and the thin edges of the sample. The thick edge is only a slightly less stable than the center

of the cable. The reduced thermal stability presumably arises from an increased strand deformation in the edge of the cables, which is much stronger at the thin edge of the cable than at the thick edge. To test this hypothesis, the RRR value is measured on extracted strands taking samples from the straight sections and the "bends" at the edges.

Table 8.1: RRR results of sample H.

Location	RRR
Straight	77-81
Thick edge	81
Thin edge	48

The results are summarized in table 8.1. The RRR value in the thick edge sample is indeed comparable to the one observed in the center of the cable, while the thin edge shows a significantly reduced RRR value. Comparable results were already reported before [97], [98], but the present data illustrate the impact on thermal stability very clearly.

8.1.3 Load line dependence

From a thermal stability point of view, the most critical area of a magnet is the conductor section that experiences the highest magnetic field. The magnetic field and the transport current of this section are linked by the load line of the magnet. By good approximation, the local magnetic field can be calculated as $B(I) = C \cdot I$, with C as a magnet dependent constant.

In the FRESCA test station MQE measurements up to 9 T may be performed, but the cable samples are designed for 12 T magnets so only part of the envisioned load line can be covered. Since both test current and magnetic field are lowered simultaneously for these measurements, the quench energy quickly goes up beyond the measurable range, leaving only a small window where MQE can be tested.

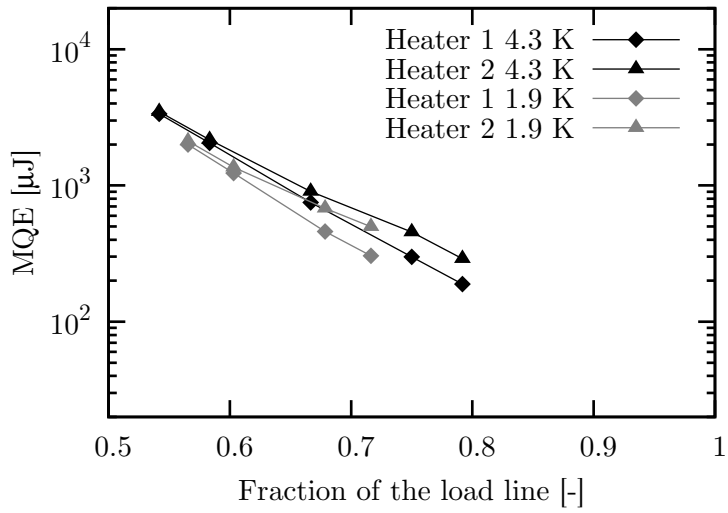

Figure 8.9: Minimum quench energy of cable sample G along the load line of the magnet for which it is intended. The data are measured for 4.3 (black) and 1.9 K (gray).

Figure 8.9 shows the MQE of sample G as function of coupled magnetic field and test current. The resulting plot is almost straight. The results at 1.9 K are lower, since the expected nominal current value and peak field are higher than at a 4.3 K operation temperature. The results of two heaters are shown since they show a significant difference. The two heaters are both placed in the center of the cable sample, however, there is a non-uniform current distribution in the sample, the nature of which is discussed in detail in section 8.1.4. This was reason to stop the measurement and no additional heaters are tested. Since these are the only direct load line measurements, the data are nevertheless shown here.

In correspondence with the result shown in figure 8.7, the thermal stability decreases when a magnet is designed and operated at 1.9 K. This is due to the small enthalpy gain combined with increased current density. However, a magnet designed to produce a

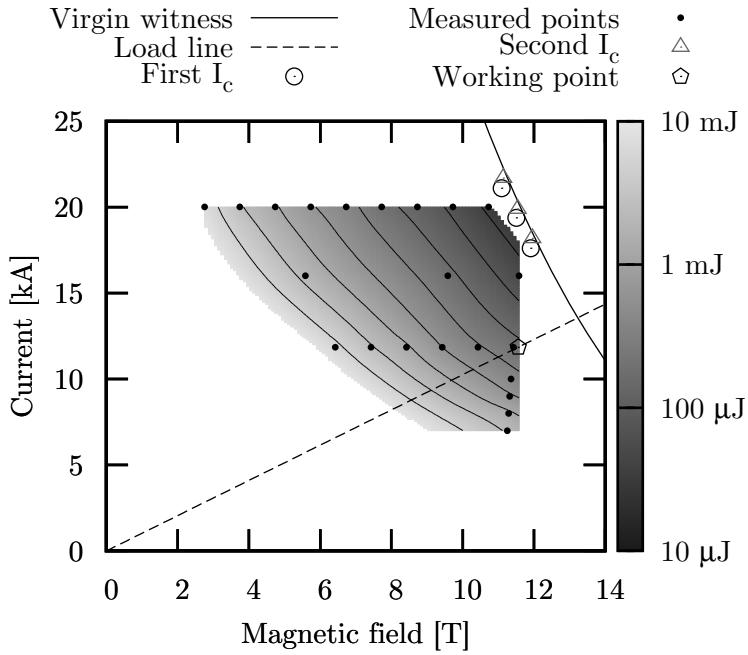

Figure 8.10: Density plot of the MQE at the thick edge heater as a function of the total magnetic field and test current. The data points are interpolated using a 2D spline algorithm to obtain a smooth surface. Contours with a factor 2 difference in energy between successive lines are added for clarity. The plot is superimposed on the $I_c(B)$ curve to give context.

certain bore field will always display better overall thermal stability when the nominal bath temperature is 4.2 K instead of superfluid helium. Since impregnated conductors do not benefit from the superfluid properties of the helium, the only reason to cool the magnet down is to save on conductor costs.

MQE map

For the full-size dipole cable sample H, the thermal stability along the load line is not directly measured but by combining the available

data sets shown in figures 8.5 and 8.8 and some additional strategically chosen measurement points, a "map" of the thermal stability is interpolated. The thus obtained 2D MQE(B, I) density plot is shown in figure 8.10. The magnet load line cuts the bottom right corner of the surface. A horizontal cut at 11.85 kA results in the nominal current line. The MQE values along this line can be seen directly in figure 8.8, represented by the open diamonds.

This map approaches the critical surface as close as it is possible within the accessible experimental window. Two complementary maps created with the same data treatment but using the results from the other two heater locations are shown in figures F.1 and F.2 in Appendix F.

These maps are interesting from a magnet design perspective, since they quantify how much the thermal stability increases when the nominal current is reduced. The nominal current might be reduced by using more turns in the coil, raising its thermal stability at the expense of a bulkier magnet and higher conductor cost. Such a design approach would bring the crossing point of the load line with the critical surface to a higher magnetic field value. The operating point would then effectively be at a lower percentage of the theoretical maximum. It is a well-known empirical observation that placing the working point of a magnet to a lower percentage of the load line helps to avoid training and other stability issues, but it is the first time that this can be quantitatively discussed in terms of measured thermal stability.

8.1.4 Reproducibility

To empirically determine an estimate of the uncertainty in the thermal stability measurements, the results obtained with different heaters are compared to each other. The thermal stability measurement is influenced by several factors:

1. local variation of surface contacts,
2. local variation of the RRR value,
3. local variation of I_c,

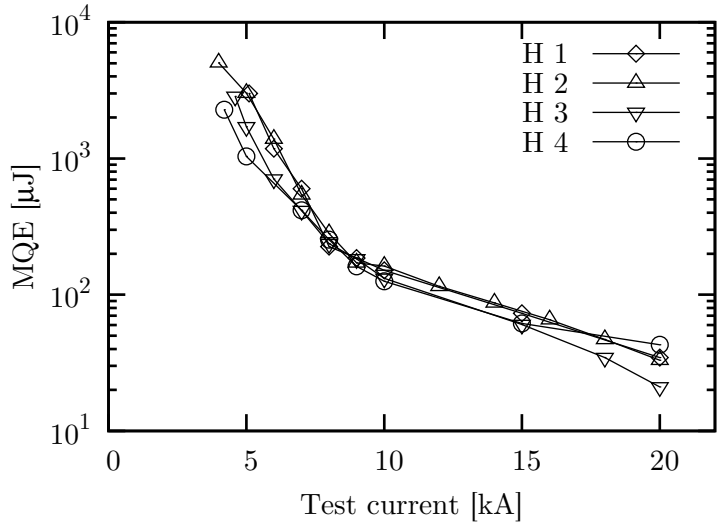

Figure 8.11: Minimum quench energy versus test current measured at 9 T and 4.3 K with 4 different heaters at the center of the cable.

4. heater efficiency,
5. current distribution over the strands at the joints.

The last two are an effect of sample preparation. To gauge the influence of these two issues, a sample is needed with a well-defined current distribution and a low variation in inter-strand contact resistances and material properties.

Sample E has four functional heaters in the center of the cable. It also reached the critical current expected from the extracted strand measurement. This implies that the sample has a uniform distribution. In addition, the current distribution is measured with Hall probes [100], showing less than 4% deviation in self-field along the cable. It is impossible to reconstruct the exact current distribution in the cable, however, an assumed current distribution can be fitted to the results. When a mean plus sinusoidal current distribution over the strands is fitted to the results, a difference smaller than 5% is obtained between the highest and lowest current per strand. Fur-

thermore, visual inspection revealed no obvious variation in contact surfaces between adjacent strands. Therefore, this sample should give a good indication of the characteristic distribution of heater efficiencies.

The same measurement is repeated with four heaters and the results are plotted in figure 8.11. On first sight the variation in the MQE values obtained seems small, but this is partly due to the logarithmic scale. A variation in heater efficiency is expected to result in a constant factor between the measurements. At high test current, above 15 kA, the measurements are strongly influenced by small changes in material properties at the heater. At low currents below I_{kink}, at less than 9 kA, the MQE curve varies from strand to strand. To estimate an upper limit of the variation of the heater efficiency, the results obtained from 9 to 15 kA are used.

The error of all values with respect to the average value of the MQE of their respective test current are calculated. The standard deviation of this is 9% of the average value. Changes of more than 20% are deemed significant with more than 95% confidence. For comparison, the method used to determine the MQE has an intrinsic uncertainty of 5%, see section 4.4.2.

Impact of a poor current distribution

As a counter example, sample G has an uncharacteristically poor current distribution, due to a preparation oversight. One of the strands was marked with ink to identify the strands after cabling. The cable was cleaned, but an ink residue inside the cable remained. During the heat treatment the ink decomposed, leaving a carbon-rich residue on several strands. This layer has poor bonding to solder, as shown in figure 8.12. The strongly uneven current distribution is most likely also the reason for the poor performance in terms of cable critical current compared to the extracted strand critical current.

Figure 8.13 shows preliminary MQE data for this cable, measured with two different center heaters. At high currents there is a factor 2 difference between the heaters that are tested. For this reason,

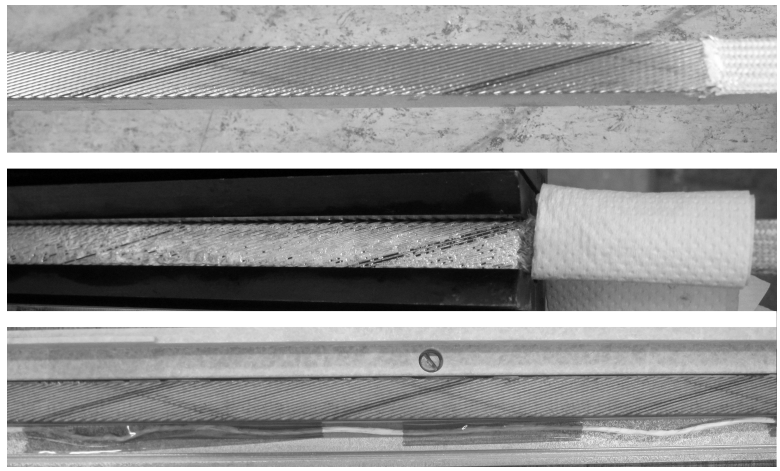

Figure 8.12: Sample G, from top to bottom; after heat treatment, after soldering and after impregnation. The blackened strands are poorly wetted by the solder.

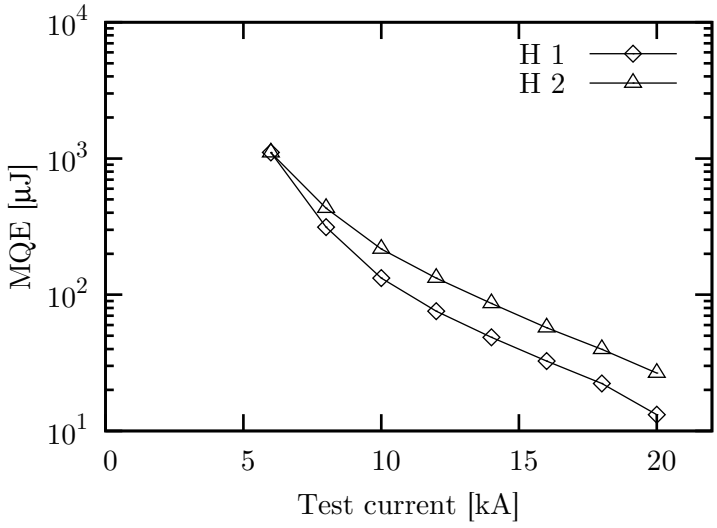

Figure 8.13: Minimum quench energy versus test current measured at 9 T and 4.3 K on sample G with 2 different center heaters.

further measurements were aborted, since the sample clearly does not represents a typical cable. However, these data clearly illustrate the influence of the current distribution and variable electrical contact on the stability of the sample.

Note that this is also the reason why this sample is excluded from table 7.1 and 7.2 in the previous chapter. The effects of the poor current distribution are also obvious in figure 6.2, in the sense that the cable does not reach the extracted strand performance.

At higher applied magnetic fields, the influence on the current carrying performance is not as strong, with only a 5% degradation versus the extracted strand. This might even be acceptable from a magnet design perspective, but the stability of the cable is decreased significantly, rendering it less usefull for the present study.

8.1.5 Distribution of the magnetic field in an accelerator magnet

To give an indication of the total gain in stability of a magnet system when the value of b_{kink} is increased, a statistical analysis of the magnetic field throughout the dipole section shown in figure 1.7 is made. The magnets are identical in performance and in the amount of conductor used, but one is a $\cos\theta$ design and the other a block design. They are evaluated in ROXIE, resulting in a magnetic field value for each strand in the cross section. A histogram with 50 bins is used over the full magnetic field range, resulting in the bar plot in figure 8.14. The highest population density is found approximately at 50% of the maximum magnetic field.

The cumulative distribution reconstructed from this histogram is a measure for the fraction of the coil found below any given value of the reduced field. This fraction is indicated by the lines in figure 8.14. The block and the $\cos\theta$ designs follow the same trend within 4%. Roughly 25% of the strands experience a magnetic field smaller than $B_{max}/3$, while another 25% are situated in a magnetic field larger than $2B_{max}/3$. So 50% of the strands are found between 0.33 and 0.66 reduced magnetic field.

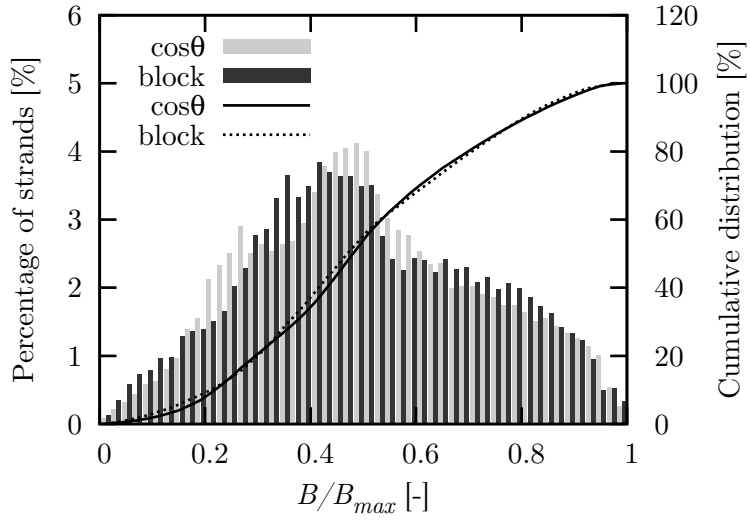

Figure 8.14: The bars are a histogram showing the distribution of strands found at each magnetic field range for cosθ and block designs. The total range of the magnetic field is subdivided by 50 bins, i.e. each contains 2% of the magnetic field range. The lines represent the cumulative sum of the histogram.

Combining these estimates with the b_{kink} values presented in figure 8.7 (0.45 for the design current), 43% of the strands in the coil benefit from the collective stability regime. The b_{kink} value falls right in the peak population density, implying that for relative small increases of conductor volume per magnet a considerably larger ratio of the coil will have an enhanced stability. This pleads for the use of more conductor to increase the stability of Nb_3Sn magnet systems.

As an example, consider a magnet operating at 4.2 K and 12 T, in which the number of strands per cable in the coil is increased by 10%, while maintaining the same number of turns and peak operating field and current. This can be approximated by a 10% increase in cable I_c. Using the Nb_3Sn scaling law, the increase of current sharing magnetic field can estimated to be $\sim 4\%$. According to the

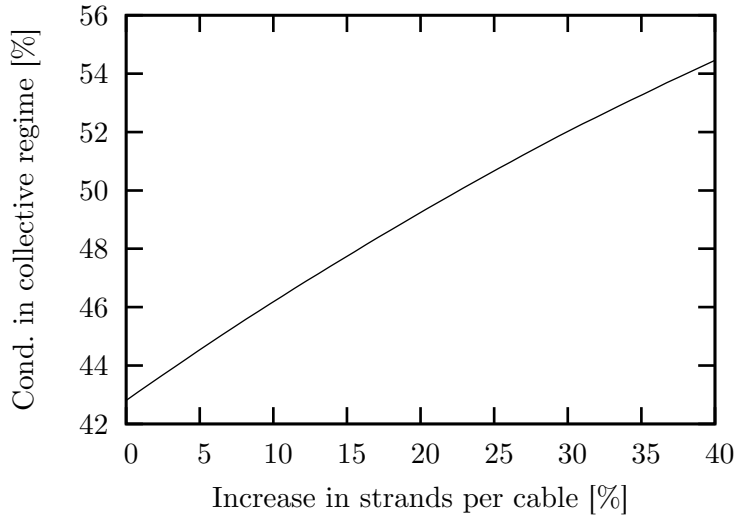

Figure 8.15: Fraction of the conductor in collective regime as a function of the increase of strands per cable. The increase in strands is calculated with a magnet operating at its critical current at 4.3 K and 12 T taken as reference.

findings in figure 8.7, the conductor fraction located in the collective strand regime would become 46%, a similar increase as the additional conductor costs.

To give a more comprehensive overview, this exercise is repeated for several values and shown in figure 8.15. The relative increase of the fraction of conductors in the collective regime is smaller than the relative rise in conductor volume. On top of this the strands in the single strand regime benefit from the reduced current densities. As a final remark, for large increases of conductor it is unlikely that the magnet design can remain similar, which is an important assumption in the calculation. The deviation from the calculated values depends on the re-design choices that are made and are therefore difficult to quantify.

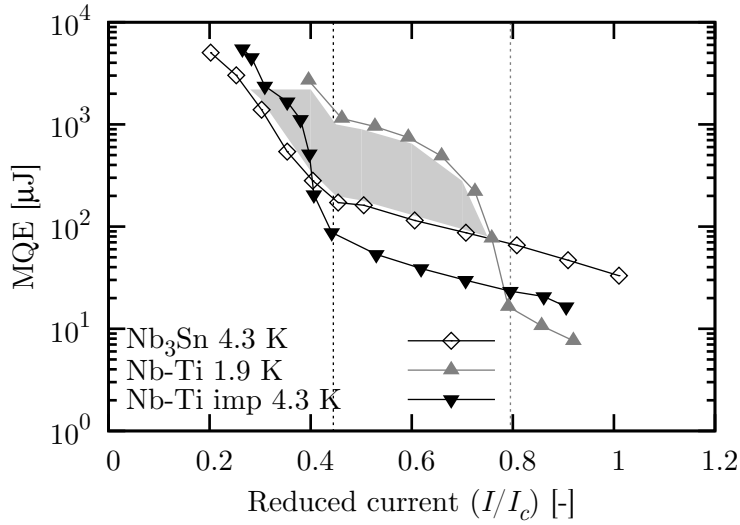

Figure 8.16: Minimum quench energy as a function of reduced current at 9 T and 4.3 K of Nb_3Sn sample E compared to two Nb-Ti measurements from [47]. Here a standard LHC dipole cable sample is measured at 9 T and 1.9 K while an impregnated sample of the same LHC cable is also measured at 6 T and 4.3 K.

8.1.6 Comparison to Nb-Ti Rutherford cables

The LHC main dipole magnets are built with Nb-Ti Rutherford cables, which are wetted by superfluid helium. These cables were extensively tested regarding stability, see reference [47]. Sample E is compared to a Nb-Ti LHC cable in figure 8.16. The so-called LHC 01 cable has 28 strands of 1.065 mm, with a f_{CnC} of 1.65 which is much higher than the 1.18 in Nb_3Sn cable Sample E.

Two measurements have been selected from [47], the first one is on a plain LHC 01 cable operated as intended (gray symbols), the second one is on a sample of the same cable but impregnated like a Nb_3Sn cable and characterized at 4.3 K. When operated in superfluid helium the Nb-Ti sample outperforms the Nb_3Sn sample over a large range (shaded area). This is due to the higher heat conductivity and heat

capacity of the helium inside the cable sample. These factors extend the collective cable stability up to a much higher reduced current of 0.8 than the value of 0.4 found for the impregnated Nb-Ti and Nb_3Sn cable samples. Even though it is currently not technically feasible to use superfluid helium wetted Nb_3Sn cables in accelerator magnets, it is interesting to quantify the increase in stability to illustrate the expected effect of better cooling of the windings in a magnet.

The two impregnated samples show similar trends, with a transition between collective and single strand regimes found at a comparable i_{kink} value. The single strand regimes have comparable slopes, the minimum propagation zone is expected to show the same quadratic current dependence. At 6 T the Nb-Ti cables has a critical current of 22.6 kA, which is comparable to 19.8 kA of the Nb_3Sn sample at 9 T. This implies that the currents per strand, but the current densities and joule heating are much lower in the Nb-Ti sample. The Nb_3Sn sample is nevertheless more stable, which is most likely due to its higher critical temperature and thus higher temperature margin.

As discussed in section 8.1.1, the voltage traces measured on Nb_3Sn cables show the onset of higher order stability, but this does not result in discontinuities in the MQE(i) curve. It is clearly visible in Nb-Ti sample.

8.1.7 Conclusion

The first thermal stability measurements on high-J_c Nb_3Sn Rutherford cables are reported. The thermal stability of two types of cables is measured. The following observations are the most striking ones:

- Just like Nb-Ti Rutherford cables, impregnated Nb_3Sn conductors can recover from a single quenched strand, when there is enough margin between bath temperature and current sharing temperature. In sample C this margin is obtained at a reduced magnetic field of 0.4. Observations in voltage traces imply that the recovery of at least two normal strands have been witnessed. Also the precursor of third order recovery is observed, but the recovery itself lies just outside the experimental window.

- At the edge of a cable the thermal stability in the single strand regime may be degraded, most likely due to degraded I_c and RRR values. However, the stability in the collective strand regime is unaffected, or even marginally better, presumably due to increased inter-strand contact.
- Reducing the bath temperature from 4.3 K to 1.9 K results in a marginal increase in thermal stability when magnetic field and transport current are kept constant. However, when the current and magnetic field are increased to utilize the enhanced conductor properties, the thermal stability decreases.
- Only the local I_c properties are relevant for stability.
- Depending on the design of the magnet, a small decrease in current density can yield a relative large gain in the fraction of the strands in a coil that is in the collective stability regime, and thus in the overall stability of the magnet system. So increasing the amount of conductor in a coil design will result in a larger fraction of windings that is capable of recovering from a single quenched strand.
- When expressed in reduced current, the transition point from collective to single strand stability regime occurs much sooner than in superfluid helium cooled Nb-Ti.

8.2 MQE calculations

The empirical data from the previous section are compared to the models described in chapter 3. Several key examples are highlighted and discussed, showing that there is some discrepancy between the models and the obtained stability curves.

8.2.1 Input parameters

Those cable properties that are used as input for the models and are readily available can be found in table 2.1. The precise value is in practice more difficult to obtain for several other model parameters.

For yet other parameters the variation over the cable is unknown. The impact of such variation is negligible close to the critical surface, since the normal zone remains small and the chances of variations are small. With increasing distance from the critical surface, the MPZ becomes larger and the volume of cable that is influenced by the disturbance also increases. This increases the likelihood of an impact from variations in the relevant properties.

The following parameters are not precisely known or have an unknown variance:

1. distribution of electrical contacts R_a and R_c,
2. thermal contacts between strands F_a and F_c ,
3. critical current data at higher temperatures,
4. variation of critical current,
5. RRR values,
6. detailed amount of external cooling.

The contact resistances R_a and R_c can only be measured on average in cable samples. Their values may fluctuate locally around the heater, with large changes in thermal stability as result. In a well-compacted cable R_a values will be sharply distributed, but R_c can vary from an open connection to a sintered copper contact.

The uncertainties in F_a and F_c are considerable, although the electrical resistance can be used to estimate the thermal conductivity assuming a sintered contact over a certain surface area. Nevertheless, exact values are unknown, and are assumed to be affected by the same variations also impacting R_a and R_c.

The critical current of the strands is well-known around the working point of the conductor. This can be used as starting point to extrapolate the performance at temperatures well above the bath temperature, but this leads to significant uncertainties. A typical example is that the strand performance at 4.3 and 1.9 K can be fitted equally well with a range of values of B_{c20} and T_{c0}, which would still result in accurate predictions for magnet design. However, at

elevated temperatures this leads to an increasingly diverging range of I_c estimates.

It is also known from RRR- and I_c measurements that a cable can have locally degraded superconducting properties due to the impact of the cabling process.

Together with a degraded I_c one often also observes a degraded RRR. This will have an impact when the normal zone propagates into such an area and starts to propagate at an accelerated pace.

Finally, the experimental setup is not perfectly adiabatic. There is a finite amount of cooling, which increasingly influences the results when the conductor is operated further and further from the critical surface.

8.2.2 CUDI

As discussed in section 3.1, CUDI is the most complex and complete model used in this work. Since it is a complete 3D thermal and electrical resistor grid model of a Rutherford cable, it is able to model the thermal stability over a wide range of operational parameters in terms of temperature, applied magnetic field and transport current. The model allows for an almost full freedom in the choice of physical properties and their distribution.

Comparison to fitted results

Sample C is tested over a relatively large range of magnetic field and test current at both 1.9 and 4.3 K, see figure 8.6. Also its superconducting properties, RRR value, contact resistances and geometric properties were empirically determined. The experimental stability data are compared to the CUDI model in figure 8.17.

Using the inter-strand thermal resistances F_a and F_c as free parameters, the model is fitted as closely to the measured data as possible. The model predicts roughly the same qualitative trends as observed in the measurement.

The single strand regime follows the same slope as the measurements. However, the absolute value of MQE is overestimated and the

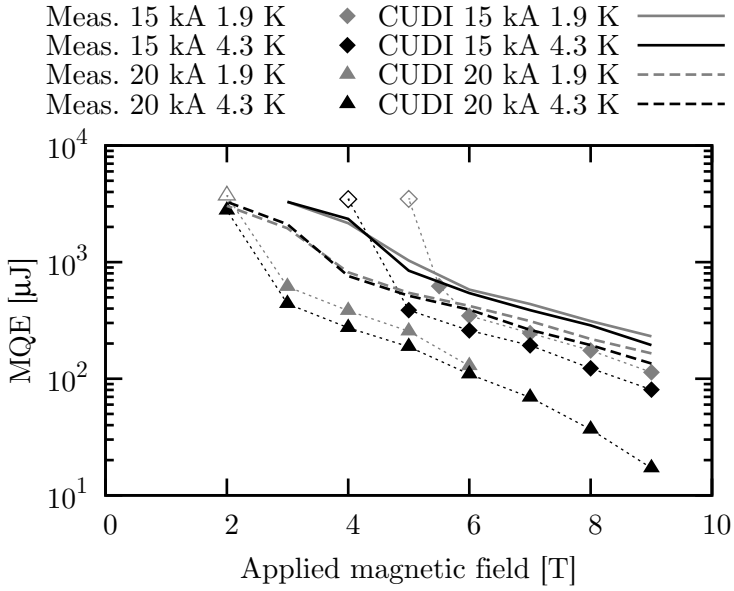

Figure 8.17: Measured minimum quench energy of sample C as a function of applied magnetic field at 1.9 and 4.3 K (symbols) compared to CUDI model predictions (lines).

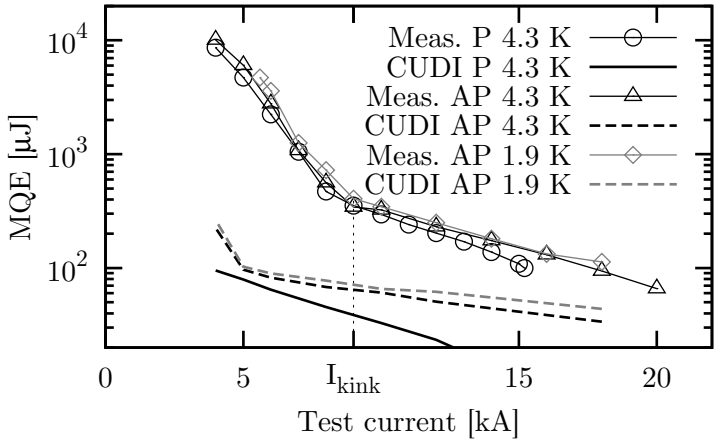

Figure 8.18: Measured minimum quench energy of sample E as a function of test current (symbols) compared to CUDI model predictions (lines). The data is obtained in parallel (P) and anti-parallel (AP) magnetic field configurations.

impact of the current density reduction is underestimated. Interestingly, the impact of temperature reduction is marginal in the simulations, whereas the measurements clearly show a small improvement in stability. Note that the model takes into account the expected enthalpy increase, which is quite small as discussed in section 8.1.1. Presumably, the measurements are affected by the helium II penetrating the heaters and giving rise to a small offset.

Especially at higher cable current, the transition to higher order stability is modelled to occur at a somewhat higher value of B_{kink}. The slope of the cable regime is less steep than measured. CUDI predicts that the MQE(B) slope becomes even less steep at lower magnetic fields. Unfortunately, this cannot be experimentally verified, since the energy densities in the point heaters become so high that they burn out.

To create a better match, the model would have to predict a lower stability of the single strand, while the higher order stability would need to be increased. Currently, there is no set of parameters which enables this in CUDI.

Predicting results

Due to the many unknown or distributed parameter values, the model has only limited predictive strength. This is illustrated even more clearly when the known cable parameters from sample E are fed into CUDI, and the unknown ones are scaled from the previous example.

The result is shown in figure 8.18. The modelled thermal stability is underestimated over the whole current range in this case. Also the slope of the single strand regime deviates from the measured data. The difference between the slope of the anti-parallel (AP) and the parallel (P) magnetic field simulations is much larger than measured. This implies that the thermal coupling between crossing strands is too strong in the model. In the anti-parallel simulation the strands are cooled too well, while in the parallel case the strands in the high magnetic field area receive more heat.

Finally, the current at which the transition occurs between the

regimes is underestimated in the simulation. In the anti-parallel case the transition seems to be completely absent.

8.2.3 StabCalc

The numeric code StabCalc, described in section 3.2, is fitted on the same MQE(B) data from sample C as with CUDI in the previous section.

The comparison between experimental data and model prediction is shown in figure 8.19. The single strand regime model results are similar to CUDI, which is unsurprising since both models use the same material properties and in the single strand regime current redistribution is minimal, so that the influence of the cable geometry is negligible. At lower applied magnetic field the effects of current and heat redistribution in the cable become more dominant and both models start to deviate from each other. Whereas CUDI shows the transition from single-strand to collective strand stability regime, StabCalc grossly underestimates the increase in stability due to the increase of thermal margin.

StabCalc is also applied to sample E, as show in figure 8.20. Since the model does not contain any 3D information, it cannot differentiate between the anti-parallel and parallel magnetic field cases, so that a single line is plotted using the magnetic field at the location of the heater.

As with cable C, the MQE(I) slope matches that of the experiment. However, also here the transition between the cable and single strand regimes is absent. This model thus seems unable to make any predictions about the collective stability behavior of Nb_3Sn conductors.

8.2.4 Analytical approximation

Using equation 3.12 the MQE values are calculated using the same input parameters and for the same data sets as with the numerical models. This is an estimate of single strand stability and therefore cannot be expected to show any stability enhancement due to current

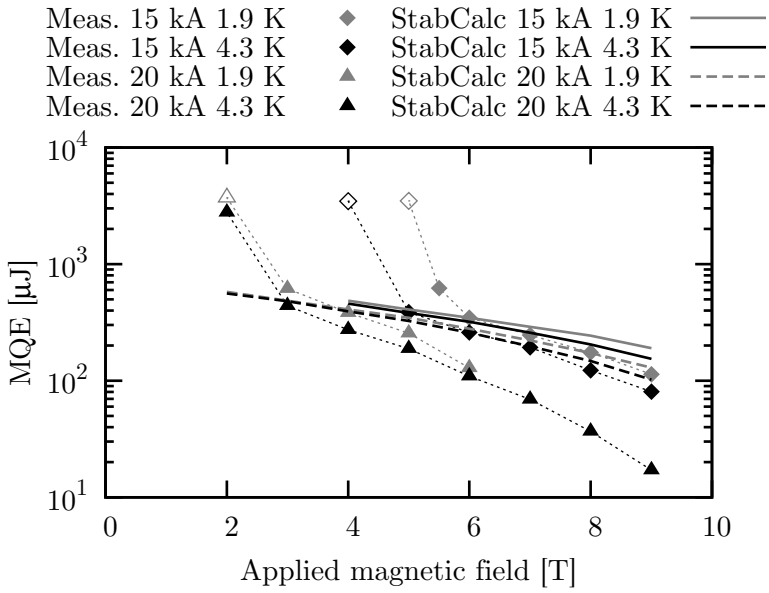

Figure 8.19: Measured minimum quench energy of sample C as a function of applied magnetic field at 1.9 and 4.3 K (symbols) compared to StabCalc model predictions (lines).

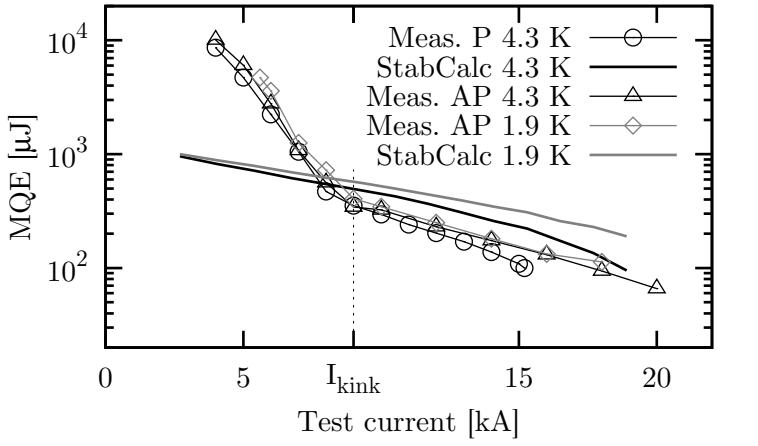

Figure 8.20: Measured minimum quench energy of sample E as a function of test current (symbols) compared to StabCalc model predictions (lines). The data is obtained in parallel (P) and anti-parallel (AP) magnetic field configurations.

sharing between strands.

Figure 8.21 shows how the analytical estimates are much less sensitive to the operational parameters as current and magnetic field than the measurements. The expression for the minimum propagation zone, equation 3.6, shows that a main variation can be expected from the increase of T_c. The change in thermal conductivity and electrical conductivity counteract each other and their effect is thus negligible in the range where the Wiedemann-Franz law holds.

As can be seen in figure 8.21, the strongest variation in estimated MQE values is due to current changes, since the MPZ scales inversely proportional with current density. At lower current densities the MPZ increases in size leading to a gain in the enthalpy needed to create such a normal zone.

These examples show that the analytical approach does provide the correct order of magnitude around the working point of the conductors. However, the increase in MQE by moving the operational conditions away from the critical surface is not correctly estimated. This is because even in the single strand regime, the neighboring strands absorb part of the heat injected in the excited strand. When the MPZ increases the length over which this transfer occurs increases as well, resulting in a larger heat sink. This effect is neglected in the analytical approximations, making them unfit to model the thermal stability of Nb_3Sn Rutherford cables with a large temperature margin.

8.2.5 Conclusion

The experimental data have been compared with several simulation models. None of the models fit the results with high accuracy over the entire measurement range. Impregnated Nb_3Sn cables miss a dominant stabilizing factor, like helium cooling in Nb-Ti conductors or a higher heat capacity such as in high-temperature superconductors. The conductors heat up relatively easily above the current sharing temperature with small heating power, but if the cooling exceeds the internal heat generation they quickly recover as well. Due to the

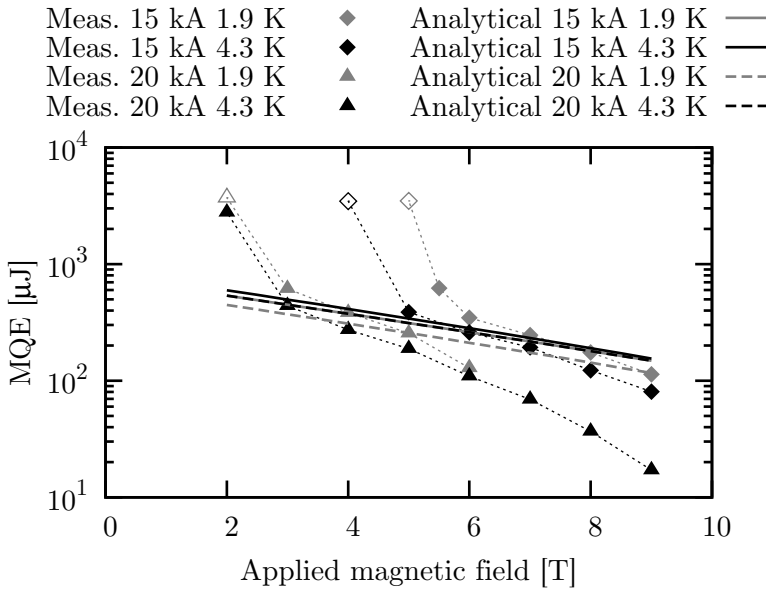

Figure 8.21: Measured minimum quench energy of sample C as a function of applied magnetic field at 1.9 and 4.3 K (symbols) compared to the analytical estimate (lines).

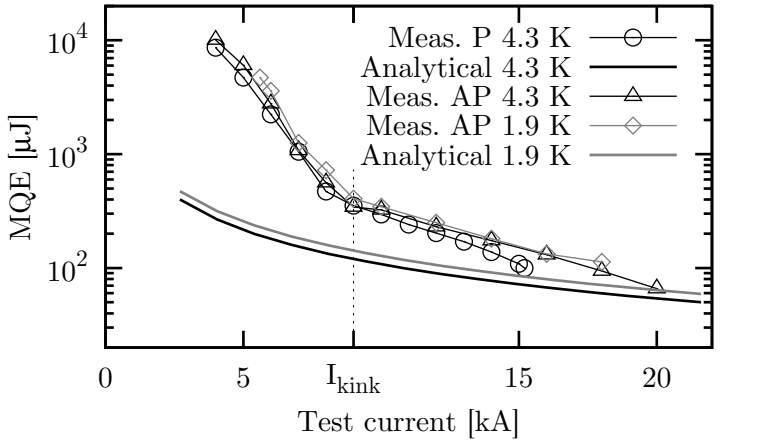

Figure 8.22: Measured minimum quench energy of sample E as a function of test current (symbols) compared to analytical estimate (lines). The data is obtained in parallel (P) and anti-parallel (AP) magnetic field configurations.

highly non-linear material properties and lack of a stabilizing factor, any small change in thermal or electrical conductivity results in large changes in temperature over time.

Aside from this global issue, several points stand out:

- There are several properties of Rutherford cables which are not directly measurable, but which are needed as input for a correct prediction of the thermal stability.
- Therefore, many parameters remain free to fit the models to the measurements. However, it is still not possible to obtain a good fit over a large range of magnetic fields and transport currents.
- Qualitatively CUDI performs best, since it does predict the transition between single strand and cable regimes. Furthermore, CUDI can be fit to match the order of magnitude of the MQE results and the slope of the single strand regime matches that of the data.
- The StabCalc model developed for this work can simulate single strand behavior with the same fidelity as CUDI, but it does not capture the transition between stability regimes.
- Analytical approximations for thermal stability are useful close to the critical surface, but become less accurate when the thermal margin from bath- to current sharing temperature increases.

Chapter 9

Conclusion

The aim of this work is to provide the first empirical quantification of the thermal stability of high critical current density (or high-J_c) Nb_3Sn Rutherford cables. To this end a dedicated experimental setup has been developed, as described in chapters 4 and 5. Several samples of high-J_c Nb_3Sn Rutherford cables are measured, resulting in a first overview of the thermal stability of these conductors, as discussed in chapter 8. Several other important and performance determining properties of this unique set of cable samples are evaluated in chapters 6 and 7.

In this conclusion chapter the main experimental observations are summarized, starting with the thermal stability in section 9.1. This section is divided in a general discussion, followed by observations on the characteristic transition point between the single strand and the collective strand (or cable) regime and finally a discussion of the benefits, or lack thereof, of operating at a lower temperature i.e. 1.9 K instead of 4.2 K. Then section 9.2 gives a summary of the modeling results.

Although only indirectly related to the main topic of the thesis, the experimental campaign also yielded a comprehensive dataset concerning other essential cable issues: like critical current variation, self-field stability and residual resistance ratio distribution. Obser-

vations thereof are summarized in section 9.3.

In the final discussion section 9.4, the main findings of this work are reflected upon in terms of their impact on magnet stability, the status of experimental and numerical know-how and the outlook for future research.

9.1 Thermal stability

Like other cabled superconductors where current-redistribution is possible, *Nb_3Sn Rutherford cables display two distinct regimes with respect to thermal stability.* At high currents or magnetic fields, the thermal margin is small and the cables are in the single strand regime where its minimum quench energy (MQE) values follow the same trend as those of isolated wires. When the thermal margin increases they enter the collective strands cable regime, where their thermal stability rapidly increases due to the possibility of current-redistribution among strands around the normal zone. This redistribution process requires a certain margin below the critical surface of the superconductor, as discussed in section 9.1.1.

The local $I_c(B)$ value of the strand at the position of the disturbance is more important than the critical current value of the cable as a whole. In section 8.1.1 it is shown that a large reduction in the critical current of the entire cable by means of a magnetic field gradient has only a marginal effect on the thermal stability, as long as the absolute magnetic field at the location of the initial disturbance remains constant. This confirms that *the MPZ does not extend far in these high-J_c conductors*, since only local material properties affect the thermal stability close to the critical surface.

As demonstrated in chapter 7, characteristic cables may show clear variations in local material properties, notably a suppressed RRR value and I_c degradation at the edges of the cable. All tested cable samples but one display a reduced MQE at both edges. One cable only showed such a reduced MQE value at its thin edge. Local

RRR measurements confirm that here the thin edge has a reduced RRR value. High-J_c *Nb_3Sn Rutherford cables commonly display a significantly lower MQE value at their edges* due to RRR and critical current degradation resulting from the cabling process.

9.1.1 Transition to collective strand behavior

At reduced currents or lower applied magnetic fields, epoxy resin impregnated Nb_3Sn Rutherford cables do display collective thermal stability behavior even though their cooling is very limited due to the cable impregnation. *The transition from the single strand to collective strands regime happens*, unsurprisingly, *at much lower ratios of the current and critical current* than in liquid helium wetted conductors. For all investigated cables this transition occurs at some 40% of the critical current when tested at 9 T applied field. For comparison, in commonly used NbTi Rutherford cables the stability regime is about 70% of the critical current. For one cable the test current is kept constant at 15 kA and the magnetic field was varied. This sample shows a transition at a magnetic field corresponding to some 40% of the magnetic field where the critical current of the cable equals the 15 kA test current.

In section 8.1.5 it is shown that these values of transition current and magnetic field imply that *roughly 40% of the conductor mass in a typical accelerator magnet operates in the collective strand regime* when the coil is operated close to its critical limit. The highest conductor population density experiences a magnetic field around transition from single strand to collective strand stability. Consequently, small increases in the amount of conductor used for a given magnet result in a relatively large increase in the conductor fraction that is in the collective regime.

In contrast to Nb-Ti, it is found that Nb_3Sn cables may transit to higher stability regimes without a clear discontinuity in the MQE curve. Instead, the transition between the single strand- and collective regime is marked by a change in slope. Transition between higher order collective regimes can be seen in the voltage signals, but

within the experimental window of this work there is no corresponding signature in the MQE(I) curves.

9.1.2 Impact of operating temperature

A Nb_3Sn magnet may be operated at 1.9 K to reach a higher magnetic field at higher current densities than at 4.3 K. However, the *MQE data show that there is no appreciable increase in thermal stability when the temperature is decreased.* Since heat capacity and conductivity are both reduced at lower temperature, there is not much to be gained from the increased temperature margin. This can be predicted from known material properties but it is now also shown empirically for these conductors. Due to the higher current density, the effective thermal stability in the magnet windings may even be reduced.

Another interesting temperature-related observation is that the thermal stability seems to be correlated with the current sharing magnetic field B_{cs}. Indeed, *MQE(B) curves measured at 1.9 K and 4.3 K may be scaled using a reduced magnetic field* B/B_{cs}. This observation makes it possible to predict the impact of a change in operational temperature on thermal stability simply on the basis of the known critical surface.

9.2 Modeling thermal stability

Three models of varying complexity are compared to the measured MQE curves. The most complex numerical model, CUDI, adapted for this work to include Nb_3Sn cable performance, is the only one able to predict the transition between stability regimes and the corresponding change in MQE versus current or magnetic field slopes. In this sense, it performs qualitatively very well, but so far it is less performing in predicting quantitative values for the transition current or magnetic field with the available input parameters.

The simpler finite difference model "StabCalc", developed for this work, fails to capture the transition and only describes the single

strand regime. The calculated MQE values in the single strand regime are comparable to the CUDI results, since the same values for the material properties are used. It has, however, limited quantitative predictive use.

A well-known analytical MQE expression generally used for single strands is shown to give a good estimate close to the critical surface. However, the increase in thermal stability when the temperature margin increases is predicted too weakly.

All material properties are highly non-linear in this temperature regime, which implies that small variations in their starting values or boundary conditions have a large impact on the thermal stability calculated with the numerical models. The large number of hidden or statistically distributed parameters in combination with the high numerical cost of the models, makes it unpractical to fit the measured results. Therefore, it is currently hard to conclude why *the models do not match the measurements well* because the correct parameter set is not found, or because they simplify the underlying physics too far.

9.3 Cable performance

The additional experiments performed in support of the thermal stability measurements confirm that the critical current of Nb_3Sn Rutherford cables can be locally degraded due to the cabling process. It is shown how such *local degradation may be effectively probed by changing the position of the peak magnetic field* over the cross section of the cabled conductor. Note that the weakest point of a cable is the limiting factor for its overall current carrying performance. This does not necessarily correspond to the most degraded part of the cable, since magnetic field gradients can locally decrease the $I_c(B)$ below the degraded value elsewhere in the cable. Putting this observation to use, the degradation can be measured as a function of the location of the peak magnetic field in the cable cross section.

RRR data obtained on cables commonly give over-estimated values. In cable samples the current flows around the low-RRR regions, that may originate from cabling damage. The observations corroborate previous findings that the RRR degradation takes place at the thin edges of the cable. Due to the low-resistance connections between the highly compacted strands, the normal current can bypass the degraded areas resulting in a lower observed RRR value.

As expected, the same self-field instabilities that limit current carrying performance of a single strand are shown to act also in the cable. *The minimum quench current behavior in the strand can thus be used to estimate worst case cable performance.* It is shown that the cable follows the same quench current curve as the strand, but normally remains unstable up to higher applied magnetic field values. However, the latter effect can be due to sample fixation and need not be an inherent cable property.

9.4 Discussion

The results in this thesis show how for state-of-the-art Nb_3Sn accelerator magnets, *the only directly available option to improve thermal stability is to use more superconductor* in the design. For this reason it is presently better to design a magnet to operate at pool boiling liquid helium temperature i.e. 4.2 to 4.5 K than at 1.9 K. This means accepting reduced J_e, which is costly. The need for epoxy resin impregnation and thus the lack of direct helium-II cooling hampers the development of more stable Nb_3Sn conductors. *Therefore, alternative cooling schemes are worth to develop.*

The energy needed to trigger a quench varies from 10 µJ to >10 mJ for Nb_3Sn cables. *To study the higher stability regimes in a cable in more detail, new heaters designs are required.* The size of the "point heaters" is ∼0.1 mm^3, so that even at low energy the energy density becomes prohibitively large. The current heater starts to degrade at energy densities higher than ∼0.2 J/mm^3. This effect in-

trinsically limits the experimental window that can be accessed with the present heaters. Higher stability regimes could be explored with larger heaters. Achieving the required response times with larger heaters or the required power densities with point heaters for stability measurements is an open engineering challenge.

The observed *scaling of stability with varying temperature using the current sharing magnetic field $B_{cs}(T)$ is a promising design tool*, but has limited use in accelerator magnets that are operated at constant temperature. However, it can be applied to estimate the impact of beam loss on the thermal stability in the coil windings close to the bore of an accelerator magnet. Also for systems cooled with supercritical helium and operating under large dynamic loads, e.g. fusion magnets, such scaling can be applied to predict thermal stability.

Due to the relatively low transverse pressure applied during the cable sample reaction in this study, there is a relatively poor electrical (and thermal) coupling between crossing strands in the measured samples. Thus *the cable samples measured most likely have comparable MQE values as cored cables.* When the same cables are used in a magnet, their R_c values will most likely be much lower resulting in different MQE values. The presented results with the current sample preparation method most likely underestimate the thermal stability for the anti-parallel field orientation. The parallel field measurements are likely to overestimate thermal stability because the heat and current redistributes into the high magnetic field area of the sample.

9.4.1 Models

None of the models perform very well, in terms of quantitative stability prediction. An analytical estimate indicates that the minimum propagation zone under magnet-relevant conditions is about 2 mm. This is close to the strand diameter of 1.25 mm, so *it is a valid question whether the strands can still be modeled straightforwardly as line elements.* On top of the small size of the MPZ, the magnetic field gradient in the sample can be up to 1 T/mm, so the material properties significantly vary across the strand as well. Therefore, a numerical

model can not exploit cylindrical symmetries to reduce the calculation load. However, in view of the steady progress in computational hardware, simulating multiple strands over the required lengths with internal structure may become numerically possible in the coming years.

9.4.2 Cable properties

The *RRR values measured on cables are more representative for quench propagation than those measured on extracted strands.* During a quench the current will redistribute over the cable cross section in the same way as in the cable RRR measurement. Using the RRR value obtained from extracted strands will thus over-estimate the initial internal heat generation. At higher temperatures, the difference in resistivity will diminish and so will the deviation between predictions based on cable or strand data.

It is shown that the possibility to vary the applied field direction in *the FRESCA test station can be used to determine which side of the broad face of the cable is most degraded.* By making a new sample holder in which cables can be oriented in any desired angle with respect to the test station dipole, a scan of the entire cable cross section could be made. This would show how far from the edges of the cable the degradation propagates.

Recent studies have indicated that the point at which the self-field instabilities start to become apparent depends on the background perturbation spectrum of a conductor. This might imply that the samples in the FRESCA test station sample holder require better fixation. Currently the samples are fixed with a transverse stress of ± 40 MPa. The stress is limited to this value to mitigate the risk of damaging of the cable samples, though the sample holder is capable of applying a higher stress. It is recommended to measure a series of cable samples at various transverse stress levels to confirm that this is the origin of the self-field stability related quenches.

Appendices

Appendix A

Thermal conduction of copper fitting parameters

For the thermal conductivity of copper reference [67] proposes an empirical relation which is correct within 10% from 1 K to above ambient temperature. This relation is:

$$k_{Cu}(RRR, T) = \frac{1}{W_0 + W_i + W_{i0}} \quad [\mathrm{W} \cdot \mathrm{m}^{-1} \cdot \mathrm{K}^{-1}], \tag{A.1}$$

$$\text{where } W_i = \frac{P_1 T^{P_2}}{1 + P_1 P_3 T^{P_2+P_4} \cdot \exp\left(-\left(\frac{P_5}{T}\right)^{P_6}\right)},$$

$$W_0 = \frac{0.634}{RRR \cdot T} \text{ and } W_{i0} = P_7 \frac{W_i \cdot W_0}{W_i + W_0}.$$

The fitting parameters P_1 to P_7 can be found in table A.1. When compared to the temperature data found in [65], there is less than 3% difference between this fit and the data over the relevant range (1 - 100 K). This correspondence is illustrated in figure A.1.

Table A.1: Fitting parameters used in equation A.1.

Constant	**Value**
P_1	$1.754 \cdot 10^{-8}$
P_2	2.763
P_3	1102
P_4	-0.165
P_5	70
P_6	1.756
P_7	$0.838/(2113/RRR)^{0.1661}$

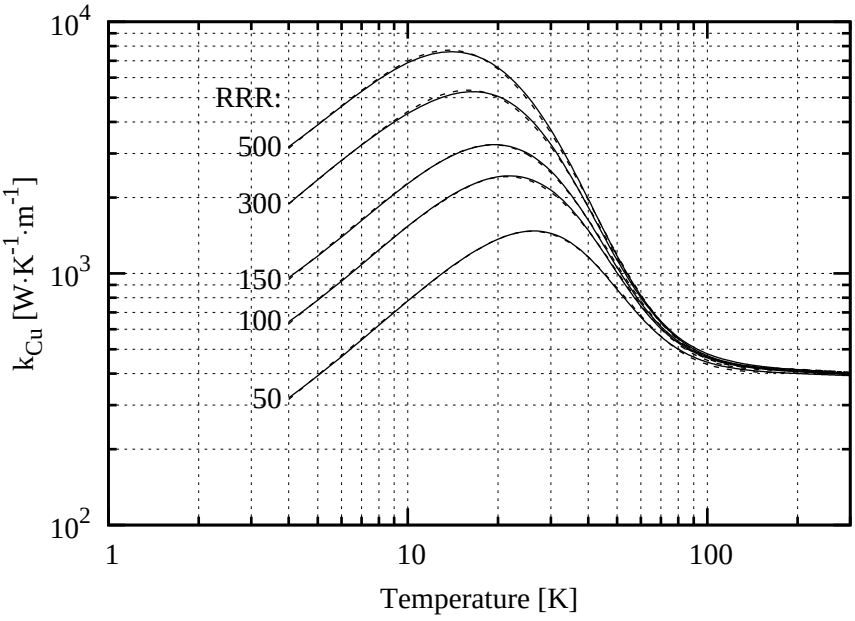

Figure A.1: Thermal conductivity of copper versus temperature. Continuous lines are data from [65] and the dashed lines are following equation A.1.

Appendix B

Fitting functions for $C_v(B,T)$ of Nb_3Sn

As shown in figure 2.7 in section 2.2.3, the heat capacity of superconductors differs from that of other materials by its strong dependence on the applied magnetic field. This appendix presents three possible methods to describe the relation between the C_v, B and T. The three methods are fitted to the data taken from [72], [73] and the results are discussed.

Theoretical $C_v(B,T)$ relation
If the relation between J_c and B is assumed linear, $C_v(T,B)$ can be calculated directly [79]:

$$C_v(T,B) = (\beta + 3\gamma/T_{c0}^2)T^3 + \gamma TB/B_{c20} \quad [\mathrm{J}\cdot\mathrm{K}^{-1}\cdot\mathrm{m}^{-3}]. \qquad \text{(B.1)}$$

Here T_{c0} is the critical temperature at zero magnetic field and B_{c20} is the upper critical magnetic field at zero temperature, while β and γ are fitting parameters. Note that this description involves two fitting parameters; γ and β, since B_{c20} and T_{c0} are known material properties. When fitted to the experimental data the following values are found:

Parameter	value
β	19.02
γ	1058

Although this model has the clear benefit of simplicity, it yields a rather poor fit to the experimental data. This is mainly because the model assumes a linear J_c dependence on B, while in reality this is closer to $1/B$.

Mixed polynomial exponential approach
Another approach is to find a suitable polynomial and exponential functions to determine the fitting parameters of the $C_v(T)$.

$$\begin{aligned} C_v(T,B) &= C_1(B)\cdot T + C_2(B)\cdot T^2 + C_3(B)\cdot T^3, \\ C_1(B) &= C_{1A} + C_{1B}B + C_{1C}B^2, \\ C_2(B) &= C_{2A} + C_{2B}\exp(C_{2C}B), \\ C_3(B) &= C_{3A} + C_{3B}B + C_{3C}B^2. \end{aligned} \tag{B.2}$$

First equation B.2 is fitted to the empirical data at various magnetic field levels. This empirical relation follows the data well, but it has nine parameters. The fitting parameter values are:

C	**1**	**2**	**3**
A	207	0	38.8
B	-3.83	-110	-1.80
C	2.86	-0.434	0.0634

Weighted average
According to [74], the heat capacity of both normal and superconducting materials can be described by:

$$C_v(T) = AT + BT^3 \quad [\mathrm{J}\cdot\mathrm{K}^{-1}\cdot\mathrm{m}^{-3}]. \tag{B.3}$$

The fitting parameters A and B change depending on the magnetic field or the state (normal or superconductive). As shown in [36], if

the fitting parameters are known for several discrete magnetic field values, they can be interpolated by a weighted average. For example when the required field value falls between B_1 and B_2 ($B_1 < B < B_2$), the C_v can be estimated at:

$$C_v(T,B) = C_v(T,B_2)\frac{B-B_1}{B_2-B_1} + C_v(T,B_1)\frac{B_2-B}{B_2-B_1} \quad [\mathrm{J}\cdot\mathrm{K}^{-1}\cdot\mathrm{m}^{-3}]. \tag{B.4}$$

This model has only four free parameters per calculated point, has a theoretical basis and shows good agreement to the data. It can also be used to fit the normal behavior of a superconductor. The fitting parameters are:

B_{app}(T)	A	B
Normal	1984	11.34
0	74.31	29.29
4	235.3	31.44
10	489.3	26.25
16	767.1	28.06

Note the large jump between normal and superconductive states, as compared to the change between the different levels of applied magnetic field.

Conclusion

All the presented fits have some advantage, but in this work the last fit will be used, since it has relatively few free parameters, is accurate at the measured points and readily allows a linear approximation in between.

Appendix C

Discretization of the 2D magneto-quasi-static approximation

In this appendix the finite difference equations are derived that need to be solved in order to model current flow in a 2D plane. Two of the four Maxwell's equations [101] are needed for the derivation. Firstly, Ampère's circuital law is taken:

$$\nabla \times \boldsymbol{B} = \mu_0 \boldsymbol{J} + \mu_0 \varepsilon_0 \frac{\partial \boldsymbol{E}}{\partial t}. \tag{C.1}$$

The $\partial \boldsymbol{E}/\partial t$ term describes electromagnetic waves either generated by current or influencing it. Because the currents used in the model are static compared to the magnetic field fluctuations of electromechanical waves, this term can be neglected. This is commonly referred to as a quasi-static approximation [77]. Using Ohm's law, equation C.1

can be rewritten to:

$$\nabla \times \boldsymbol{B} = \frac{\mu_0}{\boldsymbol{\rho}} \boldsymbol{E} \Rightarrow, \tag{C.2}$$

$$\frac{\boldsymbol{\rho}}{\mu_0} \nabla \times \boldsymbol{B} = \boldsymbol{E} \Rightarrow, \tag{C.3}$$

$$\nabla \times \left(\frac{\boldsymbol{\rho}}{\mu_0} \nabla \times \boldsymbol{B} \right) = \nabla \times \boldsymbol{E}. \tag{C.4}$$

The second Maxwell's equation used is Farraday's law of induction, with which the previous equation can be rewritten as:

$$\frac{\partial \boldsymbol{B}}{\partial t} - \nabla \times \left(\frac{\boldsymbol{\rho}}{\mu_0} \nabla \times \boldsymbol{B} \right) = 0. \tag{C.5}$$

This general case of the governing equation is simplified to 2D. Equation C.5 can be written out into all field components as such:

$$\begin{aligned} \frac{\partial B_x}{\partial t} + \frac{\partial B_y}{\partial t} + \frac{\partial B_z}{\partial t} - \nabla \times \Bigg(\frac{\boldsymbol{\rho}}{\mu_0} \Bigg[\hat{x} \left(\frac{\partial B_y}{\partial z} - \frac{\partial B_z}{\partial y} \right) \\ + \hat{y} \left(\frac{\partial B_z}{\partial x} - \frac{\partial B_x}{\partial z} \right) + \hat{z} \left(\frac{\partial B_x}{\partial y} - \frac{\partial B_y}{\partial x} \right) \Bigg] \Bigg) = 0. \end{aligned} \tag{C.6}$$

Here $\hat{x}$, $\hat{y}$ and $\hat{z}$ are the unit vectors in the x, y and z-direction, respectively. In the 2D approximation only the magnetic field in the z-direction is relevant since all other field components are zero. This leaves:

$$\frac{\partial B_z}{\partial t} - \nabla \times \left(\frac{\boldsymbol{\rho}}{\mu_0} \left[\hat{x} \left(-\frac{\partial B_z}{\partial y} \right) + \hat{y} \left(\frac{\partial B_z}{\partial x} \right) \right] \right) = 0. \tag{C.7}$$

Working out the next curl operator yields:

$$\frac{\partial B_z}{\partial t} = \nabla \times \left(\hat{y} \frac{\boldsymbol{\rho}}{\mu_0} \frac{\partial B_z}{\partial x} - \hat{x} \frac{\boldsymbol{\rho}}{\mu_0} \frac{\partial B_z}{\partial y} \right) \tag{C.8}$$

$$\frac{\partial B_z}{\partial t} = \frac{\partial}{\partial x} \left(\frac{\rho_y}{\mu_0} \frac{\partial B_z}{\partial x} \right) + \frac{\partial}{\partial y} \left(\frac{\rho_x}{\mu_0} \frac{\partial B_z}{\partial y} \right) \tag{C.9}$$

$$\frac{\partial B_z}{\partial t} = \frac{1}{\mu_0} \left(\rho_y \frac{\partial^2 B_z}{\partial x^2} + \frac{\partial \rho_y}{\partial x} \frac{\partial B_z}{\partial x} + \rho_x \frac{\partial^2 B_z}{\partial y^2} + \frac{\partial \rho_x}{\partial y} \frac{\partial B_z}{\partial y} \right). \tag{C.10}$$

Referring to figure 3.5 on page 63 for the naming convention, equation C.10 can be discretized using Δ_x and Δ_y as section length and wire diameter respectively. The differences are taken centrally around the calculation nodes:

$$\frac{dB_{z(i,l)}}{dy} = \frac{B_{z(i,l+1)} - B_{z(i,l-1)}}{2\Delta_y}, \tag{C.11}$$

$$\frac{dB_{z(i,l)}}{dx} = \frac{B_{z(i+1,l)} - B_{z(i-1,l)}}{2\Delta_x}, \tag{C.12}$$

$$\frac{d^2B_{z(i,l)}}{dy^2} = \frac{B_{z(i,l+1)} - 2B_{z(i,l)} + B_{z(i,l-1)}}{\Delta_y^2}, \tag{C.13}$$

$$\frac{d^2B_{z(i,l)}}{dx^2} = \frac{B_{z(i+1,l)} - 2B_{z(i,l)} + B_{z(i-1,l)}}{\Delta_x^2}. \tag{C.14}$$

Because the model uses a double grid, the calculation of the resistance values is non-trivial:

$$\rho_{x(i,l)} = \frac{\rho_{x(i,j)} + \rho_{x(i,j-1)}}{2} \tag{C.15}$$

$$\rho_{y(i,l)} = \frac{\rho_{y(i,j)} + \rho_{y(i,j-1)}}{2} \tag{C.16}$$

$$\frac{d\rho_{x(i,l)}}{dy} = \frac{\rho_{x(i,j)} - \rho_{x(i,j-1)}}{\Delta_y} \tag{C.17}$$

$$\frac{d\rho_{y(i,l)}}{dx} = \frac{\rho_{y(i+1,j)} - \rho_{y(i-1,j)} + \rho_{y(i+1,j-1)} - \rho_{y(i-1,j-1)}}{4\Delta_x}. \tag{C.18}$$

Equations C.15 and C.16 are linear interpolations of the resistance around the calculated point. Equation C.17 is the derivative and equation C.18 is a linear interpolation of the derivative of the resistance.

To couple the electrical and the thermal part of the model, the value of the current density in the thermal nodes is required, which is defined by equation 3.4, which is in turn discretized as:

$$J_x = \frac{1}{\mu_0}\frac{\partial B_z}{\partial y} \Rightarrow I_{x(i,j)} = \frac{A}{\mu_0}\frac{B_{z(i,l+1)} - B_{z(i,l)}}{\Delta_y}. \tag{C.19}$$

The discretization of the current between the strands in the y-direction is analog to this.

Appendix D

FRESCA magnetic field distribution and positioning of voltage taps

For critical current measurements, the length over which the measurement is performed needs to be known, since the criterion is defined as a voltage per conductor unit length. Secondly the absolute value of the applied magnetic field needs to be known over the measured length. If part of the conductor is exposed to a lower magnetic field, it will not contribute to the electrical field over the sample and the measured I_c value will be too high. In figure D.1 the field profile of the magnet over the length of the sample is shown, together with the location of the voltage taps. The location of the Nb_3Sn sample is indicated as well.

Since the set-up is not grounded, the voltage taps are always used in pairs because there is no absolute reference point. The voltage taps used in one pair are labeled with the same letter. A and B are used to measure the critical current and for this purpose they are placed within the area where the magnet provides less than 1% deviation from the peak magnetic field. Voltage taps C and D are mainly used to determine the quench location. Tap C is placed around the area

that still has relatively high field, but which does not contribute to the I_c measurement. D is a voltage tap placed on the bottom splice and on the current leads to detect quenches originating outside of the high field region. These quenches will subsequently be removed from the measurement results, or be labeled as such if they are included.

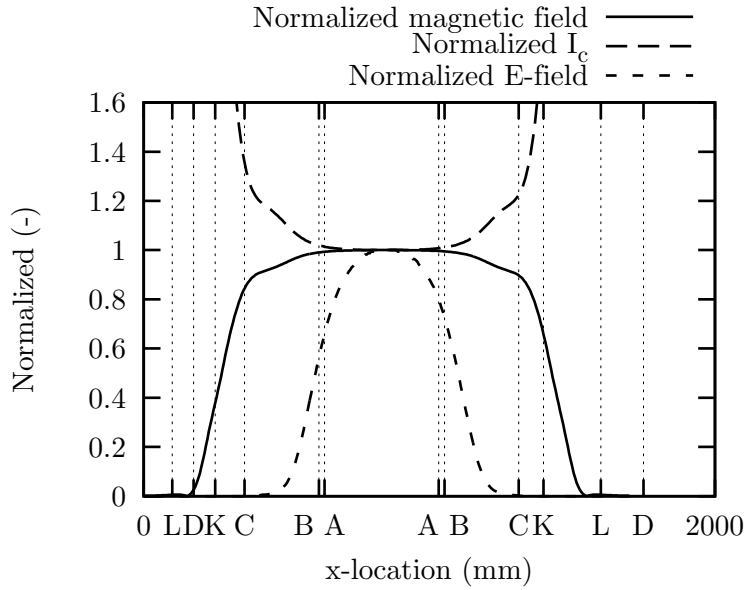

Figure D.1: Normalized magnetic field plotted from the bottom of the hairpin (x=0) along the sample length. The letters indicate key positions. L stands for the boundaries of the Nb_3Sn sample, K indicates the length of the sample between the joints and A-D denote the positions of the voltage tap pairs.

Since the magnetic field is known, the scaling law (equation 2.11 on page 43) can be used to calculate the expected variation of I_c over the sample. When the normalized critical current is known, the power law (equation 4.1 on page 84) can be used to estimate the potential drop over the sample as a function of the magnetic field. Both are calculated with characteristic values for B_{c20} (28 T), T_{c0} (17 K) and the n value (30). When plotted in figure D.1, this

hypothetical perfectly homogeneous material shows the influence of small changes in the magnetic field on the I_c measurement. The normalized E-field can be interpreted as a weighing factor for the I_c measurement over the length of the sample.

D.1 Voltage tap technology

As described in section 4.1.4, two systems were used over the course of the experiments. First, voltage tap strips and later a direct solder method were applied.

D.1.1 Voltage tap strips

The strips consist of a polyimide sheet 0.125 mm thick, 9 mm wide and 2150 mm long. There are 8 paths of copper running across the entire length of the strip on one side. On the other side there are several paths perpendicular to the length of the strip. The paths that are used for the measurement connect via a small hole in the tape from one side to the next. A top view can be seen in figure D.2. On both sides on the wide side of the sample a strip is placed. The face with the short perpendicular paths touches the sample. The paths connected to the quench detection have a redundant contact for added security. For the I_c measurements it is important to know the distance between the voltage taps, so single connection paths were used.

In past measurements on Nb-Ti cables, this method resulted in good electrical contact, since the cable was not electrically insulated. However, the Nb_3Sn samples are coated with a layer of glass fiber reinforced epoxy, which needs to be removed first. This results in a change of thickness of 0.1 mm of the cable, which needs to be compensated with additional layers of plain polyimide strips.

The contact strips run over the entire width of the cable and touch nearly half of the total number of strands in the cable. Nevertheless, it is important to note that only the voltage of the strand closest to

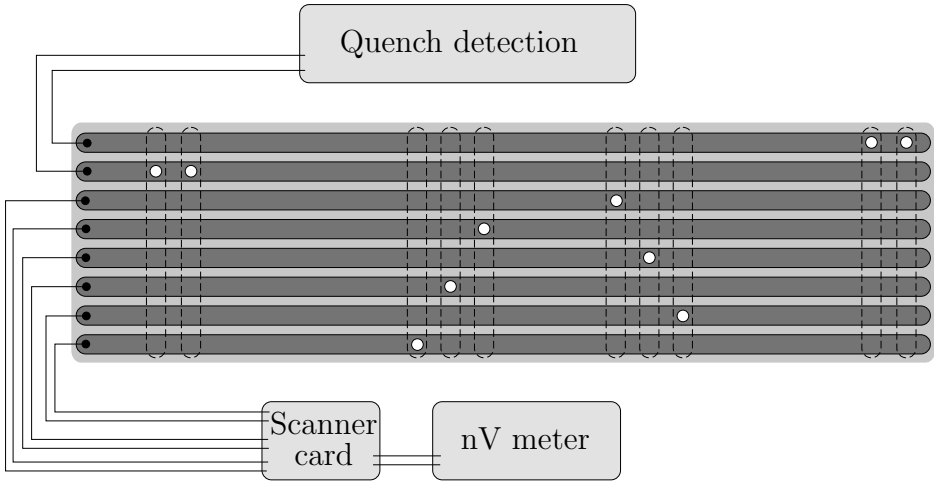

Figure D.2: Schematic view of the voltage tap strips and how they are connected to the measurement, not to scale.

the connection hole is measured. As an example; when one strand reaches I_c while the neighboring strand is still well below I_c, the first strand has a voltage drop of 10 µV/m while the second one has zero. The I_c measurement is done over approximately 0.5 meter, so the voltage difference between the strands is 5 µV. The copper path used on the voltage taps is 1 mm wide, 70 µm thick and the distance between the strands is approximately 1 mm. The resistivity of copper is around 1 nΩm depending on the purity. This results in a resistance of 14 µΩ. Therefore, the current that needs to flow through the contact path to completely negate any averaging effects of the copper on the potential is 0.35 A. This is a negligible amount of current compared to the transport currents in a Nb_3Sn wire, which ranges in several hundreds of amperes. Therefore, it is a correct assumption that the only voltage that is measured is the weighted average voltage of the two strands closest to the connection hole. The voltage of any other strand touching the voltage tap does not influence the potential measurement.

The realization of this effect, combined with the added sample

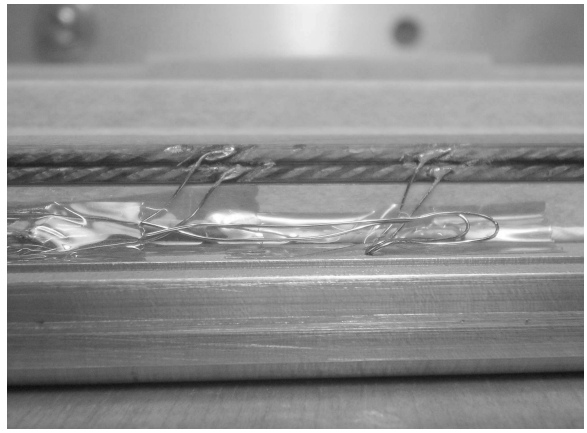

Figure D.3: Picture of a sample prepared with soldered voltage taps.

manipulations, resulted in the choice to use a less laborious approach to connect the voltage taps to the sample. The decision was made to leave the wide side of the cables intact and to solder the voltage taps directly to the strands on the thin edge of the cable.

D.1.2 Direct solder contacts

At the required location the electrical insulation is removed from the cables and a small copper wire is soldered to the exposed strand surface. This leaves the wide edge of the sample completely untouched, reducing the risk that the sample is damaged by transversal stress on the cable. An example can be seen in figure D.3. Since it is impossible to measure the average voltage over the cable (as argued in the previous paragraph) no accuracy is lost.

Appendix E

Numerical Self-field Calculation

For a fair comparison of the various measurements, the effects of the local self-field inside the samples has to be estimated. Since the geometry of the samples varies significantly, they have to be calculated with slightly different algorithms.

E.1 FRESCA sample

The calculation of a magnetic field in a cross section of a straight conductor is performed by dividing the surface into rectangular cells. The current is assumed to be concentrated in the center of each cell. These centers form an equidistant grid of points which are used in the calculations. To calculate the magnetic field generated by each point in the other points, the Biot-Savart law is used solved for an infinitely long wire:

$$\boldsymbol{B}(\boldsymbol{r}) = \frac{\mu_0 \boldsymbol{I} \times \hat{\boldsymbol{r}}}{2\pi r} \quad [\mathrm{T}], \tag{E.1}$$

where $\boldsymbol{B}$ is the resulting magnetic field for current $\boldsymbol{I}$ at distance r, with $\hat{\boldsymbol{r}}$ being the unit vector from the current to the point where

$\boldsymbol{B}$ is calculated ($\boldsymbol{r} = r \cdot \hat{\boldsymbol{r}}$). The grid is m elements wide and n elements thick, where m and n are chosen such that the spacing between the grid points is approximately equal in both directions. Both cables have a different grid to allow for differences in geometry like a keystone or an asymmetrical sample. If cable 1 has m by n grid points and cable 2 has o by p grid points the field distribution can be calculated by:

$$\boldsymbol{B}_{s,t} = \sum_{i=1}^{n}\sum_{j=1}^{m} \boldsymbol{B}(r_{i,j} - r_{s,t}) + \sum_{k=1}^{o}\sum_{l=1}^{p} \boldsymbol{B}(r_{k,l} - r_{s,t}) \quad \text{[T]}. \tag{E.2}$$

The naming convention of the indexes is explained in figure E.1. By making the current location dependent ($I_{i,j}$), more detailed geometries can be solved using this algorithm, without the need of very small grid size. The conductor fraction in the calculation cell is estimated and this value is multiplied with the current. This allows to calculate the self-field in conductors while taking the shape and size of the strands in the cable into account [102], see the bottom of figure

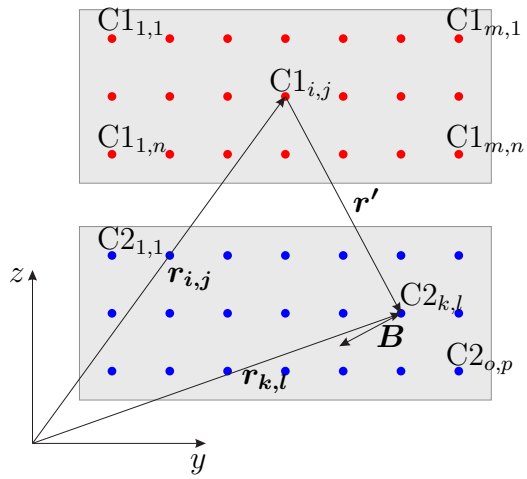

Figure E.1: Calculation of the magnetic field in point C2$_{k,l}$ resulting from the current in point C1$_{i,j}$.

E.2 for an example. To ensure that the total current is correct, the sum of the currents is normalized.

The self-field calculation is numerically relatively intensive. To increase the speed of the calculation, the self-field is calculated for a unit current (1 kA) and then scaled with the required current. For a different value for the current but the same geometry, no recalculation of equation E.2 is needed. The total field calculation is the vector addition of the applied magnetic field and the self-field.

To validate the model the calculated self-field of a rectangular cable is compared to that determined with the CERN in-house magnet design software package ROXIE [103]. The cable was calculated in ROXIE with its actual number of strands and several cases with a much larger number of virtual strands equidistantly spaced within the bounding box of the cable. This is analog to the grid used in the correction algorithm. In all cases there was no difference between the two models within four significant digits.

E.2 VAMAS Barrel

The virgin and extracted wires, for comparison to the cable results, are measured on a so-called VAMAS barrel, see figure 5.1. This is a barrel made from a resistive titanium alloy, with a groove machined in it to fixate the wire. Since the wire is wound on the barrel with relative loose winding and a low number of turns, a first order approximation of the peak field on the wire is:

$$B_p = B_{app} + \frac{\mu_0 I}{2\pi r_{fil}} = B_{app} + \frac{2I}{r_{fil}} 10^{-7} \quad [\mathrm{T}]. \tag{E.3}$$

Here B_p is the peak magnetic field in the filamentary zone of the wire, defined by the radius r_{fil}. B_{app} is the value of the applied magnetic field.

Because the wire is wound in a coil like structure on the barrel, the sample generates a small magnetic field in the center of the

barrel. This field is always directly opposed to the applied field, to ensure that the Lorentz forces push the wire against the barrel. This also gives rise to a small error in the effective B_{app} in equation E.3. If the value is calculated using FEM analysis [87], it is found that this correction is about -90 µT/A. This was calculated for the most outlying turn on the barrel, which is not where the voltage taps are located. Furthermore, the size of the wire changes the location of the current carrying elements and thus the resulting magnetic field.

The effective field of the wire samples is calculated in a similar fashion as the straight cables, even though the geometry is completely different. The barrel has a diameter of 32 mm with a 0.75 mm deep groove running from one connection terminal to the next in 9 turns around the barrel. This is approximated by 9 equidistant parallel current loops. A perfectly round current loop can be described by the following expression, taken from [104], chapter 20B:

$$B_x = B_0 \frac{1}{\pi\sqrt{Q}} \left[E(k) \frac{1-\alpha^2-\beta^2}{Q-4\alpha} + K(k) \right] \quad \text{[T]}, \qquad \text{(E.4)}$$

$$B_r = B_0 \frac{\gamma}{\pi\sqrt{Q}} \left[E(k) \frac{1+\alpha^2+\beta^2}{Q-4\alpha} - K(k) \right] \quad \text{[T]}, \qquad \text{(E.5)}$$

where,

$$B_0 = \frac{\mu_0 I}{2a} \qquad \text{[T]}, \qquad \text{(E.6)}$$

$$\alpha = \frac{r}{a}, \quad \beta = \frac{x}{a}, \quad \gamma = \frac{x}{r} \qquad \text{[−]}, \qquad \text{(E.7)}$$

$$Q = (1+\alpha)^2 + \beta^2 \text{ and } k = \sqrt{\frac{4\alpha}{Q}} \qquad \text{[−]}. \qquad \text{(E.8)}$$

Here the loop is assumed to lie in the yz-plane, with the center of the loop in the origin, the loop radius is a, r is the absolute distance from the x-axis and I is the current flowing through the loop. K and E are the elliptical integrals of the first and second kind respectively. They are solved numerically in MATLAB.

The algorithm for the calculation is similar to the cable case, the strand cross section is divided into an equidistant grid and the magnetic field from each point is calculated in all other points. However,

instead of equation E.1 equations E.4 and E.5 are used. Aside from the wire cross section of interest 8 other loops are added to simulate the entire barrel. These extra wires are simulated as single current loops without further subdivision into current carrying elements.

The result can be seen in figure E.3, here a typical example is taken with a wire carrying 1000 A in a 12 T background magnetic field. Inside the barrel the absolute value of the magnetic field is decreased due to the field generated by the sample on the barrel. The peak magnetic field is found on the edge of the filamentary zone facing away from the barrel.

E.3 U-shaped sample holder

The U-shaped sample holder used in the short sample cable tests has a more complex geometry which can not straightforwardly be solved numerically. A FEM model was used to quantify the self-field acting on the sample [105].

The model incorporated the entire Nb_3Sn part of the sample and the field generated by the magnet. Since the magnet used is a solenoid and the sample is quite large, the applied field is not assumed to be constant, but the approximate field generated by the magnet is taken into account. This model is also used to estimate the Lorentz forces acting on the sample.

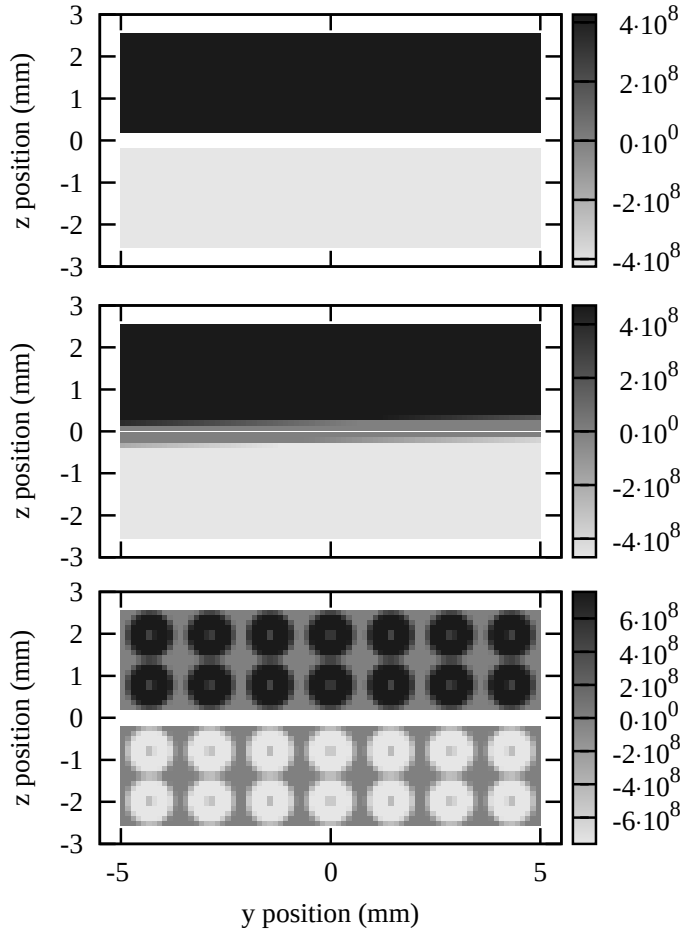

Figure E.2: Current density distribution used in various simulations. From top to bottom: rectangular conductor, keystoned conductor and a conductor with strands.

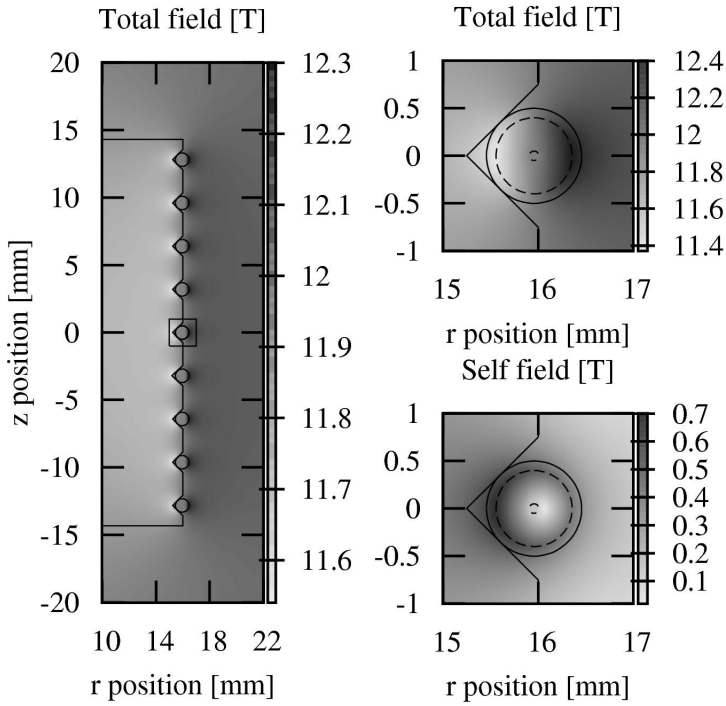

Figure E.3: Magnetic field distribution in tesla of a VAMAS barrel supporting a 1 mm diameter strand, carrying 1000 A in a background magnetic field of 12 T. The left graph shows the full barrel with 9 turns, the top right shows a zoom in at the center strand and the bottom right shows the same with only the self-field plotted.

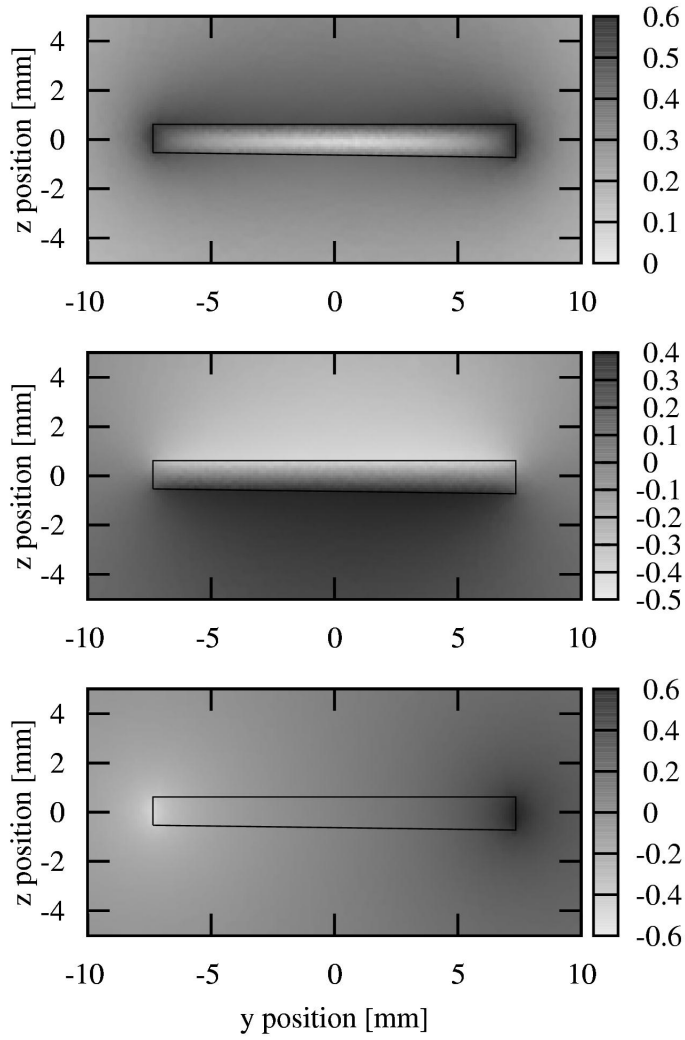

Figure E.4: Self-field of the U-shaped sample powered with 10 kA in tesla. From top to bottom: total field, horizontal component and vertical component. The cross section is taken in the center of the sample.

Appendix F

MQE maps

These are the MQE maps of the center heater and the thin edge heater of sample H. The results are very similar to the ones presented in figure 8.10. These figures cover a slightly smaller range in magnetic field due to the self-field effect. The results are placed here since they do not add much to the discussion in the results chapter, but two parameter thermal stability data sets are so rare that they are included here.

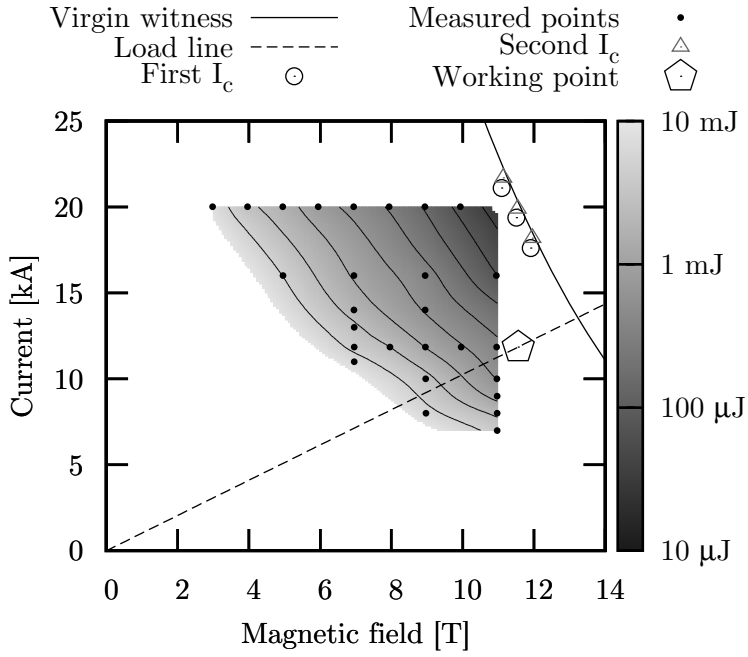

Figure F.1: Density plot of the MQE at the center heater as a function of the total magnetic field and test current. The data points are interpolated using a 2D spline algorithm to obtain a smooth surface. Contours with a factor 2 difference in energy between successive lines are added for clarity. The plot is superimposed on the $I_c(B)$ curve to give context.

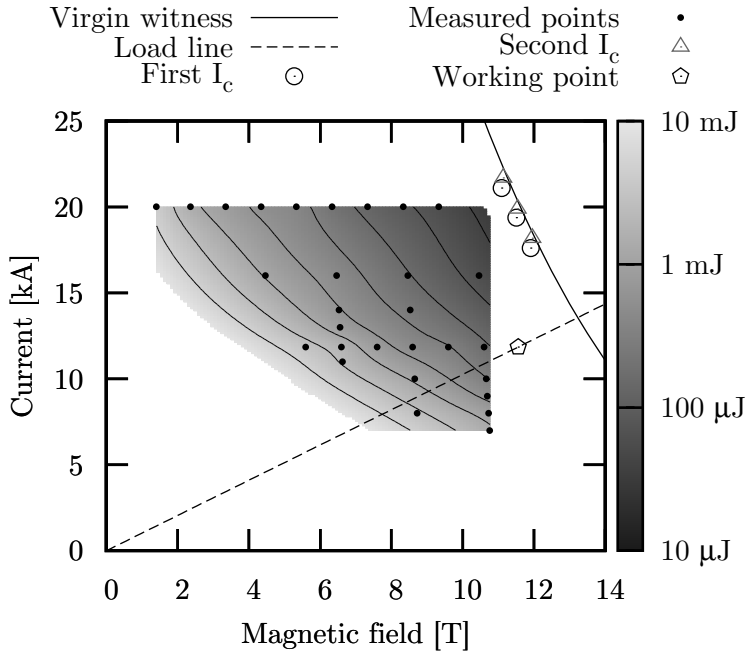

Figure F.2: Density plot of the MQE at the thin edge heater as a function of the total magnetic field and test current. The data points are interpolated using a 2D spline algorithm to obtain a smooth surface. Contours with a factor 2 difference in energy between successive lines are added for clarity. The plot is superimposed on the $I_c(B)$ curve to give context.

References

[1] H. Kamerlingh Onnes, Further experiments with liquid helium. c. on the change of electric resistance of pure metals at very low temperatures etc. iv. the resistance of pure mercury at helium temperatures, *KNAW, Proceedings*, vol. 13, pp. 1274–1276, 2 1911.

[2] J.K. Hulm and R.D. Blaugher, Superconducting solid solution alloys of the transition elements, *Physical Review*, vol. 123, no. 5, p. 1569, 1961.

[3] B.T. Matthias, T.H. Geballe, S. Geller, and E. Corenzwit, Superconductivity of Nb_3Sn, *Physical Review*, vol. 95, no. 6, p. 1435, 1954.

[4] J. Bardeen, L.N. Cooper, and J.R. Schrieffer, Theory of Superconductivity, *Physical Review*, vol. 108, no. 5, p. 1175, 1957.

[5] F.R. Fickett, Electric and magnetic properties of CuSn and CuNi alloys at 4 K, *Cryogenics*, vol. 22, no. 3, pp. 135–137, 1982.

[6] J.M. van Oort, Critical current degradation in Nb_3Sn superconductors in accelerator magnets, PhD thesis, University of Twente, Enschede, The Netherlands, 2000.

[7] S. Russenschuck, Design of Accelerator Magnets, in *CERN Accelerator School*, 2004.

[8] J.L. Caron, Artist impression of bending dipole coils in the LHC, CERN website, retrieved on 28-01-2013.

[9] M.N. Wilson, Superconducting magnets, 2nd ed. Oxford University Press, USA, 1987.

[10] M. Bruchon, G. De Rijk, M. Durante, *et al.*, EuCARD HFM dipole model design options, EuCARD-REP-2010-002, 2010.

[11] S. Russenschuck, Field Computation for Accelerator Magnets. Wiley-VCH, Berlin, Germany, 2010.

[12] P.A. Alekseev, A.I. Boev, V.E. Keilin, *et al.*, Experimental evidence of considerable stability increase in superconducting windings with extremely high specific heat substances, *Cryogenics*, vol. 44, no. 11, pp. 763–766, 2004.

[13] A. Puigsegur, F. Rondeaux, E. Prouzet, and K. Samoogabalan, Development of an Innovative Insulation for Nb_3Sn Wind and React Coils, *AIP Conference Proceedings*, vol. 711, no. 1, U. (Balu) Balachandran and M. Adams, Eds., pp. 266–272, 2004.

[14] D. Schoerling, Superconducting wiggler magnets for beamemittance damping rings, PhD thesis, Technische Universität Bergakademie Freiberg, 2012.

[15] E. Rochepault, W.M. de Rapper, P. Vedrine, F. Rondeaux, and F. Bouillault, First Performance Test of Ceramic-insulated Conductors, *IEEE Transactions on Applied Superconductivity*, vol. 22, no. 3, 2012.

[16] A.P. Verweij, Electrodynamics of Superconducting Cables in Accelerator Magnets, PhD thesis, University of Twente, Enschede, The Netherlands, 1995.

[17] R. Otmani, A. Devred, and P. Tixador, Interstrand and AC-loss Measurements on Rutherford-type Cables for Accelerator Magnet Applications, *Applied Superconductivity, IEEE Transactions on*, vol. 11, no. 1, pp. 2760–2763, 2001.

[18] E. Collings, M. Sumption, M. Susner, *et al.*, Control of Interstrand Contact Resistances of Nb_3Sn Rutherford Cables with Cores of Woven-Glass-Fiber Ribbons and Stainless-Steel Tapes, *Applied Superconductivity, IEEE Transactions on*, vol. PP, no. 99, p. 1, 2012.

[19] A. Devred, D.E. Baynham, L. Bottura, *et al.*, High field accelerator magnet R&D in Europe, *Applied Superconductivity, IEEE Transactions on*, vol. 14, no. 2, pp. 339–344, 2004.

[20] A. Devred, B. Baudouy, D.E. Baynham, *et al.*, Overview and status of the Next European Dipole Joint Research Activity, *Superconductor Science and Technology*, vol. 19, no. 3, S67, 2006.

[21] F. Regis, P. Manil, P. Fessia, M. Bajko, and G. De Rijk, Mechanical Design of the SMC (Short Model Coil) Dipole Magnet, *Applied Superconductivity, IEEE Transactions on*, vol. 20, no. 3, pp. 204–207, 2010.

[22] P. Manil, F. Regis, J. Rochford, *et al.*, Magnetic Design and Code Benchmarking of the SMC (Short Model Coil) Dipole Magnet, *Applied Superconductivity, IEEE Transactions on*, vol. 20, no. 3, pp. 184–187, 2010.

[23] M. Bajko, B. Bordini, S. Canfer, *et al.*, The Short Model Coil (SMC) dipole: an R&D program towards Nb_3Sn accelerator magnets, *Applied Superconductivity, IEEE Transactions on*, 2011.

[24] A.P. Verweij, J. Genest, A. Knezovic, *et al.*, 1.9 K test facility for the reception of the superconducting cables for the LHC, *Applied Superconductivity, IEEE Transactions on*, vol. 9, no. 2, pp. 153–156, 1999.

[25] G. De Rijk, A. Milanese, and E. Todesco, 11 Tesla Nb_3Sn dipoles for phase II collimation in the Large Hadron Collider, CERN, Tech. Rep. 19, 2010, sLHC Project Note.

[26] S.A. Gourlay, G. Ambrosio, N. Andreev, *et al.*, Magnet R&D for the US LHC Accelerator Research Program (LARP), *Applied Superconductivity, IEEE Transactions on*, vol. 16, no. 2, pp. 324–327, 2006.

[27] P. Ferracin, LARP Nb_3Sn Quadrupole Magnets for the LHC Luminosity Upgrade, in *AIP Conference Proceedings*, vol. 1218, 2010, pp. 1291–1300.

[28] L. Bottura, G. de Rijk, L. Rossi, and E. Todesco, Advanced Accelerator Magnets for Upgrading the LHC, *Applied Superconductivity, IEEE Transactions on*, 2012.

[29] S.L. Wipf, Magnetic Instabilities in Type-II Superconductors, *Phys. Rev.*, vol. 161, pp. 404–416, 2 1967.

[30] P.S. Swartz and C.P. Bean, A model for magnetic instabilities in hard superconductors: the adiabatic critical state, *Journal of Applied Physics*, vol. 39, no. 11, pp. 4991–4998, 1968.

[31] A.R. Kantrowitz and Z.J.J. Stekly, A new principle for the construction of stabilized superconducting coils, *Applied Physics Letters*, vol. 6, pp. 56–57, 3 1965.

[32] Z.J.J. Stekly and J.L. Zar, Stable superconducting coils, *IEEE Trans. Nucl. Sci*, vol. 12, no. 3, pp. 367–372, 1965.

[33] P.S. Swartz and C.P. Bean, A model for magnetic instabilities in hard superconductors: the adiabatic critical state, *Journal of Applied Physics*, vol. 39, no. 11, pp. 4991–4998, 1968.

[34] M.N. Wilson and Y. Iwasa, Stability of superconductors against localized disturbances of limited magnitude, *Cryogenics*, vol. 18, no. 1, pp. 17–25, 1978.

[35] B. Bordini, E. Barzi, S. Feher, L. Rossi, and A.V. Zlobin, Self-field effects in magneto-thermal instabilities for nb_3sn strands, *Applied Superconductivity, IEEE Transactions on*, vol. 18, no. 2, pp. 1309–1312, 2008.

[36] B. Bordini, Thermo-magnetic instabilities in Nb_3Sn superconducting accelerator magnets, PhD thesis, Fermi National Accelerator Laboratory, Batavia, IL, USA, 2006.

[37] B. Bernardo and L. Rossi, Self field instability in high-J_c Nb_3Sn strands with high copper residual resistivity ratio, *IEEE Trans. Appl. Supercond.*, vol. 19, no. CERN-AT-2008-045, pp. 2470–2476, 2009.

[38] E. Takala, The Laser Quenching Technique for Studying the Magneto-Thermal Instability in High Critical Current Density Superconducting Strands for Accelerator Magnets, PhD thesis, University of Turku, 2012.

[39] V.R. Chechetkin and A.S. Sigov, Stability of superconducting magnet systems subject to thermal disturbances, *Physics Reports*, vol. 176, pp. 1–81, 1-2 1989.

[40] M.N. Wilson and R. Wolf, Calculation of minimum quench energies in Rutherford cables, *Applied Superconductivity, IEEE Transactions on*, vol. 7, no. 2, pp. 950–953, 1997.

[41] A.P. Verweij, CUDI: A model for calculation of electrodynamic and thermal behaviour of superconducting Rutherford cables, *Cryogenics*, vol. 46, no. 7-8, pp. 619–626, 2006.

[42] D. Baynham, V. Edwards, and M. Wilson, Transient stability of high current density superconducting wires, *Magnetics, IEEE Transactions on*, vol. 17, no. 1, pp. 732–735, 1981.

[43] K. Seo, M. Morita, S. Nakamura, T. Yamada, and Y. Jizo, Minimum quench energy measurement for superconducting wires, *Magnetics, IEEE Transactions on*, vol. 32, no. 4, pp. 3089–3093, 1996.

[44] A.K. Gosh, W.B. Sampson, and M.N. Wilson, Minimum quench energies of Rutherford cables and single wires, *Applied Superconductivity, IEEE Transactions on*, vol. 7, no. 2, pp. 954–957, 1997.

[45] P. Bauer, J. Donnier, and L.R. Oberli, Tip heater for minimum quench energy measurements on superconducting strands, *Applied Superconductivity, IEEE Transactions on*, vol. 9, no. 2, pp. 1141–1144, 1999.

[46] G.P. Willering, A.P. Verweij, J. Kaugerts, and H.H.J. ten Kate, Stability of Nb-Ti Rutherford Cables Exhibiting Different Contact Resistances, *Applied Superconductivity, IEEE Transactions on*, vol. 18, no. 2, pp. 1263 –1266, 2008.

[47] G.P. Willering, A.P. Verweij, C. Scheuerlein, A. den Ouden, and H.H.J. ten Kate, Difference in Stability Between Edge and Center in a Rutherford Cable, *Applied Superconductivity, IEEE Transactions on*, vol. 18, no. 2, pp. 1253 –1256, 2008.

[48] P. Bauer, Stability of superconducting strands for accelerator magnets, PhD thesis, Vienna University of Technology, 1998.

[49] G.P. Willering, Stability of superconducting Rutherford cables for accelerator magnets, PhD thesis, University of Twente, Enschede, The Netherlands, 2009.

[50] E. Barzi, T. Wokas, and A.V. Zlobin, Sensitivity of Nb_3Sn Rutherford type cables to transverse pressure, *Applied Superconductivity, IEEE Transactions on*, vol. 15, no. 2, pp. 1541–1544, 2005.

[51] P. Bauer and D. Dietderich, Critical Current Measurements of Superconducting Cables at the NHMFL, Fermilab TD-99-039, Batavia, USA, Tech. Rep., 1999.

[52] H.H.J. ten Kate, H.W. Weijers, and J.M. van Oort, Critical current degradation in Nb_3Sn cables under transverse pressure, *Applied Superconductivity, IEEE Transactions on*, vol. 3, no. 1, pp. 1334–1337, 1993.

[53] S. Feher, G. Ambrosio, N. Andreev, *et al.*, Cable testing for Fermilab's high field magnets using small racetrack coils, *Applied Superconductivity, IEEE Transactions on*, vol. 15, no. 2, pp. 1550–1553, 2005.

[54] A.G. Prodell and A. Arn, A facility for evaluating superconductors above atmospheric pressure at 1.8 K, *Advances in Cryogenic Engineering*, vol. 43, pp. 443–450, 1998.

[55] G. Ambrosio, S. Bartlett, D. Dietderich, *et al.*, Design of a sample holder for Nb_3Sn cable test at FRESCA, FermiLab, TD note TD-04-022, 2004.

[56] G. Ambrosio, N. Andreev, S.E. Bartlett, *et al.*, Critical current and instability threshold measurement of Nb_3Sn cables for high field accelerator magnets, *Applied Superconductivity, IEEE Transactions on*, vol. 15, no. 2, pp. 1545 –1549, 2005.

[57] A.K. Ghosh, L.D. Cooley, and A.R. Moodenbaugh, Investigation of instability in high J_c Nb_3Sn strands, *Applied Superconductivity, IEEE Transactions on*, vol. 15, no. 2, pp. 3360–3363, 2005.

[58] G. Ambrosio, N. Andreev, E. Barzi, *et al.*, Measurement of Critical Current and Instability Threshold of Rutherford-Type Cables, *Applied Superconductivity, IEEE Transactions on*, vol. 16, no. 2, pp. 1160–1163, 2006.

[59] H. Ibach and H. Lüth, Solid-state physics: an introduction to principles of materials science, Second Edition. Springer Verlag, 1995.

[60] M.D. Sumption and E.W. Collings, Chromium diffusion into plated Nb_3Sn strands deduced from electrical resistivity measurement, *Applied Superconductivity, IEEE Transactions on*, vol. 5, no. 2, pp. 1925–1928, 1995.

[61] A.P. Verweij, CUDI: Users Manual, CERN.

[62] M. Gurvitch, A.K. Ghosh, H. Lutz, and M. Strongin, Low-temperature resistivity of ordered and disordered A15 compounds, *Physical Review B*, vol. 22, no. 1, p. 128, 1980.

[63] A. Godeke, Performance boundaries in Nb_3Sn superconductors, PhD thesis, University of Twente, Enschede, The Netherlands, 2005.

[64] L. Bottura and B. Bordini, $J_C(B, T, \epsilon)$ parameterization for the ITER Nb_3Sn production, *Applied Superconductivity, IEEE Transactions on*, vol. 19, no. 3, pp. 1521–1524, 2009.

[65] E.D. Marquardt, J.P. Le, and R. Radebaugh, Cryogenic Material Properties Database, *11th International Cryocooler Conference*, vol. 12, no. 6, pp. 1–7, 2000.

[66] G.D. Cody and R.W. Cohen, Thermal conductivity of Nb_3Sn, *Rev. Mod. Phys.*, vol. 36, pp. 121–123, 1 1964.

[67] N.J. Simon, E.S. Drexler, and R.P. Reed, Properties of copper and copper alloys at cryogenic temperatures, ser. NIST monograph, 117. Washington, D.C, USA, 1992.

[68] R.W. Arenz, C.F. Clark, and W.N. Lawless, Thermal conductivity and electrical resistivity of copper in intense magnetic fields at low temperatures, *Phys. Rev. B*, vol. 26, pp. 2727–2732, 6 1982.

[69] W. Goldacker, R. Ahrens, M. Nindel, B. Obst, and C. Meingast, HIP synthesized Nb_3Sn bulk materials with extraordinary homogeneity, *Applied Superconductivity, IEEE Transactions on*, vol. 3, no. 1, pp. 1322–1325, 1993.

[70] J.B. Clark, G.B. Hopple, and R.N. Wright, The effect of grain size on the high temperature plastic deformation of Nb_3Sn, *Metallurgical and Materials Transactions A*, vol. 14, no. 4, pp. 889–894, 1983.

[71] J.G. Hust, Thermal conductivity of glass fiber/epoxy composite support bands for cryogenic dewars. phase 2. NTIS, Springfield, VA(USA), Tech. Rep. NBSIR 84-3003, 1984.

[72] V. Guritanu, W. Goldacker, F. Bouquet, *et al.*, Specific heat of Nb_3Sn: the case for a second energy gap, *Physical Review B*, vol. 70, no. 18, p. 184 526, 2004.

[73] F. Bouquet, Y. Wang, P. Toulemonde, *et al.*, Using specific heat to scan gaps and anisotropy of MgB_2, *Physica C: Superconductivity*, vol. 408, pp. 60–62, 2004.

[74] N.W. Ashcroft and N.D. Mermin, Solid State Physics. San Diego: Thomson Learning, 1976.

[75] M. Karppinen, N. Andreev, G. Apollinari, *et al.*, Design of 11 T Twin-Aperture Nb_3Sn Dipole Demonstrator Magnet for LHC Upgrades, *Applied Superconductivity, IEEE Transactions on*, 2012.

[76] J.B.J. Fourier, Théorie analytique de la chaleur. Paris, France: Gauthier-Villars et fils, 1822.

[77] T.P. Orlando and K.A. Delin, Foundations of applied superconductivity. San Diego, USA: Addison-Wesley, 1991.

[78] E.B. Rosa, The self and mutual inductances of linear conductors, *Bulletin of the Bureau of Standards*, vol. 4, no. 2, pp. 301–344, 1908.

[79] L. Dresner, Stability of superconductors. New York: Plenum Press, 1995.

[80] O. Umezawa and K. Ishikawa, Electrical and thermal conductivities and magnetization of some austenitic steels, titanium and titanium alloys at cryogenic temperatures, *Cryogenics*, vol. 32, no. 10, pp. 873–880, 1992.

[81] A. Clark and J. Ekin, Defining critical current, *Magnetics, IEEE Transactions on*, vol. 13, no. 1, pp. 38 –40, 1977.

[82] M. Garber, A.K. Ghosh, and W.B. Sampson, The effect of self field on the critical current determination of multifilamentary superconductors, *Magnetics, IEEE Transactions on*, vol. 25, no. 2, pp. 1940–1944, 1989.

[83] J.F. Bussiere, D.O. Welch, and M. Suenaga, Young's Modulus of Polycrystalline Nb_3Sn between 4.2 and 300 K, *Journal of Applied Physics*, vol. 51, no. 2, pp. 1024–1030, 1980.

[84] G.P. Willering and A.P. Verweij, Modeling the heat flow from a graphite paste heater used for cable stability measurements, *CERN AT-MCS, internal note*, 2007.

[85] T.B. Massalski, J.L. Murray, L.H. Bennett, and H. Baker, Binary Alloy Phase Diagrams. ASM International, USA, 1991, vol. 2.

[86] A. den Ouden, T. Boutboul, D. Pedrini, *et al.*, Critical Current Measurements on Conductors for the NED Project, *Applied Superconductivity, IEEE Transactions on*, vol. 16, no. 2, pp. 1265–1268, 2006.

[87] B. Bordini, Self-Field Correction in Critical Current Measurements of Superconducting Wires Tested on ITER VAMAS Barrels, CERN, TE internal note 1105765, 2010.

[88] H.H.J. ten Kate, H. Weijers, S. Wessel, H. Boschman, and L.J.M. van de Klundert, The reduction of the critical current in Nb_3Sn cables under transverse forces, *Magnetics, IEEE Transactions on*, vol. 28, no. 1, pp. 715 –718, 1992.

[89] D. Richter, J.D. Adam, D. Leroy, and L.R. Oberli, Strand coating for the superconducting cables of the LHC main magnets, *Applied Superconductivity, IEEE Transactions on*, vol. 9, no. 2, pp. 735–741, 1999.

[90] D. Richter, J.D. Adam, J.-M. Depond, D. Leroy, and L.R. Oberli, DC measurement of electrical contacts between strands in superconducting cables for the LHC main magnets, *Applied Superconductivity, IEEE Transactions on*, vol. 7, no. 2, pp. 786–792, 1997.

[91] V.V. Kashikhin and A.V. Zlobin, Magnetic instabilities in Nb_3Sn strands and cables, *Applied Superconductivity, IEEE Transactions on*, vol. 15, no. 2, pp. 1621–1624, 2005.

[92] G. Ambrosio, N. Andreev, M. Anerella, *et al.*, Design of Nb_3Sn Coils for LARP Long Magnets, *Applied Superconductivity, IEEE Transactions on*, vol. 17, no. 2, pp. 1035–1038, 2007.

[93] E. Takala, B. Bordini, and L. Rossi, Perturbation Sensitivity of Magnetothermal Instability, *Applied Superconductivity, IEEE Transactions on*, vol. 22, no. 6, pp. 4 706 106–4 706 106, 2012.

[94] M.D. Sumption, M. Susner, E.W. Collings, *et al.*, Effect of Cable Edge Deformation on RRR and Magnetization of Strands Extracted From Nb_3Sn Rutherford-Type Cables, *Applied Superconductivity, IEEE Transactions on*, vol. 19, no. 3, pp. 2481–2485, 2009.

[95] W.M. De Rapper, B. Bordini, S. le Naour, L. Bottura, and H.H.J. ten Kate, Critical Current in high-J_c Nb_3Sn Rutherford Cables Affected Substantially by the Direction of the Applied Magnetic Field, *Applied Superconductivity, IEEE Transactions on*, vol. 22, no. 3, pp. 6 001 704–6 001 704, 2012.

[96] S.F. Cogan and R.M. Rose, Properties of CuSn bronze at 4.2 K, *Cryogenics*, vol. 20, no. 6, pp. 313–318, 1980.

[97] M.D. Sumption, V. Nazareth, E. Barzi, *et al.*, Measurements of RRR variation in strands extracted from nb_3sn -type rutherford cables, in *AIP Conference Proceedings*, vol. 986, 2008, pp. 277–284.

[98] M.D. Sumption, M. Susner, E.W. Collings, *et al.*, Effect of cable edge deformation on RRR and magnetization of strands extracted from nb_3sn rutherford-type cables, *Applied Superconductivity, IEEE Transactions on*, vol. 19, no. 3, pp. 2481–2485, 2009.

[99] R.V. Smith, Review of heat transfer to helium I, *Cryogenics*, vol. 9, no. 1, pp. 11–19, 1969.

[100] W.M. de Rapper, L.R. Oberli, B. Bordini, E. Takala, and H.H.J. ten Kate, Critical Current and Stability of High-J_c Nb_3Sn Rutherford Cables for Accelerator Magnets, *Applied Superconductivity, IEEE Transactions on*, 2011.

[101] J. Clerk Maxwell, On physical lines of force, *Philosophical Magazine*, vol. 21, p. 168, 1861.

[102] M. Greco, P. Fabbricatore, R. Musenich, C. Priano, and F. Kircher, Self-field effects on critical current measurements of large multi-strand conductors, *Applied Superconductivity, IEEE Transactions on*, vol. 13, no. 2, pp. 3374 –3377, 2003.

[103] S. Russenschuck, ROXIE - A Computer Code for the Integrated Design of Accelerator Magnets, in *Sixth European Particle Accelerator Conference*, Stockholm, Sweden, 1998, pp. 2017–2019.

[104] T.J. Dolan, Fusion research: Principles, experiments and technology. New York, USA: Pergamon Press, 1982.

[105] W. van de Camp, COMSOL Self-field results, Private communication, 2012.

Summary

Circular particle colliders, like the Large Hadron Collider (LHC), require particle bending magnets with a high magnetic field. In the LHC superconducting magnets are applied to achieve such magnetic fields. These magnets store large amounts of energy in their magnetic field, sufficient to severely damage the coil windings and even surrounding systems.

A relatively small perturbation of about 100 µJ in a single point can cause a transfer of a small section of a strand in the superconducting cable to the normal state. In such a normal zone severe joule heating takes place, while on the other hand the normal zone is cooled by its surroundings. If the heating exceeds the cooling the normal zone will expand, and vice versa it will collapse. Once there is an expanding normal zone in a superconducting cable, it will spread throughout the entire coil. This is referred to as the quenching of the superconducting state, or magnet quench. When this occurs the energy stored in the magnetic field needs to be discharged in a controlled way. The thermal stability of a superconductor defines the amount of thermal energy required for a point disturbance to initiate a quench.

The latest generation of high current density Nb_3Sn wires generally have a relatively low thermal stability, since the joule heating is larger due to the higher current density while the cooling is less due to lower volume ratios of stabilizing copper. It is estimated that under the most severe operating conditions a normal zone of two millimeter is sufficient to trigger a quench leading to down time of the entire

collider. Several models exist to predict the thermal stability, but there are no empirical data available on Rutherford cables featuring high current density Nb_3Sn conductors to validate them. The aim of this work is to measure the thermal stability of Nb_3Sn Rutherford cables directly.

To this end a new sample holder for an existing test station is developed, to test Nb_3Sn cables at varying transport current in various applied magnetic fields and temperatures. This enables the exploration of cable properties under conditions normally only encountered in the center of a superconducting coil.

With the aid of point heaters, the thermal stability is probed at various positions on the cable surface under various operating conditions. It is shown that regardless of the high current density and poor cooling, theses cables can recover from a quenched strand by current redistribution when the test conditions are far from the cable limitations. This transition point, where the cable can recover from a single normal strand, is determined for test current and applied magnetic field as close as possible to the typical operational conditions of a magnet coil within the experimental window. For an applied magnetic field of 9 tesla it is found that for a reduced current (I/I_c) less than 0.4 the cable can recover from a quenched strand and the cable behavior benefits from collective strands stability. For a cable carrying the critical current at a magnetic field of 12 tesla, this transition occurs at a reduced magnetic field (B/B_{c2}) of roughly 0.4.

In the center part of a Rutherford cable the thermal stability is significantly better than at the cable edges. This is due to a reduced RRR and degraded critical current at the thick and thin edges of the cable. The thermal stability decreases when Nb_3Sn is operated at a lower temperature, i.e. 1.9 K. This is to be expected when considering the reduced material properties at this temperature.

Two numerical models and one analytical model are compared to the empirical observations. It is found that none of the models predicts all features of the thermal stability curves with high accu-

racy. There are several possible reasons for this. Some parameters, like the inter-strand interactions, are only known as a global average, while local variations or systematic distributions over the cable can have a significant impact on the thermal stability. Secondly, the high current densities and poor cooling result in extremely short normal zones from which the cable can recover to the superconducting state. The numerical models evaluated here approximate the strands in the cable as line elements. When the minimum propagation zone is 2 millimeter and the strand diameter is 1.25 millimeter, the spacial resolution of the numerical model needs to be less than the strand diameter to converge on a solution. Typically the strand gets perturbed by external heat sources. For such small heat pulses there will be thermal gradients over the width of the strand with the same order of magnitude as the thermal gradients along the strand. Therefore a full 3D model of a strand cross section is required to correctly simulate point like thermal stability problems close to the critical surface of the superconductor.

Samenvatting (Summary in dutch)

In cirkelvormige deeltjesversnellers, zoals de "Large Hadron Collider" (LHC), zijn magneten nodig met een zo hoog mogelijk magneetveld om geladen deeltjes met een zo hoog mogelijke energie af te buigen en op een cirkelbaan te houden. In de LHC worden supergeleidende magneten gebruikt om zulke magneetvelden op te wekken. Deze magneten slaan een dusdanig grote hoeveelheid energie in het magneetveld op tijdens nominaal bedrijf, dat wanneer deze ongecontroleerd vrijkomt de spoelwindingen en zelfs omliggende componenten beschadigd kunnen raken.

Een relatief kleine puntverstoring van ongeveer 100 µJ kan een supergeleider in een onomkeerbare overgang naar de normale toestand brengen. In zo'n normale zone ontstaat door de hoge stroomdichtheid sterke interne warmte ontwikkeling. De normale zone wordt tegelijkertijd gekoeld door de nog koude omgeving. Als de warmteontwikkeling groter is dan de koeling zal de normale zone groeien, en omgekeerd zal de normale zone krimpen en verdwijnen. Als de normale zone zonder externe warmtebron expandeert, zal deze doorgroeien totdat de gehele geleider normaal is. Dit wordt een "quench" genoemd. Als dit in een magneet gebeurt moet de energie die in het magneetveld is opgeslagen gecontroleerd worden afgevoerd. De thermische stabiliteit van een supergeleider is een maat voor de hoeveelheid energie die nodig is om een quench te bewerkstelligen.

De laatste generatie Nb_3Sn geleiders hebben een relatief lage ther-

mische stabiliteit, omdat de interne warmteontwikkeling door de hoge stroomdichtheid enorm is, terwijl er tegelijkertijd weinig koeling is door de relatief kleine hoeveelheid stabiliserend koper. Een simpele afschatting laat zien dat onder piekbelasting een normale zone van slechts 2 millimeter lengte in een draad in een kabel al genoeg is om een quench te starten. Er bestaan diverse modellen die de thermische stabiliteit van supergeleiders voorspellen, maar er zijn nog geen empirische resultaten beschikbaar van Rutherford kabels met hoge stroomdichtheid om deze modellen te valideren. Het hoofddoel van dit werk is het direct meten van de thermische stabiliteit van dit soort kabels.

Hiervoor is een nieuwe houder voor kabel tests ontwikkeld voor een bestaande testopstelling, om Nb_3Sn Rutherford kabels bij variërende teststromen, magneetvelden en temperaturen te testen. Dit maakt het mogelijk kabeleigenschappen te meten onder condities die normaal in het midden van een magneet voorkomen.

Met behulp van puntvormige verwarmingselementen kan de thermische stabiliteit op verschillende plekken aan de buitenzijde van de kabel bepaald worden. Hieruit blijkt dat ondanks de hoge stroomdichtheid en slechte koeling, de geteste kabels in staat zijn te herstellen naar de supergeleidende toestand als een draad in de kabel volledig normaal geworden is, zolang er genoeg marge is tot het maximale stroom dragende vermogen van de kabel. De overgang waar de kabel van een enkele normale draad kan herstellen is bepaald voor testcondities die zo dicht mogelijk bij de condities in een typische Nb_3Sn magneet liggen, als door de experimentele limitaties is toegestaan. In een aangelegd magneetveld van 9 tesla wordt deze overgang gevonden bij een gereduceerde stroom (I/I_c) van minder dan 0.4. In een kabel die zijn kritieke stroom bij 12 tesla draagt vindt de overgang plaats bij een gereduceerd magneetveld (B/B_{c2}) van ongeveer 0.4.

In het centrale deel op de brede kant van een Rutherford kabel is de thermische stabiliteit doorgaans significant beter dan aan de randen van de kabel op de dunne kanten. Dit komt omdat de draadstukken in dunne en dikke zijkanten van de kabel een lagere RRR

waarde en kritieke stroom hebben. De thermische stabiliteit wordt significant minder wanneer een Nb_3Sn kabel bij lagere temperatuur, bijvoorbeeld 1.9 K bedreven wordt. Dit is voorspelbaar op basis van de materiaal eigenschappen bij deze temperatuur.

Twee numerieke modellen en een analytisch model zijn met de nieuw verkregen empirische resultaten vergeleken. De voorspelde kwantitatieve waardes uit de modellen komen slechts matig overeen met de gevonden data, hoewel kwalitatief het gedrag goed voorspeld wordt door één van de modellen. Hiervoor zijn enkele argumenten aan te voeren. Sommige parameters, zoals de interacties tussen de draden in de kabel, zijn alleen bekend als een gemiddelde waarde, terwijl kleine variaties en mogelijke verdelingen een aanzienlijke invloed hebben op de thermische stabiliteit. Verder zorgen de hoge stroomdichtheden voor extreem kleine toelaatbare normale zones in de draden. In de modellen die hier gebruikt zijn, zijn de draden in de kabel als ééndimensionale elementen gesimuleerd. Als de maximaal toelaatbare grootte van een normale zone 2 millimeter is, terwijl de draad diameter 1.25 millimeter is, moet de ruimtelijke resolutie van het model minder dan de draad diameter zijn om te convergeren. De verstoringen die hier bekeken worden komen van buiten af de draad in. Dit betekent dat de thermische gradiënt over de draad doorsnede vergelijkbaar is met de thermische gradiënt over de lengte van de draad. Daarom is in deze situatie een model nodig die de driedimensionale structuur van de draad meeneemt in de simulaties van de thermische stabiliteit, vooral dicht bij het kritieke oppervlak van de supergeleider.

Acknowledgments

A Ph.D. dissertation is a work that only bears the name of a single author, but has more contributors than a typical scientific paper (at least in the field of applied superconductivity). Here I would like to give credit to those who have contributed with technical, scientific or moral support.

First of all I would like to thank my advisor, Herman ten Kate, for giving me the opportunity to have this experience. The Ph.D. and the time abroad has proven to be very valuable to me and has taught me a great many things. I would also like to acknowledge his hard work in making this thesis more readable and motivating me in the end.

My co-advisor Marc Dhallé who was a great mentor and put in a lot of effort, even though he was only involved in the end. I will remember our lunch discussions which taught me more about the world in general than superconductors.

When I arrived at CERN, I was brought up to speed by Thierry Boutboul, who showed me the practical side of Nb_3Sn research. I partly owe my assignment to Luc-René Oberli, who helped setting up the Nb_3Sn cabling program at CERN which provided a large part of the samples for this work.

I would like to thank Luca Bottura, who still managed to make time in his busy schedule to support me when I needed advice. Many thanks to Bernardo Bordini, who was my day-to-day supervisor and was always there to listen to me when I came rambling into his office with fresh results or ideas. He also taught me not to grill salami.

The last part of my time at CERN I was supervised by Amalia Ballarino, who helped me getting the test time required for my final experiments.

Arjan Verweij helped me by making all the requested changes in the CUDI simulation code. Furthermore, I would like to thank him for the insightful discussions on thermal stability in superconductors and the modeling thereof.

The technical staff is of course of vital importance for an experimental work like this, and I would like to thank Angelo Bonasia, Pierre Jacquot, Oleg Kalouguine and Sander Wessel for making things work. A special mention for Laura Stewart for keeping the cryogenics in building 163 in working order.

Two people who helped providing me with additional sample material are Georgio Ambrosio from Fermilab and Dan Dietrich from LBNL. Many thanks for giving this work a more diverse set of samples.

My room mate at CERN, Eelis Takala, who was always available for long discussions on the fickle nature of Nb_3Sn in the day and available for BBQ and a beer in the evening. I always enjoyed the coffee breaks with Gerard Willering and Erwin Bielert, which helped me practice my dutch during my period at CERN.

I would also like to mention Andries den Ouden, who helped me setting up the first iteration of the sample preparation system. Even though he moved on to another institute, he was kind enough to bring me in contact with Dan Dietrich.

Finally I would like to thank my wife for joining the adventure at the start of my Ph.D. and my family for the time at the end of my Ph.D. when I was not as available as I would have liked to be.